

Universität
Rostock



Traditio et Innovatio



Structure-Reactivity Relationships in CeO₂-Supported Cu Catalysts: Influence of Formation, Structure and Stability of Active Sites on Catalytic Performance in Preferential CO Oxidation (PROX)

Dissertation

zur Erlangung des akademischen Grades

doctor rerum naturalium (Dr. rer. nat.)

der Mathematisch Naturwissenschaftlichen Fakultät

der Universität Rostock

angefertigt am Leibniz-Institut für Katalyse e.V.

an der Universität Rostock

vorgelegt von

Hayder Jawad Abed

geboren am 19.08.1990 in Al-Najaf

aus Iraq

Rostock, 10.08.2023

Jahr der Einreichung: 2023

Jahr der Verteidigung: 2023

Gutachter:

Prof. Dr. Angelika Brückner

Leibniz-Institut für Katalyse e.V. an der Universität Rostock

Prof. Dr. Ralf Ludwig

Institut für Chemie an der Universität Rostock

Erklärung

Hiermit erkläre ich, die vorliegende Arbeit selbstständig verfasst und keine anderen als die angegebenen Quellen und Hilfsmittel benutzt zu haben.

Rostock, 10.08.2023

Hayder Jawad Abed

Acknowledgment

First and foremost, I am thankful to Almighty Allah for giving me the strength, knowledge, ability, and opportunity to undertake my doctoral research and complete it satisfactorily.

I would like to express my sincere appreciation and thanks to my scientific supervisor Prof. Dr. Angelika Brückner for giving me the opportunity as a PhD student in her group and especially for the tremendous support and encouragement during my research. I am very grateful to her for invaluable guidance, continuous teaching, affection, and all her contribution of time and ideas, which helped me to learn a lot and strongly motivated me through the rough road to finish my thesis on time.

I would like to acknowledge Dr. Jabor Rabeah for helpful guidance, the experience shared and discussions during my research.

At the same time, I also want to thank Thanh Huyen Vuong for her support, EPR measurements, great contribution, and feedback on the publications. Further thank goes to Stephan Bartling for the NAP-XPS measurements. Special thanks go to Dr. Sebastian Wohlrab, Dr. Ali Mohamed AbdelMaged, and Dr.-Ing. Udo Armbruster for the good collaboration in this research.

I gratefully acknowledge Mr. Reinhard Eckelt for useful technical support, help with solving lab problems specially with catalytic experimental set up, as well as BET measurements. Additionally, I would like to send appreciations to Dr. Hanan Atia for H₂-TPR measurements, Dr. Nils Rockstroh for STEM measurements, Mrs. Anja Simmula for the ICP-OCS measurements, and last but not least all other members of analytic group for their direct or indirect help.

I also thank Reni Grauke for all her help during my initial PhD time, and most importantly for finding the solution to enrolled me as a Ph.D. student at Rostock university, I want to greatly thank Dr. Abdallah Ibrahim Mohammed Rabee Ahmed for all help during last EPR measurements for my last batch samples and learning how to use EPR device in perfect way, becoming one of my close friends. A special thank goes to my office-mates Phong Dam, Dr. Elizaveta Fedorova, and Dr. Jana Weiß who have been very supportive in every way. Moreover, I want to thank all other groupmates including Simon Haida, Mamdouh Alafandi, Mirjam Schröder, Quang Dinh Ta, Jawaher Mosrati and Sebastian Cisneros for the supportive atmosphere, enjoyable time, kindness, and great parties at LIKAT. Further tributes go to all other members of the workshop, administration and purchasing department of LIKAT for all assistances and the congenial work atmosphere.

Finally, I would like to express my deepest appreciation to my family and my beloved wife Amani Abed for all their love, patience, encouragement, and unconditional support throughout my life including the years of PhD studying.

Zusammenfassung

Die präferentielle Oxidation (PROX) von CO ist eine wirksame und praktische Strategie zur Reduzierung von CO-Spurenmengen auf ein sehr niedriges Niveau (< 5 ppm) aus dem als Brennstoff für Protonenaustauschmembran-Brennstoffzellen verwendeten H_2 -reichen Gasstrom.

Cu-Katalysatoren haben sich aufgrund ihrer hohen Aktivität, Selektivität und Stabilität als kostengünstige Alternative zu den teuren Katalysatoren auf Edelmetallbasis erwiesen. Bei den meisten früheren Untersuchungen wurde jedoch eine höhere Cu-Beladung verwendet, in der Regel mehr als 5 wt%, so dass keine zuverlässigen Rückschlüsse auf die Art der aktiven Zentren (Cu-Einzelzentren, Dimere, Cluster und/oder Nanopartikel) möglich sind. Einatomige Katalysatoren (englisch: single site catalysts, SACs) mit isolierten Metallzentren gewinnen aufgrund ihrer maximalen Metallausnutzung und einzigartigen Strukturen große Aufmerksamkeit in der Forschung. In den letzten zehn Jahren wurden viele Anstrengungen unternommen, um hocheffiziente und kostengünstige SACs für die CO-Oxidation zu entwickeln. SACs haben nicht nur ihr hohes Potenzial zur Verbesserung der katalytischen Aktivität gezeigt, sondern auch einen detaillierten Einblick in den Mechanismus der Reaktion und den Ursprung der aktiven Zentren ermöglicht.

Inspiziert von diesen motivierenden Erkenntnissen besteht das Hauptziel dieser Doktorarbeit in der Entwicklung hochaktiver und stabiler Cu-Trägerkatalysatoren und dem Nachweis, dass einzelne Cu-Atome (SAC) auf der Oberfläche von reduzierbarem Ceroxid aktive Zentren für die PROX-Reaktion ist. Ein weiteres Ziel ist es, den Mechanismus der Reaktion zu klären.

Unsere Strategie zur Erreichung dieser Ziele bestand zunächst in der Herstellung, Charakterisierung und Erprobung hochaktiver geträgerter einatomiger Cu-Katalysatoren (SACs) für die PROX-Reaktion im Temperaturbereich von 50 bis 150 °C. Darüber hinaus wurden verschiedene operando- und in situ-spektroskopische Techniken wie EPR, DRIFT und NAP-XPS in Kombination mit grundlegenden Charakterisierungen angewandt, um die aktiven Zentren zu identifizieren und eine zuverlässige Struktur-Reaktivitäts-Beziehung abzuleiten.

Daher wurde im ersten Abschnitt (3.1) ein heterogener Katalysator mit sehr geringer Cu-Beladung (0,05 wt%) und einem CeO_2 - TiO_2 -Träger mit hoher Aktivität und Selektivität für die CO-Oxidation im Temperaturbereich von 60-100 °C getestet. Der katalytische Stabilitätstest ergab, dass der Katalysator während der 17-stündigen CO-PROX-Oxidation bei 120 °C in einem H_2 -reichen Strom (80%) keine Deaktivierung zeigte. Die ex-situ- und operando-spektroskopischen Ergebnisse deuten darauf hin, dass die Wechselwirkung von isolierten Cu-Zentren mit CeO_2 zur Bildung einer hoch redoxaktiven Cu^{2+} -O- Ce^{4+} -Einheit führt, die leicht CO durch Gittersauerstoff oxidieren und Cu^+ -□- Ce^{3+} bilden kann. Wir fanden heraus, dass Cu^+ -□- Ce^{3+} -Anteile die Fähigkeit haben, molekularen O_2 effektiv zu aktivieren und

Superoxid-Spezies zu bilden, die mit CO reagieren können, um CO₂ zu bilden und die Sauerstofflücken aufzufüllen und die Cu²⁺-O-Ce⁴⁺- Anteile für einen weiteren katalytischen Zyklus zu regenerieren.

Der zweite Abschnitt (3.2) konzentriert sich auf Cu-Katalysatoren mit handelsüblichem CeO₂ ohne Verwendung von TiO₂. Für deren Herstellung wurde eine einfache Präparationsmethode (Kugelmahlen) verwendet. Der Grund dafür ist die Vermeidung der hohen Kosten, der Komplexität, des Zeitaufwands und der chemischen Toxizität, die bei der Herstellung des Cu-Katalysators in Abschnitt (3.1) auftreten könnten. Ein weiterer Grund ist die Untersuchung des Einflusses der Cu Agglomeration auf die katalytische Aktivität und Selektivität von Cu/CeO₂ Katalysatoren unter PROX-Reaktionsbedingungen. Daher wurden drei Cu/CeO₂ Katalysatoren mit unterschiedlichen Cu Gehalten (0.25, 0.5 und 1 wt%) nach dieser einfachen Methode hergestellt. Eine Verringerung des Cu Gehalts von 1 auf 0.25 wt% führte zu einem signifikanten Anstieg der Cu-massennormierten CO-Oxidationsrate von 103 auf 303 μmol.g_{Cu}⁻¹.S⁻¹ bei 90 °C, was auf die Bildung von mehr einzelnen Cu-Zentren auf der Oberfläche von CeO₂ zurückzuführen ist. Darüber hinaus wiesen alle Cu-Katalysatoren eine hohe katalytische Stabilität und eine 100%ige CO₂-Selektivität während der Betriebszeit von mehr als 75 Stunden bei 90 °C auf. Hervorragende Aktivität und 100% Selektivität wurden mit dem Cu_{0.25}CeO₂-Katalysator erreicht, der eine fünfmal höhere CO-Oxidationsrate als in der Literatur berichtet aufwies.

Der dritte Abschnitt (3.3) befasst sich mit der Untersuchung der Auswirkungen der Sauerstofflücken, der Sauerstoffmobilität und der Redoxeigenschaften verschiedener handelsüblicher CeO₂-Träger mit unterschiedlichen Kristallitgrößen (3 und 25 nm) auf die katalytische Leistung. Die Studie zeigte, dass die Art des Trägers eine sehr wichtige Rolle spielt. Der Cu_{0.25}CeO₂-25nm-Katalysator zeigte eine höhere Aktivität als der Cu_{0.25}CeO₂-3nm-Katalysator. Die hohe Aktivität dieses Katalysators ist auf das ausgezeichnete Redoxverhalten (wie durch EPR nachgewiesen) und die große Oberfläche zurückzuführen. Die Ergebnisse der H₂-TPR des Cu_{0.25}CeO₂-25nm-Katalysators lassen darauf schließen, dass die Reduzierbarkeit viel einfacher ist als bei Cu_{0.25}CeO₂-3nm, was wiederum mit der hohen Aktivität dieses Katalysators zusammenhängt.

Abstract

The preferential oxidation (PROX) of CO is an effective and practical strategy to reduce trace amounts of CO to a very low level (< 5 ppm) from the H₂-rich stream used as fuel for proton exchange membrane fuel cells.

Cu catalysts have been proven to be cheap alternatives to the costly noble metal-based catalysts due to their high activity, selectivity, and stability. However, most of the previous investigations used a higher Cu loading, normally more than 5 wt% preventing any reliable conclusions about the nature of the active sites (Cu single sites, dimmers, clusters and/or nanoparticles).

Single-atom catalysts (SACs) with isolated metal sites are gaining great research attention owing to their maximized metal utilization rates and unique structures. During the last decade, many efforts have been made to design highly efficient and cost-effective SACs with CO oxidation. SACs have not only shown their high potential for improving catalytic activity but also provided an ideal insight for understanding the mechanism of the reaction and the origin of the active sites.

Inspired by these motivating findings, the major aim of my Ph.D. work is to develop highly active and stable supported Cu catalysts and to demonstrate that Cu single-atom catalyst (SAC) supported on the surface of highly reducible cerium oxide is the active site for PROX reaction. A further goal is to elucidate the mechanism of the reaction.

Our strategy to achieve these goals was firstly to prepare, characterize, and test highly active supported single-atom Cu catalysts (SACs) for PROX reaction in the temperature range of 50 to 150 °C. Furthermore, various operando and in situ spectroscopic techniques such as EPR, DRIFT, and NAP-XPS combined with basic characterizations have been applied to identify the active sites and derive reliable structure-reactivity relationships.

Therefore, in the first section (3.1), heterogeneous single-atom catalysts (SACs) based on a tiny Cu loading (0.05 wt%) supported on CeO₂-TiO₂ has shown high activity and selectivity for CO oxidation in the range of temperature 60-100 °C. The catalytic stability test revealed that the catalyst showed no deactivation during 17 h time on stream during CO-PROX at 120 °C under an H₂-rich stream (80 Vol%). The ex-situ and operando spectroscopic results indicate that the interaction of isolated single-atom Cu sites with CeO₂ results in the formation of a highly redox-active Cu²⁺-O-Ce⁴⁺ moieties that can easily oxidize CO by lattice oxygen and forming Cu⁺-□-Ce³⁺. We found that Cu⁺-□-Ce³⁺ moieties have the ability to effectively activate molecular O₂ and form superoxide species that can react with CO to form CO₂ and refill the oxygen vacancies and regenerate the Cu²⁺-O-Ce⁴⁺ moieties for another catalytic cycle. The second section (3.2) focuses on: (i) increasing the atomic efficiency of Cu-based catalysts by supporting Cu single-atom sites on highly reducible and commercial CeO₂ without using TiO₂.

(ii) Simple preparation method (ball-milling) was used to prepare single-atom (SACs) catalysts. The reason for this is to avoid the high cost, complexity, consuming time, and chemical toxicity that might occur during the preparation of the Cu catalyst in section (3.1). A further reason is studying the state of Cu agglomeration effect on the catalytic activity and selectivity over Cu/CeO₂ catalysts under PROX reaction conditions. Therefore, three Cu/CeO₂ catalysts were prepared by this simple method with different Cu loadings (0.25, 0.5, and 1 wt%). Decreasing Cu contents from 1 to 0.25 wt% resulted in a significant increase in the Cu mass-normalized CO oxidation rate from 103 to 303 μmol.g_{Cu}⁻¹.S⁻¹ at 90 °C. This is attributed to the formation of more single Cu ions on the surface of CeO₂. Superior activity and 100% selectivity were achieved with Cu_{0.25}CeO₂ catalyst that showed a 5 times higher CO oxidation rate than reported. Moreover, all Cu catalysts exhibited high catalytic stability and 100% CO₂-selectivity during the time on stream for more than 75 hours at 90 °C.

The third section focuses (3.3) on: studying the effect of the oxygen vacancy, oxygen mobility, and redox properties of different commercially available CeO₂ supports having different crystallite sizes (3 and 25 nm) on the catalytic performance. The study showed that the nature of the support plays a very important role. The Cu_{0.25}CeO₂-25nm catalyst showed higher activity than the Cu_{0.25}CeO₂-3nm catalyst. The high activity obtained by this catalyst is attributed to the excellent redox behaviour (as evidenced by EPR) and high surface area. The results of H₂-TPR of Cu_{0.25}CeO₂-25nm catalyst inferred that the reducibility is much easier than Cu_{0.25}CeO₂-3nm and this further factor correlated to high activity of this catalyst.

Contents

Acknowledgment.....	iv
Zusammenfassung.....	v
Abstract.....	vii
List of abbreviations.....	xi
1 Introduction.....	1
1.1 Motivation.....	1
1.2 Fuel cells and fuel processor.....	2
1.3 Hydrogen purification methods.....	3
1.4 Preferential Oxidation of CO (CO-PROX).....	4
1.5 Catalytic systems for the CO-PROX reaction: state of the art.....	4
1.6 CuO/CeO ₂ catalysts: state of the art.....	5
1.7 Objective.....	9
2 Experimental section.....	11
2.1 Catalyst preparation.....	11
2.1.1 Sol-gel method.....	11
2.1.2 Ball-milling method.....	11
2.2 PROX activity test.....	12
2.3 Catalyst characterization techniques.....	13
2.3.1 Inductively coupled plasma optical emission spectrometry (ICP-OES).....	13
2.3.2 X-ray diffraction (XRD).....	14
2.3.3 Low-temperature N ₂ adsorption.....	15
2.3.4 Scanning transmission electron microscopy (STEM).....	17
2.3.5 Temperature programmed reduction by H ₂ (H ₂ -TPR).....	18
2.3.6 Laser Raman spectroscopy (Raman).....	19
2.3.7 Operando Diffuse Reflectance Infrared Fourier Transform Spectroscopy (DRIFTS)....	20
2.3.8 Electron paramagnetic resonance (EPR).....	23
2.3.9 Near ambient pressure X-ray photoelectron spectroscopy (NAP-XPS).....	26

3	Results and discussions.....	29
3.1	Developing of $\text{Cu}_x\text{CeTiO}_2$ ($x = 0.05$ wt%) catalyst for CO PROX reaction	29
3.1.1	Catalytic performance of $\text{Cu}_{0.05}\text{CeTiO}_2$	29
3.1.2	Catalyst characterization.....	30
3.1.3	Operando NAP-XPS investigation.	34
3.1.4	Ex Situ and Operando EPR studies.....	35
3.1.5	Operando DRIFT investigation.....	37
3.1.6	Conclusions.....	38
3.2	Effect of preparation method and Cu loadings on the PROX catalytic activity of Cu_xCeO_2 ($x = 0.25, 0.5$ and 1 wt%) catalysts	40
3.2.1	Catalytic performance of Cu_x ($x = 0.25, 0.5$ and 1 wt%) CeO_2 catalysts.....	40
3.2.2	Catalyst characterization.....	42
3.2.3	Hydrogen temperature-programmed reduction (H_2 -TPR).....	45
3.2.4	Operando DRIFT	47
3.2.5	Ex Situ and Operando EPR Studies	50
3.2.6	Operando NAP-XPS	53
3.2.7	PROX Reaction mechanism over the CuCeO_2 catalyst.....	55
3.2.8	Conclusions.....	57
3.3	The impact of the support on the PROX activity of $\text{Cu}_{0.25}\text{CeO}_2$ -3nm and $\text{Cu}_{0.25}\text{CeO}_2$ -25nm catalysts.....	58
3.3.1	Catalytic performance of $\text{Cu}_{0.25}\text{CeO}_2$ -3nm and $\text{Cu}_{0.25}\text{CeO}_2$ -25nm catalysts.....	58
3.3.2	In situ DRIFTS investigations	62
3.3.3	Ex Situ and in situ EPR studies.....	64
3.3.4	Ex Situ XPS investigations	65
3.3.5	Conclusions.....	67
4	General conclusions and Future works	68
5	References.....	71
6	Appendix.....	75

List of abbreviations

PEMFC	proton exchange membrane fuel cell
PROX	preferential oxidation of a carbon monoxide
WGSR	water gas shift reaction
Cu-SACs	Cu single-atom catalysts
MOF	Metal-organic framework
a.u.	Arbitrary units
DRIFTS	Diffuse reflectance infrared Fourier transform spectroscopy
EPR	Electron paramagnetic resonance
GC	Gas chromatography
GHSV	Gas hourly space velocity
hfs	Hyperfine structure
ICP-OES	Inductively coupled plasma optical emission spectrometry
H ₂ -TPR	Hydrogen temperature-programmed reduction
Wt%	Weight percentage
Vol.%	Volume percentage
XRD	X-ray diffraction
STEM	Scanning transmission electron microscopy
NAP-XPS	Near ambient pressure X-ray photoelectron spectroscopy
OSC	Oxygen storage capacity
TCD	Thermal conductivity detector
HAADF-STEM	high-angle annular dark-field scanning transmission electron microscopy
EEL	electron energy loss spectrometer
EDX	energy-dispersive X-ray
25 nm	Crystallite size of the support per nanometer
3 nm	Crystallite size of the support per nano meter
NPs	nanoparticles

1 Introduction

1.1 Motivation

Over the past centuries, using of carbon-rich fossil fuels has allowed an unprecedented era of prosperity and development for human development. After the industrial revolution, the amount of CO₂ in the atmosphere has consequently increased from ~280 ppm to ~390 ppm in 2010, which is further expected to be ~570 ppm by the end of the century.¹ It can be claimed that the increase in carbon dioxide emissions is a major contributor to increasing global temperatures and climate changes due to the greenhouse effect. Recently, it has been reported by the United States environmental protection agency that the largest sources of greenhouse gas emissions in the United States come from human activities, mostly through burning fossil fuels for electricity, transportation, and industry (25%, 27%, and 24% greenhouse gas emissions, respectively). The combustion of fossil fuels is a major source of increasing carbon dioxide content and other gases in the atmosphere.

In terms of greenhouse emissions, it is fair to mention that CO₂ is not the only gas contributing to the greenhouse effect. In particular, chlorofluorohydrocarbons, NO_x, and CH₄ are also greenhouse gases which are much more destructive to the environment than CO₂.²

To end the climate crisis, various alternative renewable energy sources are being proposed for power generation, including solar cells, wind energy, biomass, and proton exchange membrane (PEMFC) fuel cells.

PEMFC technology is one of the best clean energy sources compared to traditional ones. This technology uses hydrogen as fuel; therefore, using hydrogen to produce power and zero-emission is highly welcome to avoid emissions causing the greenhouse effect. Hydrogen delivered to PEMFC is usually non-pure (contaminated by 0.5-1% CO) leading to a decrease in efficiency of PEMFC. Preferential oxidation of CO is a promising approach for CO removal from an H₂-rich stream. The discovery of Cerium supported Cu catalysts for CO oxidation at low temperatures inspired us to explore the activity and selectivity of this catalyst to oxidize of CO in the presence of high concentration of hydrogen (CO PROX). However, to minimize the oxidation of hydrogen by Cu NPs and thus increase CO₂-selectivity, our study was designed to explore the activity and selectivity of Cu single sites.³

1.2 Fuel cells and fuel processor

Over 100 years ago, fuel cell technology was discovered by Sir William Grove and Christian Friedrich Schoenbein.⁴ There are many kinds of fuel cells such as proton exchange membrane (PEMFC) fuel cells, alkaline fuel cells, solid oxide fuel cells, Phosphoric acid fuel cells, differentiated by the type of electrolyte which is separating the fuel from the oxygen. Depending on the characteristics of each category, they can be used for various applications. For example, PEMFC fuel cells are typically interesting for the automotive industry. In specific, a proton exchange membrane (PEMFC) fuel cell is a continuously operating galvanic cell which it can convert chemical energy directly into electricity through the reaction between hydrogen and oxygen. These devices are very interesting due to their high efficiencies relative to traditional combustion engines and zero emission, producing only heat and water as waste products. Using of these strategies is expected to grow as the energy sector moves toward hydrogen as an energy carrier.

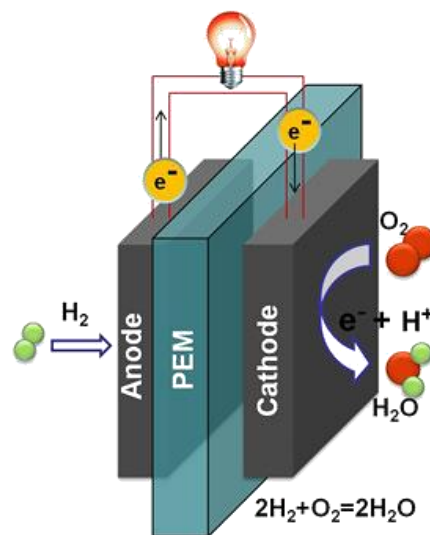


Figure 1.1. General scheme of a hydrogen fuel cell simple configuration.⁵

Figure 1.1 shows the schematic representation of the reactions in a fuel cell operating with hydrogen and air with a hydrogen-ion conducting electrolyte. The molecules of hydrogen are separated into ions and electrons when they flow over the anode. The electrons flow through the outer circuit energizing an electric load, and the hydrogen ions migrate through the ionically conducting but electronically insulating electrolyte to the cathode. Eventually, the electrons react with oxygen molecules on the surface of the cathode and hydrogen ions migrate through the electrolyte, producing water.

They could be used in various applications, including transportation, industrial, commercial/residential buildings, and long-term energy storage for the grid in reversible systems. The proton exchange membrane (PEMFC) fuel cell (Figure 1.1) has many attractive features, such as a low operating

temperature (80°C), sustained operation at high current density, low weight, cost-effective, quick start-up and shutdown.⁶

The PEMFC uses hydrogen as a fuel which can be produced by steam reforming of hydrocarbons or alcohols ($\text{fuel} + \text{O}_2 + \text{H}_2\text{O} \leftrightarrow \text{CO}_x + \text{H}_2$) followed by water gas shift reaction (WGSR) units ($\text{CO} + \text{H}_2\text{O} \leftrightarrow \text{CO}_2 + \text{H}_2$). The feed gas mixture obtained by these two processes always contains a typical composition of 45-75% H_2 , 15-25% CO_2 , 0.5-2% CO , 10-20% H_2O and N_2 .⁷⁻⁹ However, it has been reported that the anode catalyst of PEMFC is highly susceptible to be poisoned by CO , even in the presence of a tiny amount of CO in the hydrogen-rich stream at low temperatures,^{10, 11} which leads to decrease the efficiency of the fuel cell. Hence, it should be further reduced to a trace level below 10 ppm.¹²

1.3 Hydrogen purification methods

During the last decade, significant efforts have been made to develop advanced strategies for the selective removal of CO from the H_2 -rich stream without losing hydrogen. There are three approaches, such as H_2 -selective membranes,¹³ selective methanation,¹⁴ pressure swing adsorption and preferential oxidation of CO in hydrogen stream (PROX).¹⁵⁻¹⁸

H_2 -selective membranes can effectively remove CO by using a semi-permeable membrane that selectively allows hydrogen to pass through while preventing other gases. However, this technique requires relatively high pressure, and the best membranes are currently Pd-base, making it a costly method.¹⁹ In addition, these membranes are prone to embrittlement and hydride formation, which results in a loss of selectivity.²⁰

Selective methanation has also been widely used to remove CO in hydrogen reformat. Hydrogen is used to convert CO to CH_4 over ruthenium or nickel-based catalysts in this method. There are a few main disadvantages when this method is used: (i) CO conversion to methane requires hydrogen and, hence, reduces the amount of hydrogen which could potentially be utilized in the PEMFC since the conversion of one mole CO to methane consumes three moles of hydrogen (Eq. 1.1). (ii) The presence of a higher amount of CO_2 than CO in the hydrogen stream after steam reforming also leads to a decrease in the selectivity since CO_2 reduction to methane requires four moles of hydrogen which then increase the hydrogen consumption further in comparison to CO conversion to methane (Eq. 1.2).²¹

Due to the large dimensions and high costs of the compressor which is used to adjust a high pressure in order to separate the hydrogen from other gases, the pressure swing adsorption method is not suitable for non-stationary applications.²² It seems to be that the first three mentioned strategies, pressure swing adsorption, membrane separation and selective methanation are not very promising methods for PEMFC applications.



1.4 Preferential Oxidation of CO (CO-PROX)

Among the three purification methods mentioned above, the preferential oxidation of CO (CO-PROX) is a very attractive and promising method.²³ The main principle of this method involves the oxidation of CO to CO₂ by oxygen over heterogeneous catalysts in the presence of a hydrogen stream (1.3).

The advantage of this technique is a cost-effective industrial process compared to all processes already mentioned above and simplicity of implementation without significant hydrogen fuel loss.

Carbon monoxide at the outlet of the water gas shift reactor is selectively oxidized in the PROX reactor over oxidation catalysts using externally supplied oxygen. The following three reactions can be occurred in the PROX system.



The PROX catalysts must show high activity and high CO₂-selectivity, to avoid the undesired side reaction such as water formation (Eq.1.2) and CO-methanation (Eq.1.3). An efficient catalyst should be able to selectively oxidize 0.5-2% CO present in the reformat. Hydrogen is the primary component in the reformat, any oxidation of hydrogen by the catalyst would lead to a decrease in the overall fuel efficiency. Furthermore, the H₂O through hydrogen oxidation can have a negative impact on the catalytic activity of the catalyst. Therefore, the essential requirements for PROX catalysts are high CO oxidation and low hydrogen oxidation.^{9,24}

Based on the catalytic performance of the PROX reaction, active catalysts can be classified into two groups. The first group comprises noble metals, including (Pt, Au, and Ru) while the second group contains non-noble transition metals, such as Cu and Co.

1.5 Catalytic systems for the CO-PROX reaction: state of the art

Pt-based catalysts, which showed good resistance to the adsorption of CO₂ and H₂O,²⁵ are known as higher temperature CO-PROX catalysts with an optimal operating temperature being around 200 °C.²⁶⁻²⁸ However, Pt catalysts show higher intrinsic activity for H₂ rather than for CO oxidation. The selectivity to CO₂ (~40%) remains constant across a wide temperature range (170-300°C), indicating that the activation energies of CO and H₂ oxidation reactions are comparable. Gold-based catalysts have

also attracted great attention for PROX applications, especially Au supported on reducible oxides such as Au/CeO₂,^{29,30} Au/CeCuO_x,³¹ and Au/TiO₂³² due to their low temperature performance.^{29,30} Supported Rh and Ru catalysts have also been applied for CO-PROX, to some extent. However, they showed low CO₂ selectivity (about 25%) ,mostly due to the conversion of CO to methane.^{33,34}

Despite the superior activity of the supported noble metal catalysts, there are three main drawbacks preventing their practical large-scale applications: (i) agglomeration of Au species at high temperatures to large particles which leads to a decrease in the number of the active sites, (ii)

the low PROX selectivity of these catalysts due to the undesired oxidation of H₂ and/or CO reduction to methane, and (iii) their high cost and scarcity preventing them from sustainable large-scale applications.^{35,36} To overcome all these drawbacks, it is highly required to find alternatives to noble metals catalysts such as transition metal-based catalysts.

According to the literature, supported copper^{3,37-41} and cobalt⁴²⁻⁴⁴ catalysts based on reducible supports showed comparable activity and high selectivity at low temperatures for CO-PROX. Moreover, they are much cheaper than noble metal catalysts. However, Co catalysts have been used only to a small extent since the formation of carbonate intermediates in the presence of CO₂ poisoning the Co-catalysts and, hence, limits their application.^{45,46}

1.6 CuO/CeO₂ catalysts: state of the art

In recent years, copper ceria catalysts have emerged as outstanding catalysts for a number of heterogeneous catalytic reactions involving redox steps, such as methanol synthesis, low-temperature CO oxidation,⁴⁷ NO reduction,⁴⁸ N₂O decomposition⁴⁹ and water gas shift reaction.⁵⁰ These reactions play a critical role in fundamental and industrial processes.

Lately, comprehensive studies using Cu/CeO₂ catalysts have shown that these systems provide high performance for CO oxidation in the presence of hydrogen at a temperature window of 50–150 °C.^{15,39,51-53}

Most advanced studies of structure-reactivity relationships showed that the high catalytic activity of CuCeO₂ catalysts typically attributed to the synergistic redox behaviour between copper and CeO₂, which is the key to forming a high amount of oxygen vacancies, and therefore, generating redox-active Cu²⁺/ Cu¹⁺ and Ce⁴⁺/ Ce³⁺ pairs.

Using ceria as a support is specifically advantageous for CO oxidation reaction and PROX, due to its capability to store and release oxygen under oxidizing/reducing conditions. An improved oxygen storage capacity (OSC) can be obtained through ceria doping. Substituting some of the Ce species in the fluorite structure is introduced a lattice strain that weakness Ce-O bonds and thus decreasing the oxygen vacancy formation energy and thus enhances oxygen ion diffusion.⁵⁴⁻⁵⁷

The redox behavior of CeO₂ can even be improved when isovalent cations such as Zr⁴⁺, Ti⁴⁺ and Sn⁴⁺ are incorporated into Ce lattice positions which are known to enhance the oxygen mobility and reducibility of CeO₂.⁵⁸ However; it has been reported by Chang et al. that the catalytic performance of CO₂ hydrogenation to methanol over Cu-CeTiO₂ was 4-260 times higher than over the corresponding binary CuTiO₂ and CuCeO₂ materials, respectively, due to a significant synergistic effect between CeO₂ and TiO₂.⁵⁹ Ching et al. have shown that the CO oxidation rate was dramatically improved by increasing the amount of Ce additive deposited on Cu/TiO₂. This superior catalytic activity was attributed to the presence of small CeO₂ particles on TiO₂ and highly dispersed Cu-Ce species which caused a high amount of Ce⁺³ and abundant oxygen vacancies.⁶⁰

Zhiwei et al. have prepared a series of CuO/Ce_{1-x}Ti_xO₂ catalysts by sol-gel impregnation and tested them under CO-PROX conditions, whereby the catalyst CuO/Ce_{0.8}Ti_{0.2}O₂ exhibited the highest activity compared to pure CeO₂ and TiO₂. The authors concluded that the excellent activity of CuO/Ce_{0.8}TiO₂ may be contributed to the strong interaction between TiO₂ and CeO₂ in the support as well as the interfacial between CuO and the support.⁵²

Chen et al. reported that the CO₂ selectivity was significantly improved when Sn⁴⁺ ions were incorporated in CeO₂ to form CuO/Ce_xSn_{1-x}O₂ catalysts.⁶¹ Also, they found that appropriate amounts of Zr⁴⁺ incorporated into CeO₂ to form CuO/Ce_xZr_{1-x}O₂ and CuO/Ce_xZr_{1-x}O₂-Al₂O₃ catalysts could not only enhance the mobility of lattice oxygen but also improve the activity and CO₂-selectivity.^{62, 63} However, it is also noteworthy that modifying of CeO₂ with other elements did not always improve the activity of CuO/CeO₂ catalyst in CO oxidation. Ratnasamy et al. have prepared a series of CuO-CeO₂, CuO-CeO₂ZrO₂ and CuO-ZrO₂ materials by a coprecipitation method and tested them under CO-PROX reaction conditions. They observed that CuO-CeO₂ showed higher activity than CuO-CeO₂ZrO₂ and CuO-ZrO₂.⁶⁴ Manzoli et al. and Caputo et al. also found that doping cerium with zirconia had no positive effect on CO-PROX performance.^{65, 66}

The metal dispersion and redox properties are not only enhanced by added isovalent elements but also can be significantly improved when CuO/CeO₂ catalysts modify with another promoter such as iron or Nickel. It was reported that the modification of iron and nickel oxides increased the catalytic activity of CuO/CeO₂ catalysts in CO-PROX despite the Cu-content in this catalyst was very low; this suggests that the role of iron and nickel in the redox cycle.⁶⁷

Jichang et al. reported that the addition of Fe to CuO/CeO₂ led to an increase in the turnover frequency from 3.62×10^{-2} to $4.50 \times 10^{-2} \text{ s}^{-1}$, since Fe was incorporated into the CeO₂ lattice, which led to the formation of Fe-O-Ce moieties and oxygen vacancies. Moreover, the resistance against CO₂ and H₂O was enhanced, and the long-term stability was largely improved from 170 to 400 h.⁵⁷

The synthesis procedure plays a significant role in the catalytic properties of the base metal catalysts. Liu et al. studied the influence of the preparation method, and they reported that CuO/CeO₂ catalysts prepared by co-precipitation have a lower catalytic activity for the preferential oxidation of CO in excess hydrogen compared to similar catalysts prepared by a chelating method.⁴⁰

Another study by Avgouropoulos et al. reported that the ranking of the activity of CuO/CeO₂ catalysts which have been prepared by various preparation methods is as follows: urea-nitrates combustion > citrate-hydrothermal > coprecipitation > impregnation method. The physicochemical characterization of the samples revealed that the urea-nitrates combustion and citrate-hydrothermal preparation methods produced a higher amount of easily reducible copper oxide strongly interacting with the surface of CeO₂, while coprecipitation and impregnation methods produced a large amount of copper particles weakly associated with CeO₂ surface.⁶⁸

Tremendous efforts have been made in the past 20 years to gain a deeper understanding of the origin and nature of the active site(s) responsible for PROX in the Cu/CeO₂ catalyst. Yet still these issues are not fully understood. Some investigations have shown that the conversion of CO to CO₂ in the presence or without H₂ largely depends on the Cu⁺-CO species.⁶⁹⁻⁷³

Yao et al. have used a combined operando XANES/DRIFTS technique to study the mechanism of the CO + O₂ process (3.3% CO/, 1.7% O₂/He) without H₂, over a CuO/ CeO₂ catalyst, and showed that highly dispersed Cu⁺ ions on the catalyst surface were the active species for CO oxidation.⁷⁴ This is consistent with the active site which was identified in the CO-PROX reaction.^{60, 75, 76}

However, few details on the local structure of active species in CuCeO₂ catalysts have been found for CO-PROX. By using EXAFS, Zhang et al. have identified the local coordination of the active oxygen ions and the active Cu species in ceria-supported copper catalyst under real CO-PROX conditions.⁷⁷ They have established that the active/labile oxygen is the first oxygen neighbour of Cu²⁺ species that isolated with CeO₂ in a mixed oxide solution of CuCeO₂.

Other authors postulated that isolated Cu single sites at the interface between CuO and CeO₂ particles are responsible for the high CO conversion rate while Cu_yCe_{1-y}O_{2-x} solid solutions were less active.^{78, 79}

X-ray absorption spectroscopic investigations confirmed that the transition metal (copper) species are stabilized in the 3+ oxidation state upon incorporation into the CeO₂ lattice.⁸⁰ In opposition to previous reports suggesting Cu⁺ or Cu²⁺ to be the active sites for catalysis. Joseph et al. reported that the high catalytic activity of Cu_{0.1}Ce_{0.9}O_{2-x} is due to the accessible Cu³⁺/Cu²⁺.⁸¹

In a few reports, Cu-Cu dimers have also been claimed to be active sites for CO oxidation.^{82, 83}

Recently it has been reported that atomically dispersed Cu⁺ cations supported on a zirconia-based metal-organic framework (MOF), Cu/UiO-66, are highly active for CO oxidation both in hydrogen or without hydrogen at high temperatures (above 200 °C).⁸⁴

In most studies of CO oxidation in the presence or absence of hydrogen between 2010 and today, Cu contents of about 10-5 wt% have been used to prepare ceria supported Cu catalysts, and such high contents led to the formation of different copper species (single atoms sites, dimers, oligomers, clusters and nanoparticles).^{15, 41, 47, 57, 85-87} Due to this, it is hard to obtain reliable information about the active sites. In contrast, our group has recently published highly active Cu/CeO₂-TiO₂ (Ce/Ti ≈0.3) catalysts for CO oxidation with Cu contents well below 1 wt%. In these catalysts, single Cu ions exposed on the surface of CeO₂ particles were identified as active sites based on results from a comprehensive multimethod analysis. It was found that oxygen for CO oxidation is provided by reversible Cu²⁺-O-Ce⁴⁺ ⇌ Cu⁺-□-Ce³⁺ redox shuttles on the catalyst surface.⁸⁸ With these catalysts, unprecedented Cu-based CO oxidation rates have been obtained.

1.7 Objective

The use of noble metals-based catalysts in the preferential oxidation of CO is not highly desirable for industrial applications due to the elevated cost and lower CO₂-selectivity. Therefore, Cu catalysts represent a cheap and available alternative for those processes traditionally based on noble metals catalysts. The recent discovery of high activity and selectivity properties in the CO-PROX process of copper oxide catalysts supported on ceria has renewed interest in materials other than noble metals. However, an urgent need to enhance the catalytic performance of PROX catalysts by maximizing both the CO oxidation rate and the CO₂ selectivity at low temperatures.

Based on the previous studies which were used CuCeO₂ catalysts for CO-PROX reaction, there are many conflicting's and open questions about the nature of active sites over CuCeO₂ system, specifically: i) What is the redox-active couple of Cu (Cu³⁺/Cu²⁺) or (Cu²⁺/Cu⁺), ii) which is the structure of the active sites for CO oxidation, Cu single sites or CuOx particles.

To efficiently answer these questions, a targeted comparison of catalysts containing varying proportions of CuO clusters and Cu single sites should be conducted. By systematically reducing the Cu content, it is possible to induce a transition from a predominantly cluster-based system to one that is enriched with the desired single sites.⁸⁹ Therefore, the aim of this Ph.D. thesis to enhance the atomically dispersed Cu single-atom catalysts (Cu-SAC) using a highly dispersed CeO₂ on TiO₂ and a commercial pure CeO₂.

To achieve this goal, special attention is dedicated to the impact of the preparation method and the identification of active sites and reaction mechanisms using a combination of various in-situ spectroscopies under the most relevant reaction conditions. To this end, the following aspects have been investigated:

- Preparation of Cu/CeTiO₂ (Ce/Ti ratio = 0.18) catalyst with very low Cu loading (0.05 wt%) by sol-gel method to demonstrate that Cu-SAC on CeO₂ is highly active and stable for CO-PROX reaction (section 3.1).
- Explore the opportunity to prepare Cu-SAC supported on highly reducible and available commercial CeO₂ by using a ball-milling and thermal annealing method (Section 3.2) and maximize the number of the active sites by increasing the Cu loading (0.23, 0.5 and 1 wt%).
- Study the effect of the oxygen vacancies, oxygen mobility, and redox properties of different commercially available CeO₂ supports having different crystallite sizes (3 and 25 nm) on the catalytic activity and selectivity of Cu_{0.2}CeO₂ during CO-PROX reaction (Section 3.3).

Among the various spectroscopic techniques, in-situ electron paramagnetic resonance (EPR) spectroscopy was used to monitor and characterize different Cu species and their redox behaviour during PROX conditions. In-situ infrared spectroscopy in diffuse reflectance mode (DRIFTS) was performed to identify the adsorbed surface species as a basis for deriving the reaction mechanism. Near ambient pressure X-ray photoelectron spectroscopy (NAP-XPS) was applied to follow changes in the oxidation state of the Ce species on the surface of the materials under reaction conditions. Moreover, basic characterization techniques such as X-ray diffraction (XRD), determination of the specific surface area by the Brunauer/Emmet/Teller method (BET), scanning transmission electron microscopy (STEM), inductively coupled plasma-optical emission spectrometry (ICP-OES), hydrogen temperature programmed reduction (H₂-TPR), and Raman spectroscopy were used to characterize the structure of the catalysts.

2 Experimental section

Since the present work aims to improve the catalytic performance of the CeO₂ supported Cu catalysts to reduce CO in the hydrogen rich stream. Various supports such as CeO₂-TiO₂ and CeO₂ (commercial) with different texture properties have used to prepare a highly active Cu single atom catalysts for preferential CO oxidation. In this section, preparation procedures of the support and Cu-containing catalysts are described. Then, PROX activity tests are described, including calculation of CO oxidation rate normalized on copper, CO conversion and CO₂-selectivity. In the following section, the basic concept, and the purpose of all the characterizations followed by their experimental descriptions are explained.

2.1 Catalyst preparation

2.1.1 Sol-gel method

To prepare highly active and selective Cu single atom catalyst supported by CeTiO₂ for PROX reaction (section 3.1.1). Cu_xCeTiO₂ (x = 0.05 wt%) catalyst was prepared by sole-gel method.^{3,55} All chemicals used in this method were obtained by Sigma-Aldrich with 98-99% purity. The support (CeO₂-TiO₂) with a fixed Ce/Ti molar ratio of 0.2 and the copper containing catalyst were prepared by a sol-gel method as follows: An amount of 1.37 g of (NH₄)₂Ce(NO₃)₆ salt was dissolved in 8.75 ml of anhydrous ethanol at 60 °C with continuous magnetic stirring until a homogeneous solution was obtained. A complexing agent of 3.75 mL of Ti⁴⁺ isopropoxide and 1.62 mL of ethyl acetoacetate was added to the Ce⁴⁺ salt solution. The mixture was then magnetically stirred at room temperature for 1 h. After that, 2.25 mL HNO₃ solution (0.1M) was added dropwise under continuous stirring to form a suspension by hydrolysis, which turned under stirring into a spongy orange gel. The gel was eventually extracted under supercritical conditions by ethanol in an autoclave (T = 245 °C, p = 60 bar) to create an aerogel, followed by calcination at 500 °C for 3 h in static air. The Cu/CeO₂-TiO₂ catalyst with 0.05wt% of copper, was synthesized using a one-step sol-gel method as described above for the pure support CeO₂-TiO₂ by adding CuCl₂.2H₂O to the Ce and Ti precursors in anhydrous ethanol. The product was extracted under supercritical conditions by ethanol, as mentioned above. Finally, the solid catalyst was calcined at 500 °C in static air for 3 h.

2.1.2 Ball-milling method

To increase the atomic efficiency on the surface of highly dispersed cerium oxide and avoid the complexity of sol-gel method used in previous section (3.1). A ball milling method was used to prepare three catalysts with different Cu loadings supported on commercial cerium oxide (Merck).

Briefly, appropriate amounts of copper nitrate trihydrate $\text{Cu}(\text{NO}_3)_2 \cdot 3\text{H}_2\text{O}$ (0.023, 0.047 and 0.095 mg), and 2.45 g of CeO_2 were placed in an agate mortar with adding 5 ml of acetone to better increase the dispersion of Cu on the CeO_2 support. The mixture was grounded manually for 15-20 min, and a homogeneous pale green powder was obtained. After that, the solid powder was milled at 3 r/min for one hour with a mass ratio of ball to the solid powder of 76:1 (190 g ball per 2.5 g powder) at room temperature under ambient conditions. Finally, the catalysts were subsequently calcined in static air for 5h at 500 °C (thermal ramp rate 3 °C/min). The catalysts obtained by this method were named as Cu_xCeO_2 ($x = 0.25, 0.5$ and 1 wt%) (section 3.2).

To study the influence of redox properties, crystallite sizes and reducibility on the catalytic performance, a ball milling method was also used to prepare Cu catalysts on CeO_2 with different crystallite sizes (25 nm (Sigma-Aldrich) and 3 nm (Thermo Fischer Science.)) with 0.25 wt% Cu. The characterization and the catalysts' performance of these two catalysts are discussed in section 3.3. The obtained catalysts were named according to the crystallite size of the support. For example, the $\text{Cu}_{0.25}\text{CeO}_2\text{-3nm}$ catalyst indicated that the crystallite size of the support used in this catalyst is 3nm; other catalyst was named as the $\text{Cu}_{0.25}\text{CeO}_2\text{-25nm}$. Cu catalysts used in the present investigations, which are prepared by sol-gel and ball-milling, are identified in Table 2.1.1.

Table 2.1.1. Molecular formula, Cu loadings and preparation methods of prepared Cu catalysts used in the present work.

Cu catalysts	Cu loadings Wt%	Preparation method
$\text{Cu}_{0.05}\text{CeTiO}_2$	0.05	Sol-gel
$\text{Cu}_{0.25}\text{CeO}_2$	0.25	Ball-milling
$\text{Cu}_{0.5}\text{CeO}_2$	0.5	
Cu_1CeO_2	1	
$\text{Cu}_{0.25}\text{CeO}_2\text{-25nm}$	0.25	Ball-milling
$\text{Cu}_{0.25}\text{CeO}_2\text{-3nm}$	0.25	Ball-milling

2.2 PROX activity test

The PROX catalytic activity tests were performed using 100 mg of sieved material (250-315 μm) in a continuous-flow fixed-bed quartz reactor (length 200 mm, internal diameter 6 mm). The feed contained 1% CO , 1% O_2 and 80% H_2 and the rest He in a total flow of 30 ml/min, corresponding to gas hourly space velocity (GHSV) of 18000 $\text{ml} \cdot \text{g}^{-1} \cdot \text{h}^{-1}$. Before starting the experiment, the catalyst was activated in 10% of hydrogen for 1 hour at 250 °C, and then cooled down to 50 °C in He to switch on the inlet feed mixture in order to start the reaction at a temperature range 50-150 °C.

The CO₂ product and un-converted molecules were analyzed by using online chromatography (Shimadzu), which it was equipped with two columns, a Molsieve 5 Å to separate CO, O₂, and H₂, and a Poraplot-Q to isolate CO and CO₂. The CO conversion rate normalized to the mass of copper, CO conversion, and CO₂-selectivity were calculated by using the (Eq.2.1), (Eq.2.2) and (Eq.2.3). The intrinsic catalytic activity constant k_L has been calculated by using the (Eq. 2.4)⁹⁰ in which P_{CO} and P_{O_2} are the partial pressures of CO and O₂ and K_L is the CO adsorption equilibrium constant. Lopez et al. used k_L in an attempt to rank copper-based CO-PROX catalysts from literature⁹¹ and we used the same approach to compare the intrinsic activity of Cu_{0.05}CeTiO₂ catalyst (section 3.1) with the state of the art.

$$\text{Reaction Rate} = \frac{X_{CO} \times n_{CO,in}}{m_{Cu}} \quad (2.1)$$

$$X_{CO} (\%) = \frac{n_{CO,in} - n_{CO,out}}{n_{CO,in}} \times 100 \quad (2.2)$$

$$S_{CO_2} = \frac{n_{CO,in} - n_{CO,out}}{n_{O_2,in} - n_{O_2,out}} 0.5 \times 100 \quad (2.3)$$

$$k_L = \frac{r_{CO}(1 + K_L \cdot P_{CO})}{K_L \cdot P_{CO} \cdot P_{O_2}} \quad (2.4)$$

$$K_L = 7.53 \exp\left(\frac{8700}{RT}\right) \quad (2.5)$$

2.3 Catalyst characterization techniques

Characterization is essential in any practical catalytic study and industrial application since it provides necessary parameters, such as structure and chemical composition, texture properties, and surface properties which are related to catalytic activity. The catalysts were characterized by ICP-OES, BET, XRD, (HAADF-TEM with EEL and EDX elemental mapping techniques), Raman, H₂-TPR, DRIFT, EPR, NAP-XPS.

2.3.1 Inductively coupled plasma optical emission spectrometry (ICP-OES)

It is not uncommon for the composition of a catalyst at the end of preparation to be different from the expected stoichiometry of the target compound. This can be due to several factors, including incomplete reaction, impurities in the starting materials, or side reactions that result in the formation of unintended products. Hence, for comparing catalytic activity, it is crucial to check the elemental composition of synthesized materials. ICP-OES (Inductively Coupled Plasma Optical Emission Spectroscopy) is a powerful analytical technique used to determine the elemental composition of materials. In this method, the sample is first digested in an acid to dissolve all the metal ions existing. The resulting solution is then introduced into an inductively coupled plasma source where it is atomized, excited, and ionized. The high temperatures in the plasma source cause significant amounts of collisional excitation, resulting

in the emission of light at characteristic wavelengths. The atomic emission from the plasma is then collected using a lens or mirror and imaged onto the entrance slit of a wavelength selection device such as a grating or prism. The device separates the emitted light into its component wavelengths, which are then detected using a photomultiplier tube or a charge-coupled device. The intensity of the emitted light at each wavelength is proportional to the concentration of the corresponding element in the sample. By measuring the intensities of the emitted light at specific wavelengths for each element of interest, the weight percentages of the metal ions in the sample can be quantified.⁹²

Experimental description: In a typical procedure, the sample (10 mg) was dissolved in an acidic mixture of 8 ml aqua regia and 2 ml hydrofluoric acid. Then, the mixture was treated by microwave-assisted equipment at 200 °C and 60 °C. The solution was diluted with 90 ml of distilled water and analyzed by using Varian 715-ES ICP-emission spectrometer and the ICP Expert software.

2.3.2 X-ray diffraction (XRD)

X-ray diffraction (XRD) is one of the most important non-destructive tools to identify the crystalline phases, crystallite sizes, and disorder of the materials. The X-ray Diffraction technique works based on the interaction between the electron cloud of the atoms present in the material and the X-ray radiation, which leads to diffraction effects when the X-ray radiation passes through the material with geometrical changes on the length scale of the radiation wavelength. Due to the similarity in scales between the distances between the atoms and the wavelength of X-rays, phenomena such as constructive and destructive interference occur when these materials are exposed to X-rays (Figure 2.1).⁹³ These phenomena result in diffraction patterns where X-rays are scattered at specific angles depending on the distance between the atoms within a sample. By analysing the intensity and position of these diffraction peaks, important information about the crystal structure and composition of the material can be obtained, which is particularly useful in catalysis for understanding the active sites catalysts.

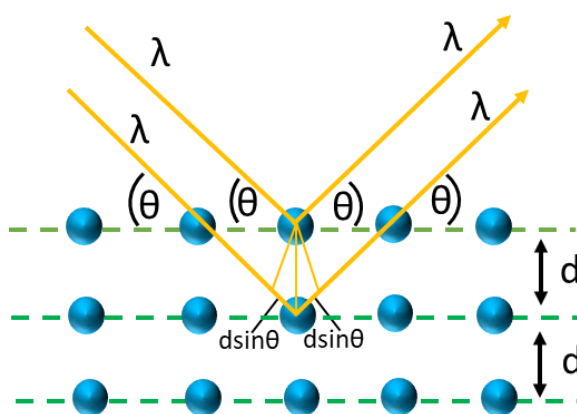


Figure 2.1. Visualization of Bragg diffraction.

Crystals exhibit multiple sets of planes with different interplanar distances. X-rays are diffracted from these planes at characteristic diffraction angles. The relationship between the wavelength of the X-rays, the atomic spacing within the crystal lattice, and the diffraction angle is described by the Bragg equation (2.6). This equation states that for a particular reflection order (represented by the integer "n"), the wavelength of the incident X-ray beam (represented by " λ "), the distance between parallel lattice planes (represented by "d"), and the angle of diffraction (represented by " θ ") are related as follows:

$$n \cdot \lambda = 2d \cdot \sin \theta \quad 2.6$$

Experimental description: At room temperature, the XRD powder patterns were recorded by using a $\theta/2\theta$ diffractometer (a X'Pert Pro, Panalytical, Almelo, Netherlands), which is equipped with a X'Celerator RTMS Detector and Cu K α radiation ($\lambda = 1.5418 \text{ \AA}$, 40 kV, 40 mA). The 2θ data were collected in the range from 5 to 80 °C. The WinXPOW by STOE&CIE program with an inclusion of the Powder Diffraction File PDF2 of the ICDD (International Centre of Diffraction Data) was used to determine the phase composition of samples.

2.3.3 Low-temperature N₂ adsorption

In the field of heterogeneous catalysis, it is widely known that a better understanding of catalytic behaviour can be achieved through knowledge of the surface area and pore properties. Thus, the surface area, specific pore volume, and pore size distribution are considered to be exceptionally important factors. Consequently, determining these properties is highly attractive. The Nitrogen adsorption technique at its boiling point temperature (77K) is most commonly used for this purpose. The surface of solid materials is exposed to the liquid nitrogen. Brunauer-Emmett-Teller (BET) theory is a widely utilized technique to determine the surface area of solid porous materials.⁹⁴ It is as follows.

$$\frac{P}{V(P_0 - P)} = \frac{(C-1)}{V_m \cdot C} \cdot \frac{P}{P_0} + \frac{1}{V_m \cdot C} \quad 2.7$$

P is the equilibrium pressure for a specific surface coverage

P₀ is the saturation pressure of adsorbates at the temperature of adsorption

V is the volume of adsorbed gas

V_m is the monolayer adsorbed gas quantity

c is the BET constant

$$c = \exp\left(\frac{E_1 - E_L}{RT}\right) \quad 2.8$$

Where E₁ is the heat of adsorption for the first layer

E_L is the heat of adsorption for the second and higher layers and is equal to the heat of liquefaction or heat of vaporization.

Equation (2.7) represents an adsorption isotherm, which can be graphed as a straight line with the y-axis representing $1/[V(P-P_0)]$ and P/P_0 is the x-axis. This graphical representation is referred to as a BET plot. The linear relationship described by this equation holds within the range of $0.05 < P_0/P < 0.35$. To calculate the monolayer adsorbed gas quantity (V_m) and the BET constant (c), the slope (A) and y-intercept (I) of the line are utilized. The following equations (2.9 and 2.10) can be employed for these calculations:

$$Vm = \frac{1}{A+I} \quad 2.9$$

$$c = 1 + \frac{A}{I} \quad 2.10$$

The BET method is a commonly employed technique in materials science to determine the surface area of solids through physical adsorption of gas molecules. It allows for the calculation of both the total surface area (S_{total}) and the specific surface area (S_{BET}), which can be expressed as follows:

$$S_{total} = \frac{Vm \cdot N \cdot S}{V} \quad 2.11$$

$$S_{BET} = \frac{S_{total}}{a} \quad 2.12$$

V_m is the units of the monolayer volume of the adsorbate gas.

N is the Avogadro number ($6.02214076 \times 10^{23}$)

S is the adsorption cross section of the adsorbate

V is the molar volume of the adsorbate gas

a is the mass of the solid sample or adsorbent.

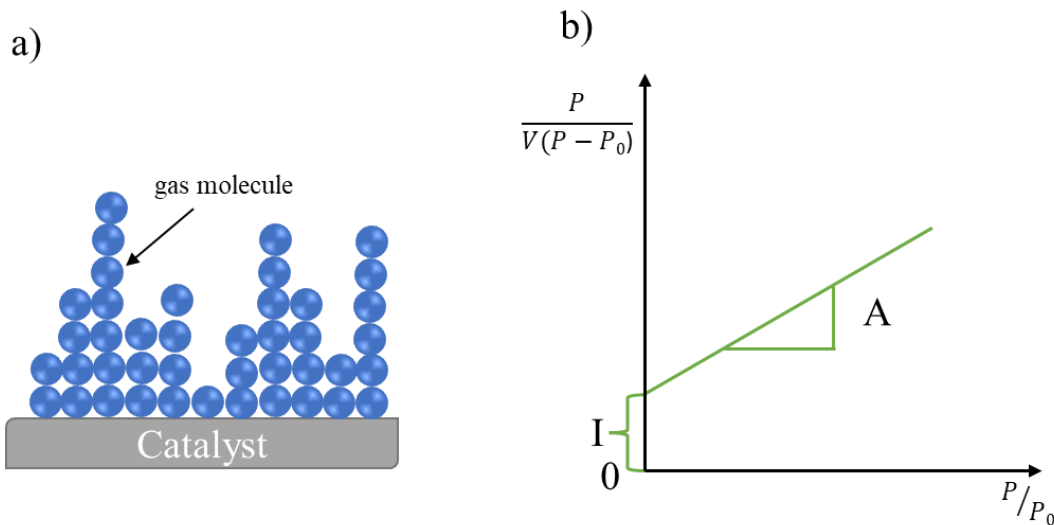


Figure 2. 2. a) is the BET model of multilayer adsorption on the surface of the catalyst, b) BET plot results.

Experimental description: Brunauer-Emmett-Teller (BET) method, the measured N₂ adsorption at 77k were used to calculate the BET surface area and pore volume using a Micromeritics, ASAP 2010 apparatus (Micromeritics GmbH, Aachen, Germany). Before starting the analysis, the sample was vacuumed at 200 °C at 0.01 bar for three hours.

2.3.4 Scanning transmission electron microscopy (STEM)

STEM is commonly utilized to indicate the size of the particles existing in the sample, particularly in the nanometer range and it provides information related to the morphology, composition, and distribution, making it a valuable technique for research and development in both academic and industrial settings. With advancements in technology, the STEM can now even monitor samples with atomic resolution, enhancing its capabilities and contributions to scientific inquiry. In STEM, electrons are used instead of light when compared to light microscopy. However, STEM operates on the same principle of light microscopy. The aid a high voltage (around 200 KV), an electron gun emits electrons, which are then directed through a series of electromagnetic lenses and tightly focused into a narrow beam. The electrons pass through the thin materials (around 100 nm) and the unscattered electrons produce an image on the fluorescent screen at the bottom, then a CCD camera can be utilized to collect the image in the computer. In our facility, STEM is attached to the energy dispersive spectroscopy (EDS) which is used to conduct the elemental analysis of the materials. Every element possesses a distinct atomic structure that results in unique X-ray emission energies. When high-energy photons or electrons collide with the specimen's electron shells, they excite the electrons, causing them to be knocked out from the inner shell and leave a hole. As a result, an electron from a higher-energy shell fills the gap and produces an X-ray that corresponds to the energy difference between the two shells. The detector recognizes the X-ray signal, and a crystal inside the detector turns the signal into an electrical voltage signal. The pulse processor measures the electrical signals, which are then transmitted to the analyzer.

Experimental description: Scanning transmission electron microscopy (STEM) experiments were carried out with an aberration-corrected JEM-ARM200F (Jeol, Corrector: CEOS) at 200 kV, also the microscope is equipped with a Gatan Enfium ER electron energy loss spectrometer (EELS) and JED-2300 (JEOL) energy-dispersive X-ray (EDX) spectrometer having a silicon drift detector (dry SD60GV) (Figure 2.3). The Annular Dark Field (ADF) detector was used to obtain the positional reference image during the EELS acquisition. For STEM imaging, a High-Angle Annular Dark Field (HAADF) and an Annular Bright Field (ABF) detector were used. Without further treatment, the dry powder samples were placed onto a copper grid or nickel grid with holey carbon film (mesh 300), which was then transported to the microscope.

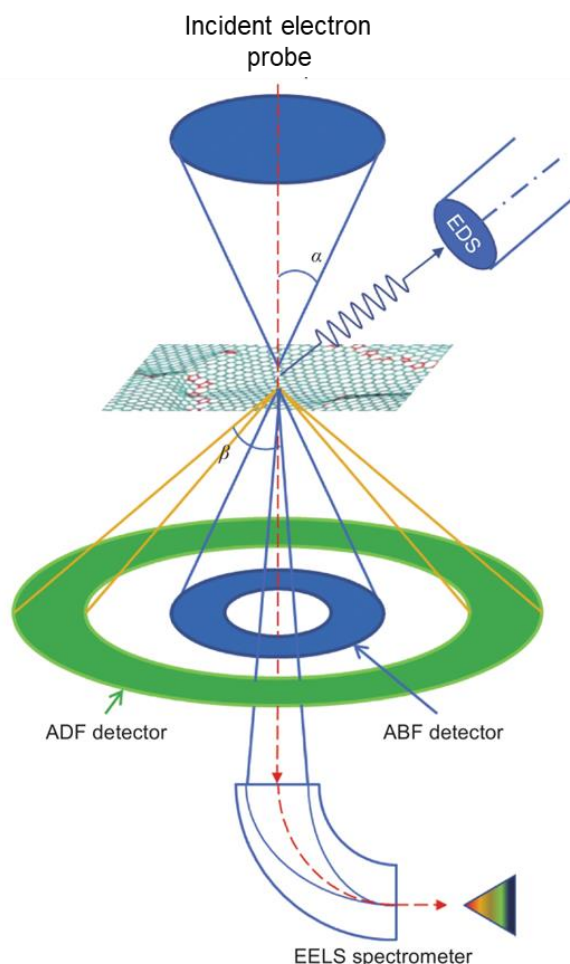


Figure 2.3. Schematics of STEM imaging showing various detectors (Adapted from ref.⁹⁵).

2.3.5 Temperature programmed reduction by H₂ (H₂-TPR)

The redox properties of copper deposited on Ceria are essential for improving its performance over CeO₂-based catalysts at low temperatures. The H₂-TPR technique is widely used to characterize the reducibility of catalysts. Reduction peaks corresponding to different species are observed at the temperatures required for their complete reduction. The amount of hydrogen consumed during the reduction process can be used to quantify the reduction capacity of the active species.

Experimental description: H₂-temperature-programmed reduction (TPR) was carried out using an Autochem II 2920 instrument (Micromeritics, Norcross, USA). A U-shaped quartz reactor was employed to load 200 mg of the sample. Before starting the measurement, the samples were pre-oxidized under the flow of 5% O₂/He (50 ml/min) at 400 °C with a heating ramp of 10k/min. For 30 min, the temperature was held to remove any adsorbed species, and then the system was cooled down to room temperature under 5% O₂/He. The TPR experiments were performed from room temperature to 900 °C in 5% /H₂/ Ar flow (50 mL min⁻¹) with a heating rate of 10k min⁻¹. A thermal conductivity detector

(TCD) was used to record the hydrogen consumption peaks. The quantity of hydrogen consumed was determined from the peak area.

2.3.6 Laser Raman spectroscopy (Raman)

Raman spectroscopy, which falls under the category of vibrational spectroscopy, was initially observed experimentally by Raman and Krishnan in 1928.⁹⁶ This spectroscopic technique focuses on the measurement of frequency shifts in the light that is scattered inelastically by materials when photons from the incident light interact with molecules and generate scattered photons (Figure 2.4). The difference in frequency between the incident and scattered light is called Raman shift (calculated by equation 2.13), which is provided information of lattice vibrations.⁹⁷

$$\text{Raman shift} = \frac{1}{\lambda_0 - \lambda} - \frac{1}{\lambda_0} \text{ (cm}^{-1}\text{)} \quad 2.13$$

λ_0 is the wavelength of the excitation laser, and λ is the wavelength of the Raman scatter in cm^{-1} .

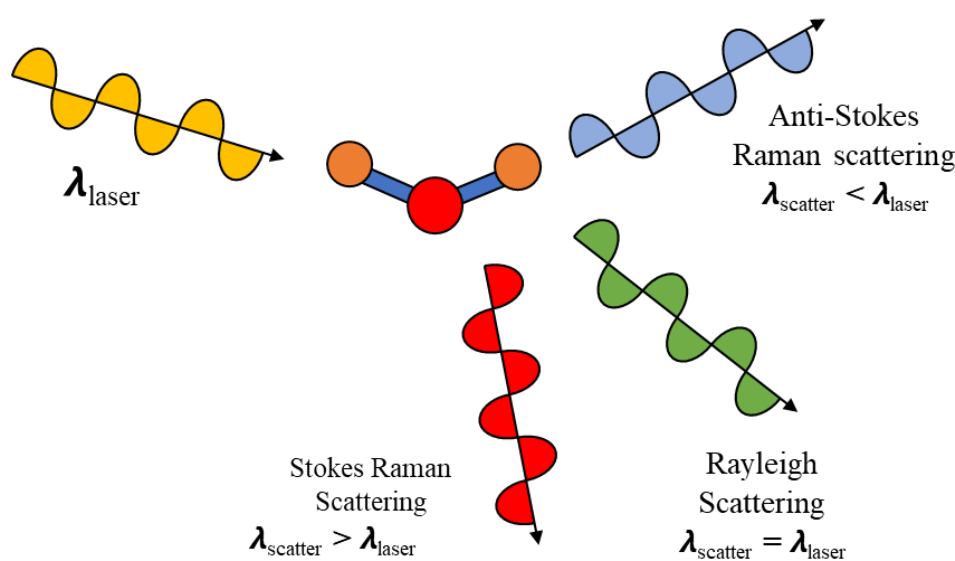


Figure 2.4. The Three kinds of scattering processes that can occur when light interacts with a molecule.

In most scattering events, the energy of a molecule remains the same after it interacts with a photon; therefore, the scattered photon has the same energy and wavelength as the incident photon. This type of scattering is known as Rayleigh scattering and is a dominant process. Especially this kind of scattering energy is used to determine the structure of molecules. While during the scattering, the molecule gains energy from the photon, and then the scattered photon loses energy, and its wavelength increases. This is called Stokes Raman scattering. On the contrary, if the molecule's energy loses by relaxing to a lower vibrational level and the scattered photon gains the corresponding energy, its wavelength decreases, called Anti-Stokes Raman scattering (Figure 2.5).

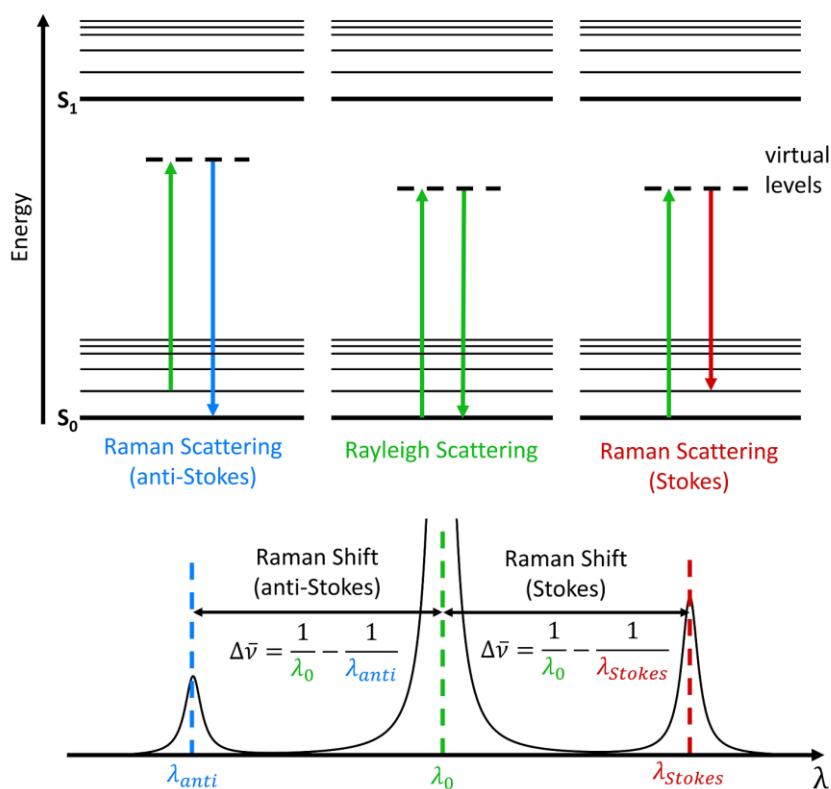


Figure 2.5. Jablonski Diagram showing the origin of Rayleigh, Stokes and Anti-Stokes Raman Scatter (Adopted from ref.⁹⁸).

Today, Raman spectroscopy is a highly effective technique in the field of catalysis. It is widely used to analyze catalyst structures and investigate chemical reactions occurring on the bulk and surface of catalysts under reaction conditions. Raman spectroscopy technique has a lot of advantages, such as offering exceptional resolution (around 1 cm^{-1}) and a broad spectral range ($50\text{-}5000 \text{ cm}^{-1}$), enabling the study of molecular vibration features (e.g., NH_3 , peroxide ions), and identification of crystalline oxide phases and determination of the structure of non-crystalline surface species. Due to all these advantages, Raman spectroscopy has been extensively applied in heterogeneous catalysis.

Experimental description: Raman spectra were recorded with a Horiba Jobin Yvon LabRam micro spectrometer iHR 550 using a 660 nm laser. An entrance slit in the spectrometer of $200 \mu\text{m}$ and a diffraction grating of 1800 mm^{-1} were used. To check the homogeneity of the sample, the spectra were obtained at different points of the sample by using a laser power on the samples of ≈ 0.1 to $\approx 10 \text{ mW}$ with a power density of $2.8 \times 10^5 \text{ W}\cdot\text{cm}^{-2}$. Data analysis was performed by LabSpec 6, Jobin Yvon Horiba built-in software.

2.3.7 Operando Diffuse Reflectance Infrared Fourier Transform Spectroscopy (DRIFTS)

The surface properties of catalysts play a crucial role in heterogeneous catalytic reactions. To gain insights into the interaction between adsorbed molecules and the catalyst, it is essential to employ

appropriate vibrational spectroscopic techniques like FTIR spectroscopy. This method allows for the direct monitoring and analysis of molecular interactions occurring on the catalyst's surface.⁹⁹ In addition, employing in situ FTIR approaches offers valuable insights into the nature of surface sites on a catalyst such as acid, base, and redox sites, during catalytic reactions. This information is crucial for developing a comprehensive understanding of the underlying mechanisms of the catalytic reaction. The electric field component of light in the infrared region is responsible for inducing transitions between two vibrational states of a molecule. IR radiation can be divided into three main regions: the far-IR (<400 cm⁻¹), the mid-IR region (400-4000 cm⁻¹) and the near-IR (13000-4000 cm⁻¹). In heterogeneous catalysts, the mid-infrared region is the most attractive for adsorbate studies as most of the molecular vibrations are excited with the radiation of this region. The infrared absorption frequency of a heteronuclear diatomic molecule's stretching vibration is influenced by the bond strength (expressed by the force constant, f) and the reduced masses (μ) of the bonded atoms. In this simplified model, the molecule can be envisioned as two masses connected by a spring, where the bond distance oscillates around an equilibrium position. When the bond is stretched or compressed beyond this equilibrium, the potential energy of the system increases. Like a harmonic oscillator, the bond's energy oscillates between kinetic and potential forms as it vibrates. The resonance frequency of vibration of a bond is given by the equation (2.14)

$$\nu = \frac{1}{2\pi} \sqrt{\frac{f}{\mu}} \quad 2.14$$

ν is the resonance frequency of vibration

f is the force constant

μ is the reduced mass of the bonded atoms

The degree of freedom refers to the number of variables required to fully describe the motion of a particle. In a 3-dimensional space, an atom has three degrees of freedom, corresponding to its translational motion. For a molecule consisting of N atoms, the total degree of freedom becomes $3N$ since each atom contributes three degrees of freedom. However, due to the bonding between atoms, not all motions are translational. Some motions are rotational, and others are vibrational. In the case of non-linear molecules, the rotational motion can be described in terms of rotations around three axes, resulting in three rotational degrees of freedom. The remaining $3N-6$ degrees of freedom correspond to vibrational motion. On the other hand, linear molecules (such as CO₂) do not exhibit rotation around their own axis as it leaves the molecule unchanged. Hence, linear molecules have only two rotational degrees of freedom, leaving $3N-5$ degrees of freedom for vibration.

The IR band intensity, however, is significantly relative to the change in the dipole moment of the molecule during the vibration (selection rule). Therefore, there are IR-active and IR-inactive vibrations (see Figure 2.6 for CO₂).

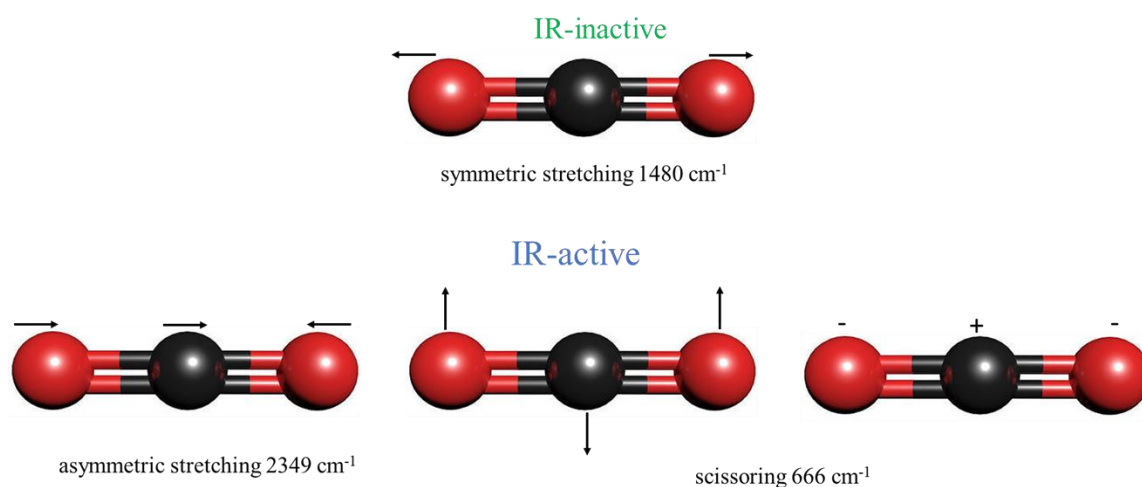


Figure 2.6. The four vibrational modes of a linear three-atomic molecule (CO₂).

The traditional FTIR technique, such as transmission IR, has certain limitations as it can only be utilized for samples that are partially transparent to infrared radiation. In cases where the sample is opaque and exhibits low infrared transmittance, an alternative approach known as Diffuse Reflectance Infrared Fourier Transform Spectroscopy (DRIFTS) can be employed.⁹⁹ In this mode, the infrared beam does not need to go through the bulk sample like in transmission mode. In the diffuse reflectance mode, the infrared beam is directed onto a shallow layer of catalyst powder, penetrating approximately 1-10 microns into it. The beam is then reflected back to an optical system. To achieve this, a configuration of mirrors is used, as shown in Figure 2.7. These mirrors are arranged to allow the incident infrared beam to be directed towards a pair of parallel elliptical mirrors. One side of the elliptical mirror directs the incident beam towards the sample, and the reflected radiation from the sample is collected by the second elliptical mirror. Finally, the collected radiation is directed towards a detector.

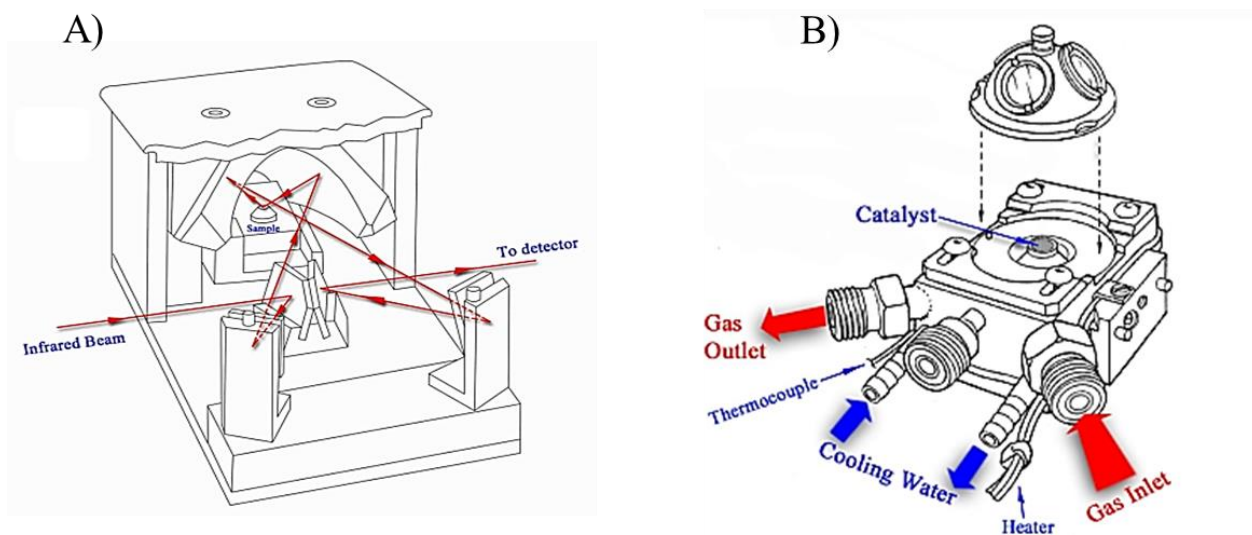


Figure 2.7. DRIFT reactor. A) Optical setup for a DRIFTS experiment (Harrick). B) Reaction Cell (Harrick) (Adopted from ref. ¹⁰⁰).

In this thesis, this powerful technique has been used to follow the state of Cu species on the surface of the support through the IR peak of $\text{Cu}^+\text{-CO}$.

Experimental description: Operando Diffuse Reflectance Infrared Fourier Transform Spectroscopy measurements were performed using a Nicolet 6700 FTIR spectrometer (Eurotherm), which was equipped with high temperature Praying Mantis reaction cell (Harrick), CaF_2 windows and a temperature control unit. The gas flow system with Bronkhorst mass flow controllers was connected to the reaction cell to enable dosages of reactants. The spectra were recorded in the frequency range $4000\text{-}400\text{ cm}^{-1}$ (averaged 64 scans). 50 mg of pure sample particles were deposited on top of a layer of 60 mg KBr. Initially, a reductive pretreatment in a stream of 10% H_2/He (15 ml min^{-1}) was performed for one h at $250\text{ }^\circ\text{C}$. Afterwards, the reaction cell temperature was reduced to $50\text{ }^\circ\text{C}$ and switched to the reaction mixture of 1% CO , 1% O_2 , and 80% H_2 (15 ml/min) in He. After one hour reaction, the temperature increased to ($80\text{ }^\circ\text{C}$, $90\text{ }^\circ\text{C}$, and $100\text{ }^\circ\text{C}$, respectively) and at relevant temperatures the reaction was kept for 60 min.

2.3.8 Electron paramagnetic resonance (EPR)

In heterogeneous catalysis, electron paramagnetic resonance has been widely used to study the nature of paramagnetic species which are containing unpaired electrons such as free organic or inorganic radicals, and some oxidation state of transition metals. As well known in literatures, copper is the leading active site for preferential oxidation of CO, and redox pair of $\text{Cu}^{2+}/\text{Cu}^+$ plays a decisive role in the catalytic performance. Cu^{2+} has unpaired electrons and, therefore, is possible to detect by EPR spectroscopic technique.

Electron paramagnetic resonance (EPR) is widely used to investigate the oxidation states (oxidized and reduced) of Cu-based catalysts. In general, more information about the nature and symmetries of Cu²⁺ ion sites can be obtained from the EPR signal of Cu²⁺. Based on anisotropy and the EPR parameters of the EPR signal, the Cu²⁺ ions can be demonstrated to be existing as monomers, dimers, and clusters in tetrahedral or octahedral symmetries.^{101, 102} Moreover, the intensity of the EPR signal from isolated Cu²⁺ can be considered as a measure of the degree of oxidation of Cu catalysts. For example, when Cu²⁺ ions are exposed to progressive reduction conditions, the EPR signals intensity of Cu²⁺ must be significantly decreased due to the reduction of Cu²⁺ ions to EPR silent species such as Cu⁺ or Cu⁰.

In this Ph.D. thesis, the EPR technique was primarily used to characterize how the copper (Cu²⁺) ions based on CeO₂ are located and to understand how the Cu²⁺ involved in the catalytic activity cycle.

The basis of EPR spectroscopy lies in the spin of an electron and its associated magnetic moment. When a single electron placed within an applied magnetic field, B₀, the two possible spin states of the electron have different energies. This energy difference is a result of the Zeeman effect (Figure 2.8). The lower energy state occurs when the electron magnetic moment, μ, is aligned parallel with the magnetic field and a higher energy state occurs where μ is aligned antiparallel the magnetic field. The two states are distinguished by the projection of the electron spin, m_s, on the direction of the magnetic field, where m_s = -1/2 is the parallel state, and m_s = +1/2 is the antiparallel state. The energy difference levels between the two spin states are given by the equation (2.15)

$$\Delta E = g_e \beta \cdot B_0 \quad 2.15$$

β is the Bohr magneton (9.274 x 10⁻²⁸ J.G⁻¹)

B₀ is the strength of the magnetic field

g_e is known as the g-factor of the free electron (≈2.0023)

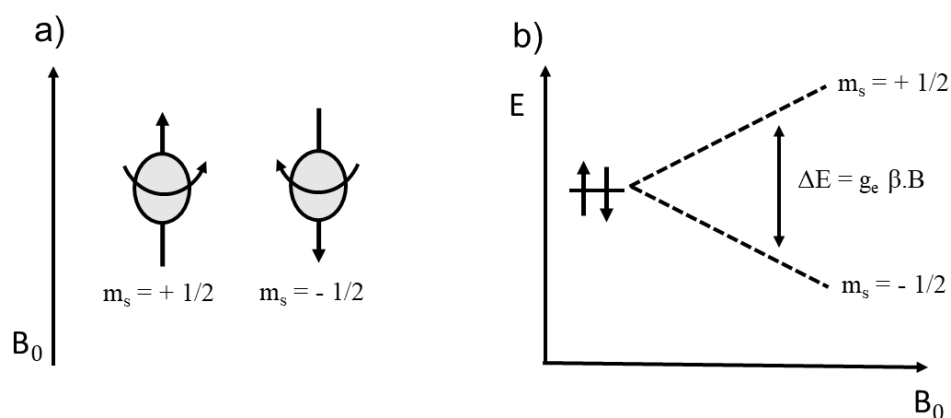


Figure 2.8. (a) The orientations of the electron μ in the magnetic field B₀, (b) corresponding the spin state energies.

In a molecule, electron occupy orbital where spin-orbit coupling can occur. This causes a deviation in the g-value from its expected value g_e and can be utilized to detect the presence of species containing a

single unpaired electron within the molecule. The g-value is calculated based on the frequency (ν) of the EPR signal in units of megahertz (MHz) and the strength of the magnetic field (B_0) (equation 2.16).

$$g = \frac{\Delta E}{\beta \cdot B_0} = \frac{h \cdot \nu}{\beta \cdot B_0} = 0.7145 \cdot \frac{\nu(\text{MHz})}{B_0(\text{gauss})} \quad 2.16$$

h is the Planck's constant ($6.626 \times 10^{-34} \text{ J s}^{-1}$)

ν is the value of the frequency (MHz)

β is the Bohr magneton ($9.274 \times 10^{-28} \text{ J G}^{-1}$)

EPR spectra can be recorded using two distinct methods. The first method is continuous wave (cw) spectroscopy, where the applied frequency remains constant. In this approach, the magnetic field is adjusted until the microwave energy matches the energy difference required for allowed spin transitions. Concurrently, peak absorption of energy occurs, and the EPR signal is measured. The resonance energy for EPR falls within the microwave range, typically around 9-10 GHz in the X-band frequency. The second method is known as pulsed EPR, where short pulses of high-power microwave radiation are directed towards the sample, and the sample's response is recorded in the absence of radiation. However, in this thesis, exclusively the continuous wave (cw) method was applied.

In the case of Cu^{2+} , the magnetic interaction between the magnetic moment of the unpaired electron and nuclear spin results in a slightly different magnetic energy for each spin state into different levels as shown in Figure 2.9 for Cu^{2+} ion ($d^9, I = 3/2$). The selection rule allows only transitions between levels with $\Delta m_S = \pm 1$ and $\Delta m_I = 0$. Therefore, four transitions will be allowed as shown in the energy level diagram. Thus, the obtained EPR spectrum comprises four-lines signal centered at g_{iso} and split by a_{iso} . For anisotropic spectrum, four-lines splitting are observed for the individual lines.

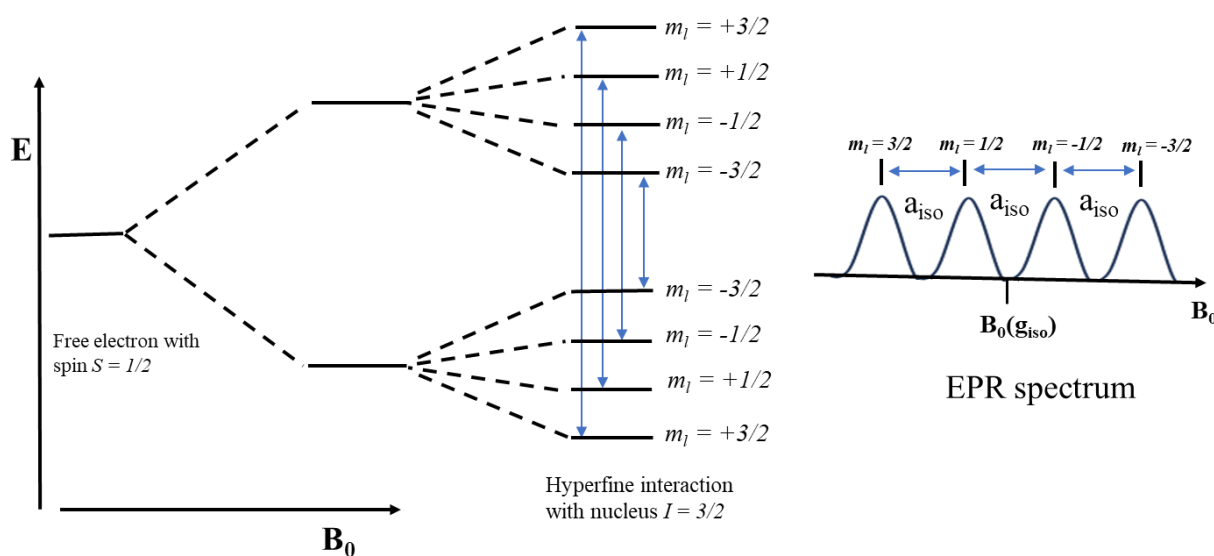


Figure 2.9. Energy level diagram and resulting EPR spectrum for a spin system with one electron $S = 1/2$ and a nucleus $I = 3/2$ with isotropic electron Zeeman (g_{iso}) and hyperfine (a_{iso}) interactions.

Experimental description: Electron paramagnetic resonance (EPR) spectra were recorded with a Bruker ELEXSYS 500 –10/12 spectrometer run at x-band cw-spectroscopy. Microwave power was used 6.3 mW, an amplitude of up to 5 G and a modulation frequency of 100 kHz. Operando EPR experiments were carried out in a home-made quartz plug-flow reactor with a 3.0 mm inner diameter and a 0.5 mm wall thickness under continuous feed flow. Typically, a 50 mg sample particle (250-350 μm) was deposited inside a quartz plug-flow reactor connected to a flow gases unit equipped with mass flow controllers (Bronkhorst) at the inlet and a quadrupole mass spectrometer (Omnistar, Pfeiffer Vacuum GmbH) at the outlet for online product analysis.

Before the catalytic reaction, the catalyst was reduced by 10% H_2/Ar for one hour at 250 $^\circ\text{C}$. Then, the following experiments were performed by exposing the reduced Cu catalysts and the bare support at 90 $^\circ\text{C}$ to: 1) PROX mixture 1% CO + 1% O_2 + 80% H_2 in He. 2) 5% O_2/He for 1h to check the ability of Cu catalysts to activate oxygen, flushing with 50 ml/min of Ar for 15 min followed by feeding 5% CO/He for 60 min to check the role of surface oxygen in CO oxidation.

2.3.9 Near ambient pressure X-ray photoelectron spectroscopy (NAP-XPS)

Near atmospheric pressure (NAP)-XPS is a technique frequently used to characterize catalysts under working conditions and to investigate the surface chemistry associated with the catalytic process at the solid-gas interface. It is a powerful surface analysis method which provides information about the oxidation state, elemental composition, and electronic properties of the surface of the materials.

NAP-XPS has been utilized to study a comprehensive set of catalytic reactions (CO oxidation, NO reduction, forward and reverse water-gas shift reaction, CO and CO_2 hydrogenation to methanol or methane, methane dry reforming, methane conversion to methanol, hydrogenation of olefins, desulfurization, etc.). In the field of heterogeneous catalysis, NAP-XPS has shown its ability to identify catalytic active phases, variations in the concentration of surface species, and associated reaction mechanisms, where reactions primarily take place at the gas-solid interface. This method provides in situ and surface-sensitive information that cannot be obtained by other "bulk" characterization techniques like X-ray diffraction. Therefore, in this work, Near Ambient Pressure X-ray photoelectron spectroscopy (NAP-XPS) was used to determine the changes in the oxidation state of Ce species on the surface of the catalyst under CO-PROX reaction conditions and in control experiments, and also to gain more information about the amount of the O-vacancy which is associated with the presence of Ce^{3+} species.

The basic principle of XPS is based on the photoelectric effect, which was first discovered by Heinrich Hertz in 1887. In XPS, the sample was illuminated by high energy photons lower than ~ 6 KeV (soft X-rays) and the kinetic energy was analysed for the emitted electrons (Figure 2.10). The emitted

photoelectron was the result of the full transfer of the X-rays energy to a core level electron. This also can be expressed mathematically in equation (2.17). It simply claims that the energy of the x-ray ($h\nu$) was equal to the binding energy (B_E) of the electron plus the kinetic energy (K_E) of the electron that was emitted, plus the spectrometer work function (Φ), a constant value.

$$h\nu = B_E + K_E + \Phi \quad 2.17$$

Equation (2.17) can be rearranged to obtain equation 2.18, in order to determine the binding energy of the electron.

$$B_E = h\nu - K_E - \Phi \quad 2.18$$

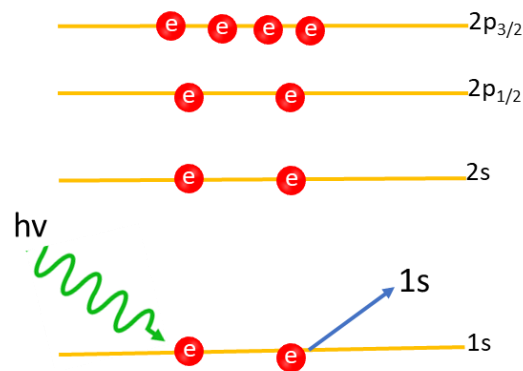


Figure 2.10. Processes that result from x-ray bombardment of a surface include emission of a photoelectron.

This concept was also illustrated diagrammatically in Figure 2.11 Note that the photoelectron binding energy was measured with respect to the sample Fermi level (not the vacuum level) which was the reason that Φ was included.

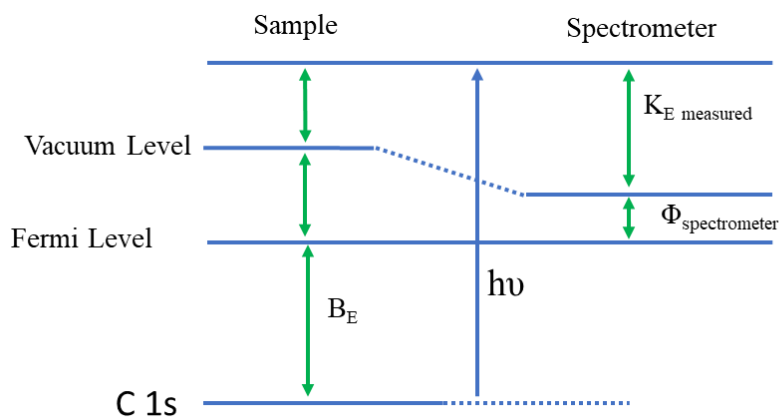


Figure 2.11. Energy level diagram illustrates schematically the basic XPS equation, including the x-ray source energy ($h\nu$), the binding energy of the electron (B_E), the measured kinetic energy of the electron ($K_{E \text{ measured}}$), and the work function of the spectrometer ($\Phi_{\text{spectrometer}}$).

One notable advantage of X-ray Photoelectron Spectroscopy (XPS) compared to other techniques is its capability to determine the chemical surroundings of the atoms present in a sample. The chemical environment encompasses factors such as the closest neighboring atoms and the oxidation state of the element, which directly influence the binding energy observed in the photoelectron peaks.

An XPS instrument consists of an X-ray source, sample stage, analyzer, extraction lenses, and detector placed in an ultra-high vacuum environment. A schematic diagram of an XPS system is demonstrated in Figure 2.12, showing all the main components. For two reasons, the XPS instruments are housed in an ultra-high vacuum. First, in order to prevent the emitted electrons from scattering off air molecules as they travel to the analyzer, and this requires vacuum levels on the order of 10^{-5} – 10^{-6} mbar. Second, to reduce the surface contamination that occurs within the chamber.

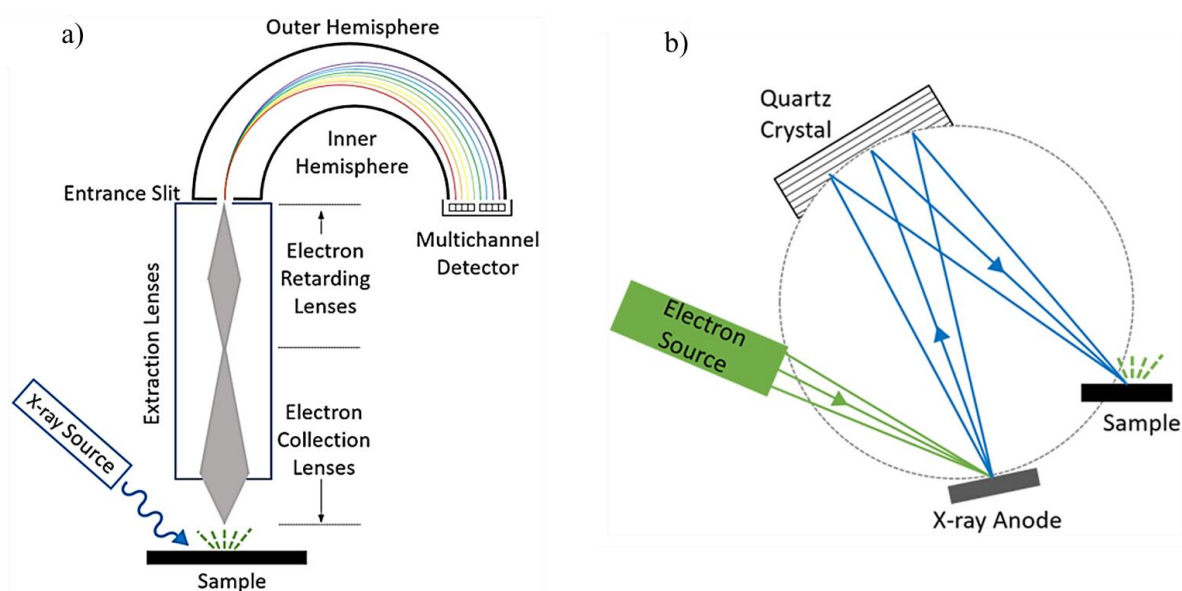


Figure 2.12. Schematic diagrams show the major components of an (a) XPS instrument and (b) monochromator (Adopted from ref. ¹⁰³)

Experimental description: Near Ambient Pressure X-ray photoelectron spectroscopy (NAP-XPS) spectra were recorded on a laboratory NAP-XPS (SPECS Surface Nano Analysis GmbH, Germany). The NAP-XPS apparatus consists of (i) differentially pumped phoibos 150 electron energy analyzers, (ii) a nozzle of 500 μm diameter, (iii) a monochromated Al K α radiation source ($E = 1486.6$ eV), and a laser system for sample heating. The feed gas mixture was introduced by using Mass flow controllers (Brooks, GF40). The total pressure in the analysis chamber was set at 2 mbar. The pressed sample was deposited in a stainless-steel holder. A thermocouple was attached to the sample's surface to control the temperature. The binding energy peaks of the sample were referenced according to the corresponding binding energy peak (284.6 eV) positions of C 1s.

3 Results and discussions

3.1 Developing of $\text{Cu}_x\text{CeTiO}_2$ ($x = 0.05$ wt%) catalyst for CO PROX reaction

The majority of prior studies on CO oxidation and CO-PROX have used Cu concentrations of at least 5 wt% or higher, which ultimately results in the formation of separate but loosely attached CuO_x nanoparticles. Recently, our group have presented highly active $\text{Cu/CeO}_2\text{-TiO}_2$ catalysts for CO oxidation with a Cu content well below 1 wt%. Their activities in terms of Cu-mass normalized rate were higher than those of Cu/CeO_2 catalysts with higher Cu loadings.⁵⁵ We have demonstrated that active sites in these catalysts are Cu single site ions exposed on the surface of CeO_2 that undergo reversible $\text{Cu}^{2+}\text{-O-Ce}^{4+} \rightleftharpoons \text{Cu}^+\text{-}\square\text{-Ce}^{3+}$ redox shuttles. Despite these very promising results, a CuCeO-TiO_2 ($\text{Ce/Ti} = 0.18$) catalyst with very low amount of Cu (0.05wt%) has prepared by sol-gel method. Firstly, CuCeO-TiO_2 ($\text{Ce/Ti} = 0.18$) catalyst has successfully applied for preferential CO oxidation (section 3.1.1). The next section focuses on structure, and surface properties of the bare support and Cu containing catalysts (3.1.2). In the following parts, various in situ/operando spectroscopic techniques such as NAP-XPS (3.1.3), EPR (3.1.4), and DRIFTS (3.1.5) are used to derive structure-reactivity relationships under most relevant reaction conditions. Last section, Conclusions are drawn in 3.1.6.

3.1.1 Catalytic performance of $\text{Cu}_{0.05}\text{CeTiO}_2$

The CO conversion over the Cu-free support was low, whereas much higher activity was observed over the supported Cu catalyst under the same reaction conditions (Figure 3.1.1d). The catalytic activity of the copper catalyst expressed as rate of CO-oxidation is shown in Figure 3.1.1a. An almost the rate of CO oxidation (based on Cu mas) increase linear was observed with increased temperature and 100% CO_2 selectivity even when temperature reached 100 °C. Only at high temperature, the H_2 oxidize was observed and this led to form water at the expense of CO_2 . López et al. have used Eq. 2.4 to rank the intrinsic catalytic performance of more than 40 $\text{CuO}_x\text{-CeO}_2$ catalysts from previous studies.⁹¹ To compare, the K_L values of this catalyst and their best catalyst A (prepared by a citrate method with 10 wt% Cu)¹⁰⁴ are plotted in Figure 3.1.1.b. It is evident that our catalysts clearly outperforms catalyst A.⁹¹ and all other Cu-based cerium oxide catalyst used for CO-PROX catalysts in this ranking of 2008 (not shown in Figure 3.1.1b), since it displays higher intrinsic activity at much lower Cu loadings. Note that our catalyst contains 0.05 wt% Cu compared to 10 wt% of catalyst A. Moreover, This catalyst shows higher intrinsic CO-PROX activity than those reported.^{57, 86, 105, 106} However, it showed very stable performance and almost did not deactivate within 17 h time of stream at 120 °C (Figure 3.1.1c), although slight H_2 oxidation at this temperature resulted to form some water, competitive adsorption of which is

known to cause deactivation of CuO_xCeO_2 catalysts.¹⁰⁷⁻¹⁰⁹ To see the reasons for this unprecedented activity, we should consider the results of structure characterization presented in the following sections.

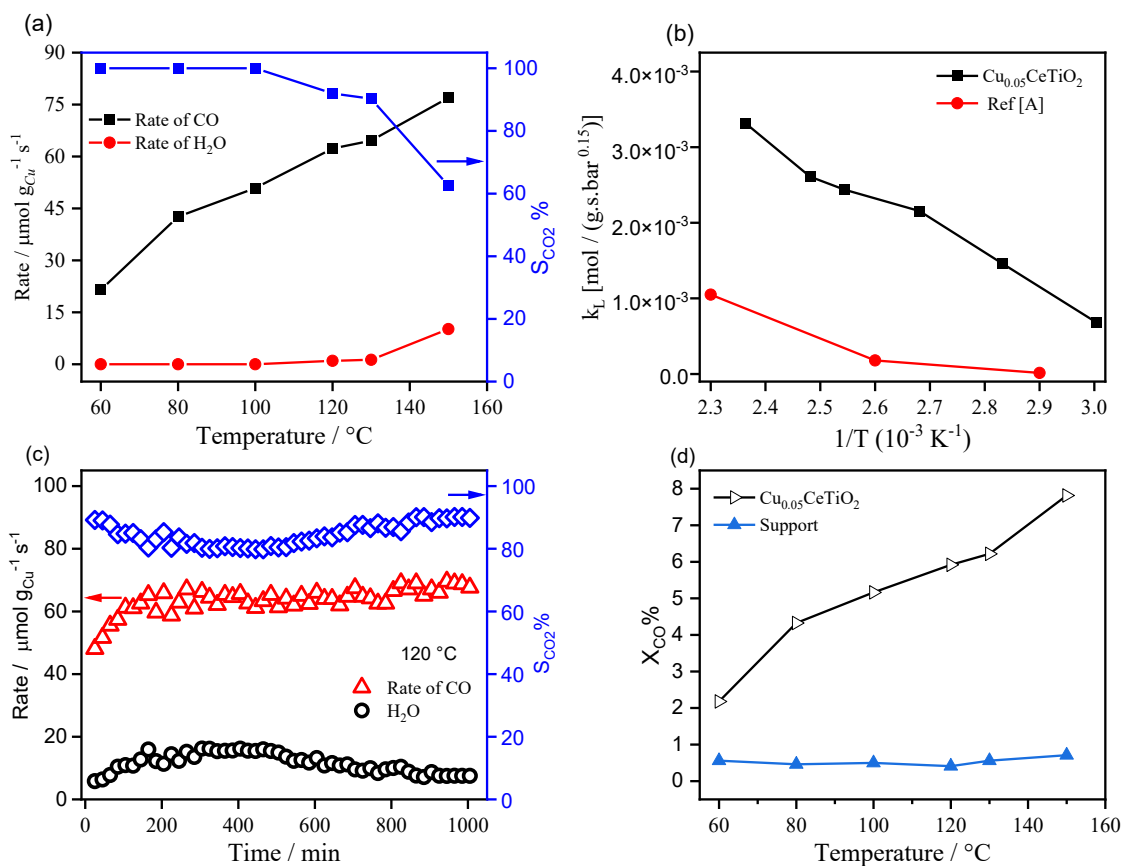


Figure 3.1.1. (a) Cu mass normalized rate of CO conversion and H₂O formation (left axis) and CO₂ formation selectivity (right axis), b) intrinsic catalytic activity constants k_L for the Cu catalyst of this work in comparison to the best catalyst (A) of ref,¹⁰⁴ (c) Long-term stability test at 120 °C under CO-PROX conditions, (d) CO conversion during CO-PROX reaction (1% CO, 1% O₂, 80% H₂; 30 ml min⁻¹) on the Cu catalyst and support obtained after H250 treatment over the temperature range from 60 to 150 °C.

3.1.2 Catalyst characterization

Elemental analysis by ICP-OES established a Ce/Ti ratio of about 0.2 for the pure support and the Cu-containing catalyst as well as a Cu loading of 0.05 wt% for the latter, which are close to the values used in the synthesis solution. Both the pure support and the Cu catalysts are showed type IV N₂ adsorption/desorption isotherm with hysteresis loops typical for mesopores (Figure 3.1. 2).¹¹⁰ The BET surface area slightly decreased upon addition of Cu whereas the average pore diameters increased, and the total pore volume was not changed much.

Table 3.1.1. Elemental composition, surface and pore properties.

Sample	Element composition		S_{BET} ($\text{m}^2 \cdot \text{g}^{-1}$)	Pore volume ($\text{cm}^3 \cdot \text{g}^{-1}$)	Average pore diameter (nm)
	Cu	Molar ratio			
	(wt. %)	Ce/Ti			
CeTiO ₂	-	0.19	143	0.32	6.4
Cu _{0.05} CeTiO ₂	0.05	0.18	111	0.27	7.3

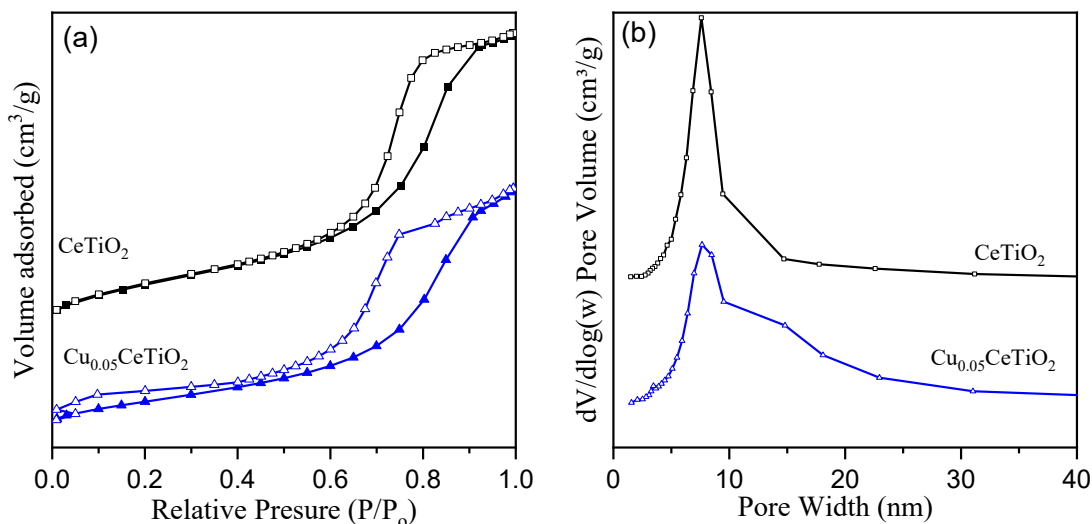


Figure 3.1. 2. (a) N₂ adsorption and desorption isotherms (filled and open symbols, respectively) and (b) pore size distribution calculated from the desorption branch of support and Cu-catalyst.

Figure 3.1.3 depicts that the XRD powder patterns of the pure support and the Cu catalyst are nearly identical. Both, support and catalyst show characteristic peaks of the CeO₂ cubic fluorite structure (ICDD PDF 00-034-0394) and anatase phase of TiO₂ (ICDD PDF-2 2017).¹¹¹ This indicates that the crystalline phase does not change even when is Cu added. Due to very copper loading, there are no reflection peaks corresponding to Cu oxide (CuO).

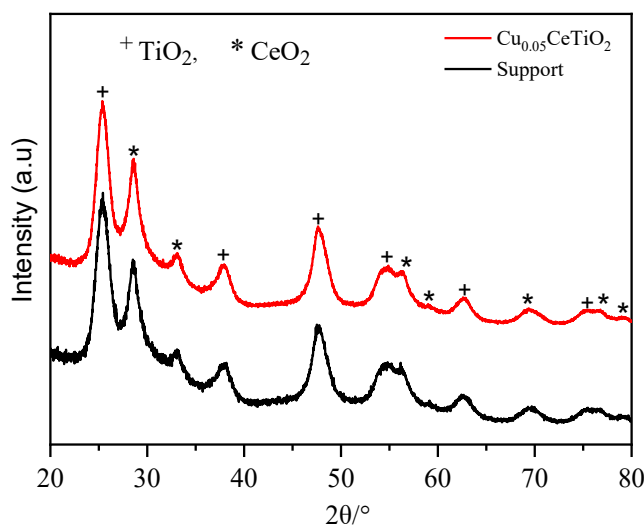


Figure 3.1.3. Powder XRD patterns of the fresh CeO₂-TiO₂ support and the Cu catalyst.

Figure 3.1. 4 shows Raman spectra of both the support and the Cu catalyst. They are also virtually identical and in agreement with the XRD patterns. The typical bands of anatase appear at 148, 403, 517, and 640 cm^{-1} . Besides, a weak band attributed to the F_{2g} is seen at 463 cm^{-1} vibration mode of the cubic fluorite-type structure of CeO_2 .^{111, 112} As expected, no Raman bands related to the vibration of Cu-O could be detected and this a good evidence that the Cu species are highly dispersed.

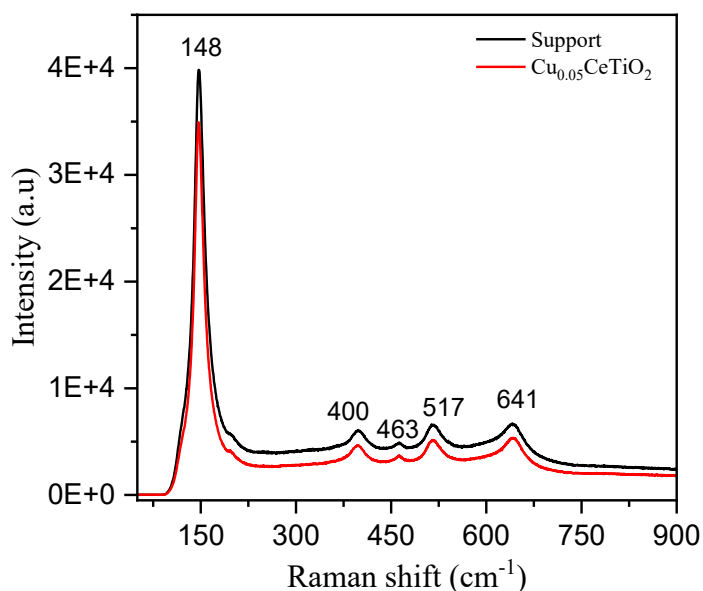


Figure 3.1. 4. Raman spectra of the fresh $\text{CeO}_2\text{-TiO}_2$ support and Cu-containing.

STEM-HAADF images also with corresponding energy-dispersive X-ray spectroscopy (EDS) maps of the pure support and the Cu catalyst to visualize the distribution of Ti (red) and Ce (green) are displayed in Figure 3.1.5. ED spectra of the catalyst area are plotted in Figure A.1. The Ti and Ce are homogeneously distributed throughout the whole sample in the Cu-free support, indicating a fairly uniform distribution of CeO_x on TiO_2 (Figure 3.1.5b). In addition, the Cu catalyst (Figure 3.1.5d) shows regions of enriched TiO_2 and almost pure CeO_2 (marked with a circle in Figure 3.1.5d) as well as areas with uniform distribution of Ce and Ti. No Cu species can be seen in the HAADF STEM images (Figure 3.1.5c and e), possibly due to the very low Cu content. Moreover, the contrast in the HAADF STEM images is dominated by heavy, strongly scattering Ce atoms, which makes it difficult to see tiny Cu species in their vicinity. Likewise, distinguishing between Cu and Ti is difficult because they have similar or close atomic numbers (i.e., low Z-contrast). Also, Cu could not be found by EDS mapping (Figure 3.1.5d), which indicates that it is present as a highly dispersed single atoms or in very few large separate entities not comprised by mapping. Interestingly, the presence of isolated Cu single sites is shown below by EPR and DRIFT spectroscopy results. The electron energy loss spectra (EEL) at the Ce M-edge from different positions marked as 1 and 2 in the ADF image (Figure 3.1.5e) are shown in (Figure 3.1.5f), they provide information on the Ce oxidation state. Area 1 is located on a large particle

consisting of pure CeO₂ (similar to the green entity in (Figure 3.1.5d), while in region 2 Ti and Ce are relatively homogeneously dispersed as in the Cu-free support (Figure 3.1.5d).¹¹³ The Ce white lines appear at energy losses characteristic of Ce⁴⁺ in the EEL spectrum of area 1 (black trace in Figure 3.1.5f). In contrast, the corresponding signals of area 2 are slightly shifted to lower loss energies. This observation indicates that big separate CeO₂ particles in the Cu catalysts contain Ce basically in its highest valance state +4 while Ce evidently reduced to +3 when it is highly dispersed on TiO₂.¹¹³

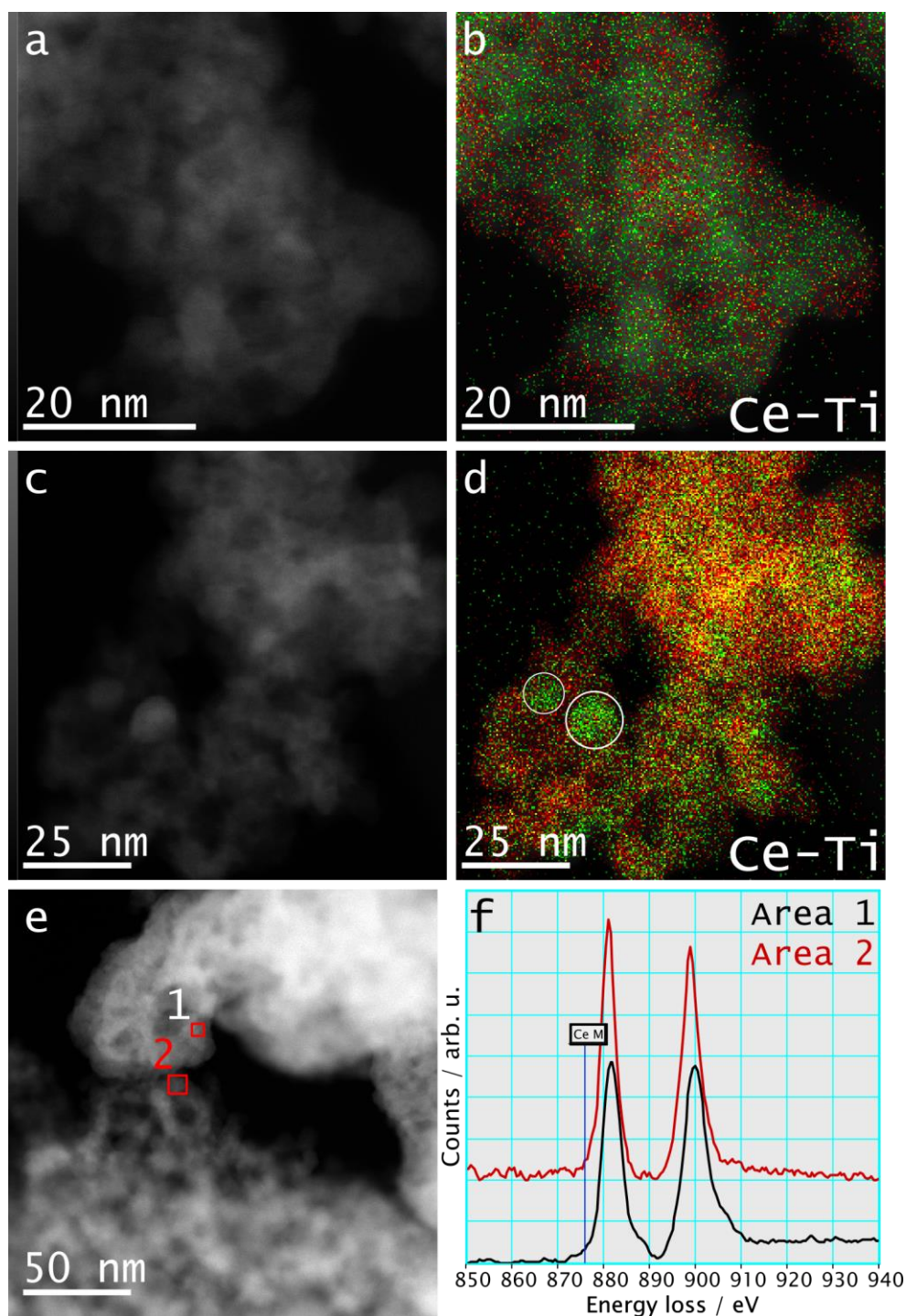


Figure 3.1.5. HAADF-STEM images (a, c), ADF image (e), EDS maps of Ti (red) and Ce (green) (b, d) and EEL spectra (f) of the Cu-free support (a, b) and the Cu catalyst (c-f).

3.1.3 Operando NAP-XPS investigation.

All spectra of the bare support and the copper catalyst in the region of Ce 3d show the characteristic doublet of Ce^{+4} at 916.86/898.59 eV (u'''/v'''), 901.09/882.7 eV (u/v) and 907.67/887.29 eV (u''/v'') in addition to those of Ce^{3+} at 903.65/885.05 eV (u'/v') and 899.75/880.87 eV (u^0/v^0) (Figure 3.1.6).^{114, 115} The amount of Ce^{3+} on the surface has been determined from the area of the signal sub-components defined by Eq. 3.1.1¹¹⁴ and is written on the left side of the spectra.

$$Ce^{3+}(\%) = \frac{u_0+v_0+u'+v'}{\sum_i u^i+v^i} \quad (3.1.1)$$

At 127 °C in N_2 the surface of the pure support is already partially reduced and exposes 34% Ce^{3+} (Figure 3.1.6), in agreement with previous works of literature.¹¹⁶⁻¹¹⁸ Also, this is evidenced by EPR spectroscopy discussed below. Reductive pretreatment in 10% H_2/N_2 at 250 °C of the support led to a slight increase of surface Ce^{3+} to 39%. Upon subsequent switching to the complete CO-PROX feed at 120 °C no reoxidation of Ce^{3+} was observed and on CO_2 formation could be detected by mass spectroscopy. In contrast to bare support, the surface of the fresh Cu-containing catalyst (Figure 3.1.6b) in N_2 at 127 °C has only 21% of Ce^{3+} but this amount markedly increased to 32% after reduction at 250 °C. Upon turning on the CO-PROX mixture at 120 °C, most of the Ce^{3+} formed during prereduction in H_2/N_2 was re-oxidized to Ce^{4+} and formation of CO_2 and H_2O was observed (see Figure A.2)

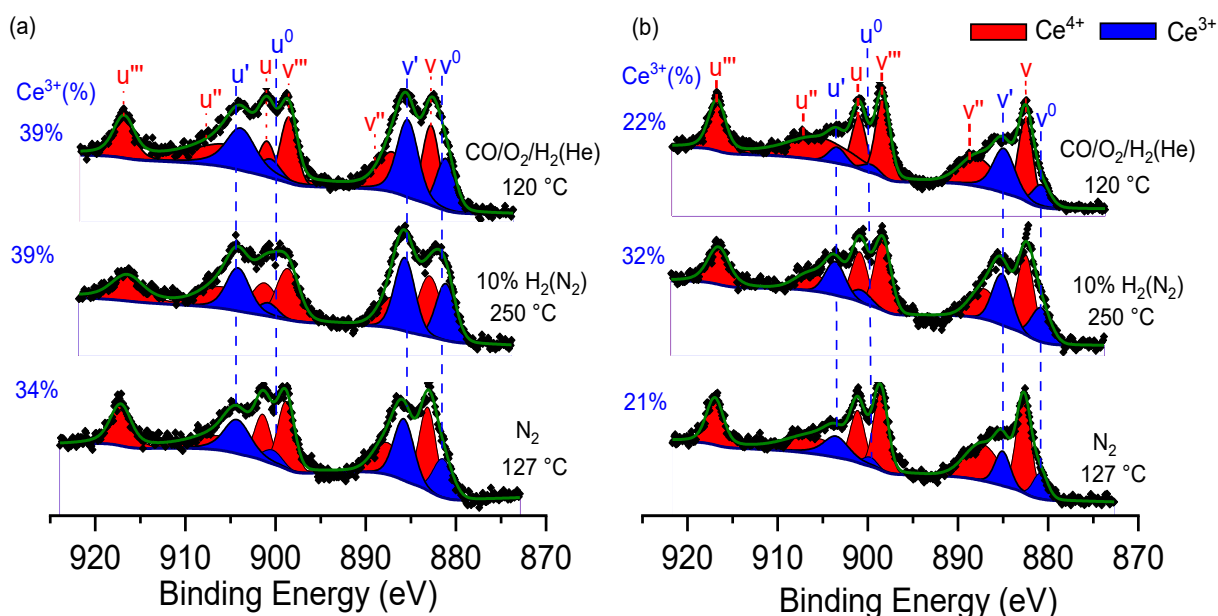


Figure 3.1.6. NAP-XPS spectra in the Ce 3d region of the support (a) and the Cu catalyst (b) measured under different conditions at a total pressure of 2 mbar.

Remarkably, The Ti valance state was unchanged and remained essentially Ti^{4+} on the surface of both, the pure support, and the Cu catalyst under all conditions (Figure 3.1.7). This indicates that the unique

$\text{Ce}^{3+}/\text{Ce}^{4+}$ redox activity on the surface of the catalyst might be due to the presence of copper, which however is hardly detectable by NAP-XPS due to its very low content of only 0.05 wt%. Therefore, to obtain more information about the impact of Cu on the redox behaviour of the catalyst, we have used operando EPR spectroscopy which is a very sensitive and more powerful method to detect Cu single atoms.

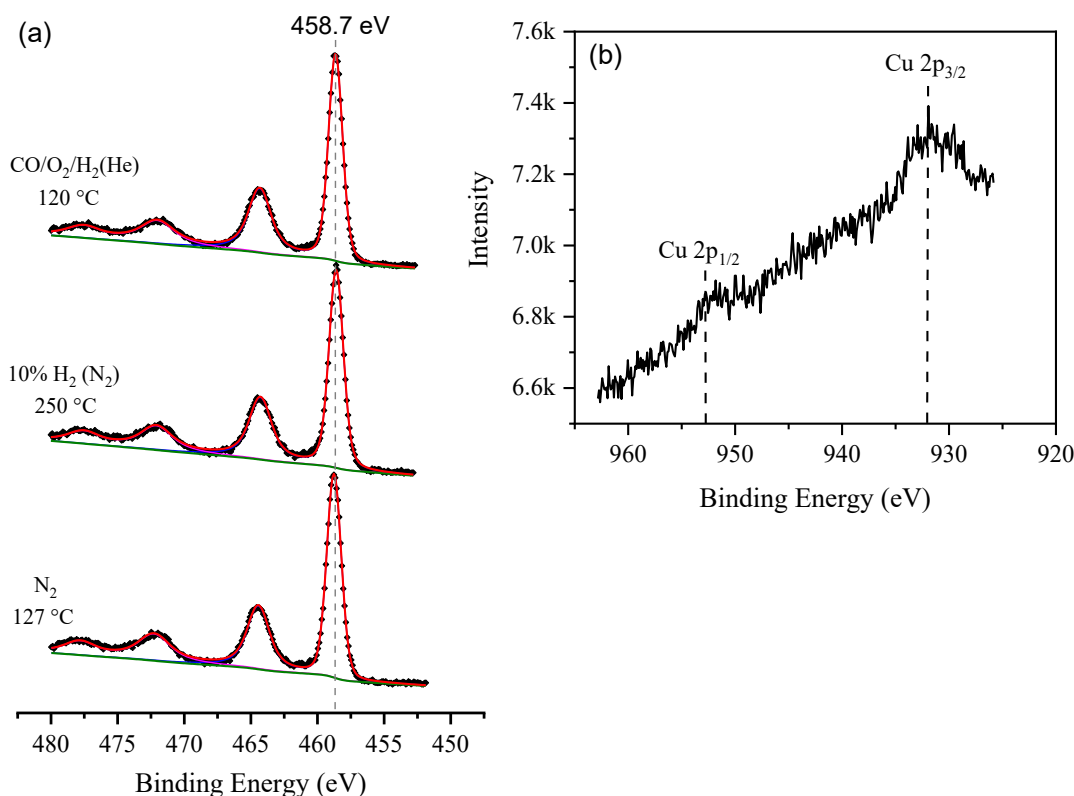


Figure 3.1.7. In situ NAP-XP spectra of the Ti2p region of the Cu catalyst measured at 120 °C under 1% CO, 1% O₂, 80% H₂ flow at a total pressure of 2 mbar (a) and spectrum of the Cu2p region of the Cu catalyst under He conditions at 90 °C temperature (b).

3.1.4 Ex Situ and Operando EPR studies.

The EPR spectrum of the pure support displays a weak isotropic line at $g = 2.004$ from electrons trapped in oxygen vacancies¹¹⁹, and another weak axial signal with $g_{\perp} = 1.967$ and $g_{\parallel} = 1.943$ (poorly resolved), that was also detected before in pure ceria as well as in CeO₂-TiO₂ materials. It is attributed to electrons trapped in vacancies next to cerium ions, to Ce³⁺ or to some kind of Ce³⁺-O⁻-Ce⁴⁺ defect sites (Figure 3.1.8a).¹²⁰⁻¹²² It suggests the presences of Ce³⁺ in both support and Cu catalyst which is also evident from the XPS and EELS data as discussed above. In addition to these signals, the bare support shows a strong roughly isotropic line at $g = 2.020$ from O₂^{•-} species which is formed by electrons transferred from anionic vacancies to adsorbed O₂ molecules. The EPR spectrum of the Cu-containing catalyst shows two signals of isolated Cu²⁺ single sites with hyperfine structure (his) due to the coupling of the single electron spin (d^9 , $S = 1/2$) with copper's nuclear spin ($I = 3/2$). The g and A values were determined

by spectra simulation (Figure A.3a). Tetragonally distorted octahedral Cu^{2+} species are detected by the signal I with $g_{\parallel} = 2.425$, $g_{\perp} = 2.075$, $A_{\parallel} = 266$ MHz and $A_{\perp} = 80$ MHz in the bulk of the $\text{CeO}_2\text{-TiO}_2$ support.¹²³ Signal II is characterized by a higher A_{\parallel} ($g_{\parallel} = 2.300$, $g_{\perp} = 2.058$, $A_{\parallel} = 290$ MHz, $A_{\perp} = 65$ MHz) and a lower g_{\perp} value. Both values indicate a higher tetragonal distortion of the Cu^{2+} environment and are perhaps consistent with a Cu^{2+} site in square-pyramidal geometry exposed on the catalyst surface.^{123, 124}

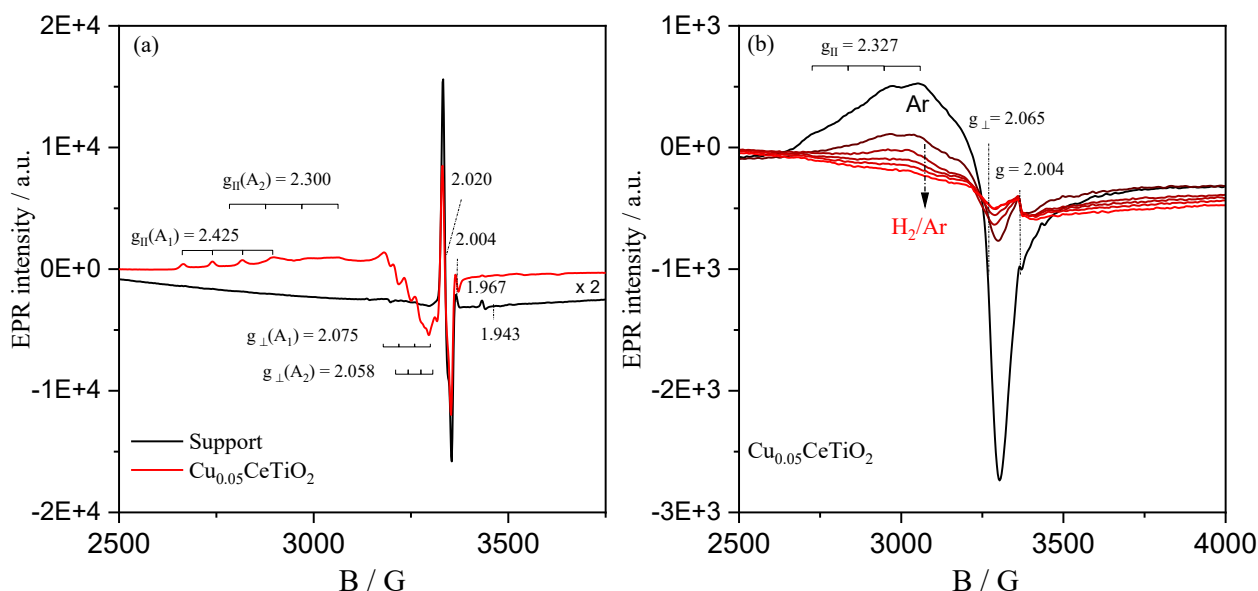


Figure 3.1.8. (a) EPR spectra of the fresh calcined support (black) and the Cu-containing catalyst (red) recorded at -180 °C; (b) of the Cu catalyst during 1 h pretreatment in 10% H_2/Ar flow at 250 °C.

When the catalyst was heated up to 250 °C under argon flow, the EPR signals of Cu^{2+} collapsed into a broad asymmetric line with $g_{\parallel} = 2.327$ and $g_{\perp} = 2.063$ in which only A_{\parallel} is poorly resolved (Figure 3.1.8b). The reason for the loss of resolution is increase of Cu^{2+} site mobility and loss of coordinated H_2O , that changes their local environment and hence, also the spin Hamiltonian parameters.^{125, 126} The Cu^{2+} single sites on the surface were reduced to EPR silent Cu^+ , upon switching to hydrogen at 250 °C, and this decreased in the EPR signal intensity of Cu^{2+} while that the oxygen vacancies seem to be slightly increased at $g = 2.004$ (Figure 3.1.8b). After 1 h reduction pretreatment, only about 53% of Cu^{2+} single species were reduced to Cu^+ whereas the rest remained Cu^{2+} (calculated from the double integrals of the EPR signals before and after exposure to H_2/Ar flow). The Cu^{2+} sites persisting reduction are likely incorporated in the bulk of the catalyst, and thus protected from contact with the reactants. A similar behaviour of Cu^{2+} species has been observed in our previous CuCeTiO_2 catalysts⁵⁵ and other CuCeO_2 materials.¹²³

When the reduced Cu catalyst was subsequently exposed to PROX feed mixture of 1% CO , 1% O_2 , in 80% H_2/Ar , the EPR signal intensity of Cu^{2+} ($g_{\parallel} = 2.329$, $g_{\perp} = 2.065$) significantly increased due to the reoxidation of reduced Cu species with time (Figure 3.1.9a). This reoxidation process was very fast and comprised the majority of Cu sites already within the first 10 min (Figure 3.1.9b). However, only about

90% of the initial Cu^{2+} intensity was reached at steady state under PROX reaction conditions. This suggests that the reoxidation of Cu^+ to Cu^{2+} by O_2 molecules is slower than the reduction of Cu^{2+} active EPR-silent Cu^+ species by CO, making the total EPR-active Cu^{2+} quantity in time average under steady-state reaction conditions slightly lower than in the freshly Cu-based CeTiO_2 catalyst.⁵⁵ The Cu^{2+} ionic radius is slightly lower than that of Ce^{4+} (0.77 pm and 0.87 pm in 6-fold coordination, respectively), but higher than that of Ti^{4+} (0.61 pm).¹²⁷ This might favour the incorporating of Cu in Ce^{4+} instead of Ti^{4+} lattice positions, and the smaller particle size of CeO_2 in Cu-containing catalyst may increase the percentage of accessible Cu single site on the surface of CeO_2 . The online mass spectrometry data in Figure A.3b also indicated the production of CO_2 during the PROX conditions at the outlet of the EPR flow reactor.

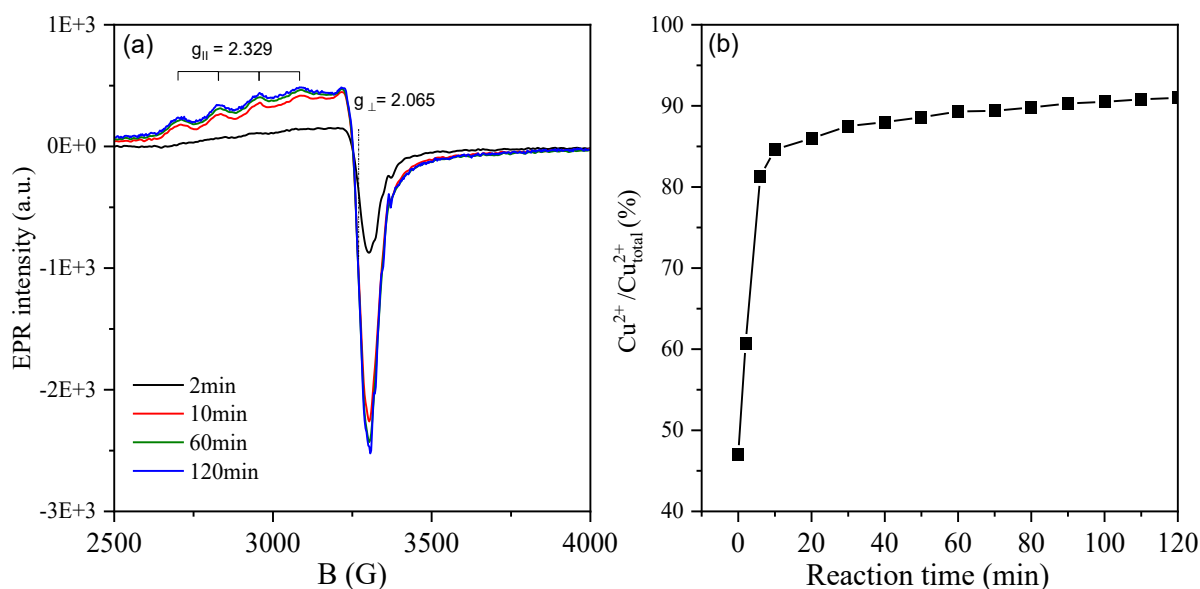


Figure 3.1.9. (a) Operando EPR spectra at 120°C of the Cu catalyst (pre-reduced for 1 h in H_2 at 250 °C) during exposure to PROX feed flow of 1% CO + 1% O_2 + 80% H_2 (spectrum after 1 h pretreatment in H_2 at 250 °C and cooling to 120 °C subtracted), (b) intensity ratio of the Cu^{2+} EPR signal in plot (a) to the one in the initial calcined catalyst (based on double integrals).

3.1.5 Operando DRIFT investigation

DRIFT spectra of the Cu-free O₂ support and the copper catalyst (both after reductive pretreatment in 10% H_2/He at 250 °C for 1h) recorded at 80 °C under PROX feed mixture are displayed in Figure 3.1.10. The pure support shows the two broad weak bands at 2127 and 2160 cm^{-1} attributed to the modes of gaseous $\text{CO}_{(\text{g})}$ and decreased significantly within the first 10 min (Figure 3.1.10b).¹²⁸

Figure 3.1.10a shows the two characteristic bands of gaseous CO_2 gas phase at 2362 and 2339 cm^{-1} in spectra of Cu catalyst, which can be seen after introducing the CO-PROX feed, suggesting that the catalyst was working. In contrast, these bands do not appear in the spectra of the pure support, on the other hand, no catalytic activity was observed in the temperature range of 60-150 °C (Figure 3.1.1d). A

strong band of adsorbed could be seen at 2125 cm^{-1} right after switching to the CO-PROX feed mixture. This refers to the fact that the CO is much stronger adsorbed on Cu species than on Ce^{3+} sites. The Cu species on the surface should have an oxidation state lower than +2 since the catalyst was pre-reduced at $250\text{ }^\circ\text{C}$ prior to exposure to the PROX conditions. This agrees with the TPR results of our previous work over the CuCeTiO_2 catalyst⁵⁵ and also with NAP-XPS result discussed above. We ascribe the band at 2125 cm^{-1} to CO adsorbed on interfacial Cu^+ species.¹²⁹⁻¹³² The band intensity of Cu^+ -CO continuously decreases during reaction time. This suggests the reoxidation of reduced copper species to Cu^{2+} , and this agrees well with EPR results (Figure 3.1.9.a).

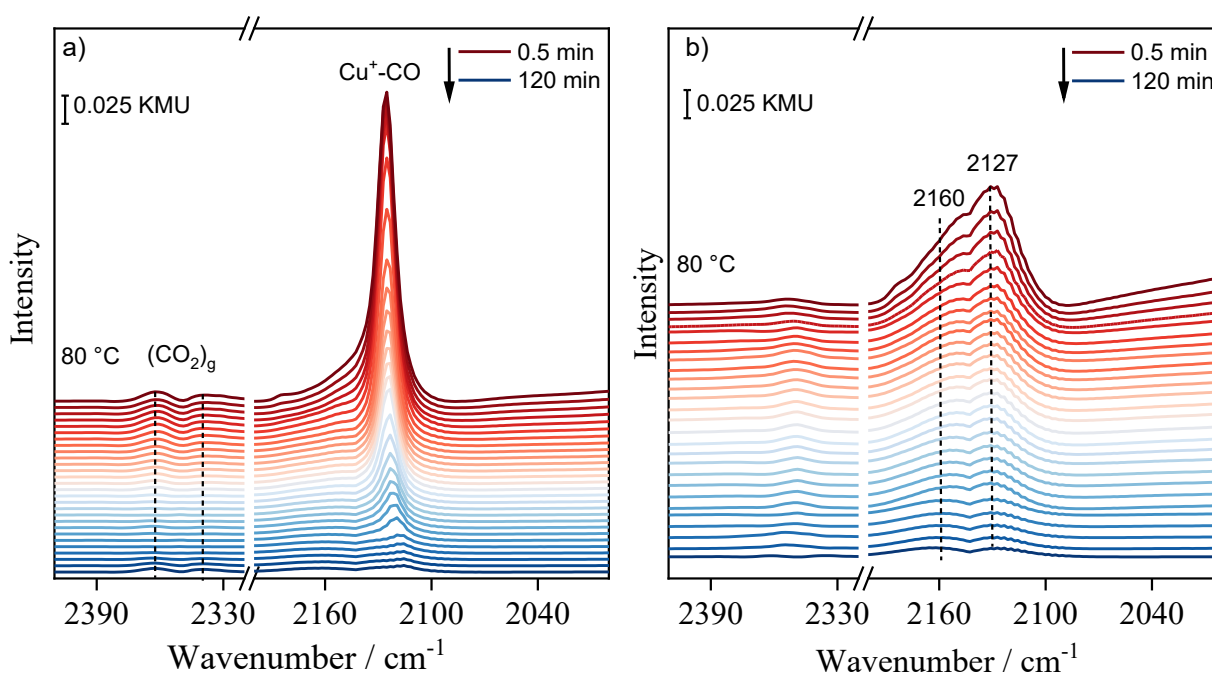


Figure 3.1.10. DRIFT spectra recorded as a function of time at $80\text{ }^\circ\text{C}$ in a flow of 1% O_2 , 1% CO , 80% H_2/He of a) the Cu catalyst and b) the bare support (both pre-reduced for 1h at $250\text{ }^\circ\text{C}$ in H_2). From top to bottom: 30 s to 120 min.

3.1.6 Conclusions

Comparison with the state of literature reveals that catalyst 0.05wt% $\text{Cu}/\text{CeO}_2\text{-TiO}_2$ ($\text{Ce}/\text{Ti} = 0.18$) prepared by a sol-gel method outperformed the best known CeO_2 - based PROX catalysts significantly. The support CeTiO_2 consists of separate TiO_2 anatase and CeO_2 cubic fluorite structure that are finely mixed and homogeneously distributed throughout the pure support. Under PROX reaction conditions, NAP-XPS results confirmed that Ti^{4+} coexists with Ce^{4+} and Ce^{3+} on the surface of this support, whereas neither Ti nor Ce displayed any significant redox activity. This may be the reasons why the Cu-free support does not show catalytic activity. In contrast to the support, the Cu catalyst shows a significant and reversible $\text{Ce}^{4+}/\text{Ce}^{3+}$ redox shuttle under PROX reaction conditions whereas the Ti oxidation state essentially remains (Ti^{4+}) tetravalent.

Copper was detected only by EPR due to its tiny quantity, which confirms its predominant single-site nature. Around 50% of these Cu single sites undergo reversible redox cycle under PROX conditions and this percentage is much higher than detected in our previous 0.06% (Ce/Ti = 0.32) catalyst, which exposed only about 3% redox reversible Cu sites during CO oxidation conditions⁵⁵ and had very large CeO₂ particles in the micrometer range. Clearly the high amount of TiO₂ (Ce/Ti = 0.18) in this catalyst lead to promote the dispersion of CeO₂ particles.^{133, 134}

It seems that the extent of redox reversibility of Ce and Cu under CO-PROX conditions is similar, indicating that the Cu is located close to Ce, possibly on the surface of highly dispersed CeO₂ particles. Therefore, we suggest that the active sites for CO oxidation reported on our previous catalyst 0.06% Cu/CeTiO₂ (Ce/Ti = 0.32) are same as for PROX on the 0.05% Cu/CeTiO₂ (Ce/Ti = 0.18) catalyst, namely single Cu ions within redox-active Cu²⁺-O-Ce⁴⁺ ⇌ Cu⁺-□-Ce³⁺ moieties associated by labile oxygen on the surface of CeO₂ particles, yet due to the lower Ce/Ti ratio and much smaller CeO₂ particles lead to an increase the concentration Cu²⁺-O-Ce⁴⁺ ⇌ Cu⁺-□-Ce³⁺ moieties.

3.2 Effect of preparation method and Cu loadings on the PROX catalytic activity of Cu_xCeO_2 ($x = 0.25, 0.5$ and 1 wt%) catalysts

The spectroscopic investigations over Cu/CeTiO_2 (with very low copper content only 0.05 wt%) in previous section (3.1) showed that active sites are single Cu ions on the surface of highly dispersed Ceria, shuttling between $\text{Cu}^{2+}-\text{O}-\text{Ce}^{4+}$ and $\text{Cu}^+-\square-\text{Ce}^{3+}$. Surprisingly, we found that TiO_2 did not play any direct role during the catalytic reaction. Instead, its role is attributed to promote the formation of highly dispersed and easily reducible ceria sites with a high number of oxygen vacancies.³ Moreover, we found that a major part of Cu single sites is incorporated in the bulk during the preparation of the $\text{Cu/CeO}_2\text{-TiO}_2$ by sol-gel method and hence plays no direct role in CO oxidation, i.e., decreased the atomic efficiency of Cu. Therefore, this section aims to increase the atomic efficiency of Cu species on the surface of the support by depositing different Cu contents on highly reducible and commercial CeO_2 (without TiO_2). Moreover, to avoid the high cost, complexity, and chemical risks by applying our previously used sol-gel, a ball milling method was used to prepare different Cu/CeO_2 catalysts by solid-state reaction. Different Cu loadings, namely, 0.25, 0.5, and 1 wt%, have used to investigate how the state of Cu agglomeration effect the catalytic activity and selectivity of the PROX reaction. These catalysts have tested for preferential carbon monoxide oxidation and characterized by conventional analytic methods (sections, 3.2.1 and 3.2.2, respectively). To illustrate the interrelationship between physicochemical properties and redox behaviour of the Cu/CeO_2 catalysts and their catalytic performance, Hydrogen temperature-programmed reduction ($\text{H}_2\text{-TPR}$, section 3.2.3) and in situ and operando FTIR spectroscopy in diffuse reflectance mode (DRIFTS, section 3.2.4), Electron Paramagnetic Resonance (EPR, section 3.2.5), near ambient pressure X-ray photoelectron spectroscopy (NAP-XPS, section 3.2.6) have been applied.

3.2.1 Catalytic performance of Cu_x ($x = 0.25, 0.5$ and 1 wt%) CeO_2 catalysts

The PROX catalytic activity test over the pure support and Cu catalyst was performed in the temperature range 50-150 °C after reducing the samples with 10% H_2/He . As shown in Figure 3.2.1.c, the catalytic test of the pure support was inactive while the CeO_2 supported Cu catalysts showed much higher activity. This indicates that the synergy between Cu and Ce at the copper catalysts plays an essential role for the enhanced catalytic performance of the combined catalyst as reported.^{77, 135, 136} To obtain more information about this significant interaction and catalytic activity over Cu containing catalysts, we will consider the structural characterization results studied in detail in this section. Figure 3.2.1a displays the intrinsic activity over the prepared catalyst under PROX reaction conditions. A linear increase in CO-oxidation rate was observed with increasing temperatures, and Figure 3.2.1b shows CO_2 -selectivity

which was $\leq 100\%$ up to 100°C for all catalysts. Further increase in the reaction temperature led to a decline of the CO_2 -selectivity. The decrease of the CO_2 -selectivity could be attributed to formation of water caused by undesirable H_2 oxidation. It can be seen that CO-oxidation rate normalized on Cu decreased with increasing Cu content and it is clear from Figure 3.2.1a, that catalyst with lowest Cu loading ($\text{Cu}_{0.25}\text{CeO}_2$) is much more active than other catalysts in this section. However, comparing the reaction rate obtained by the best catalyst with lowest Cu loading ($\text{Cu}_{0.25}\text{CeO}_2$) in this work with those reported in the state of the art confirms that our catalyst exhibits activity higher than the best active catalyst reported (Table A.1) and nine times higher than the catalyst ($\text{Cu}_{0.05}\text{CeTiO}_2$) which was prepared by the sol-gel method as shown in the previous section 3. In addition to this superior activity, our catalysts were also prepared by a simple method (ball-milling), while complex and expensive preparative method was always used in literature (sol gel, hydrothermal and Co-precipitation... etc.). For the potential industrial application, the catalytic stability of the catalyst under actual reaction conditions is very important. The long-term stability tests of the Cu catalyst have been performed under the same PROX reaction conditions which were used in the kinetic measurements. Figure 3.2.1.d shows that no deactivation could be observed on all the prepared catalysts after around 75 h reaction 90°C . On the other hand, the CO_2 -selectivity remains stable during the time-on-stream experiment (98-100%). To find out what reasons are attributed to the higher catalytic performance, we must consider the results of the structural characterization presented in the following sections.

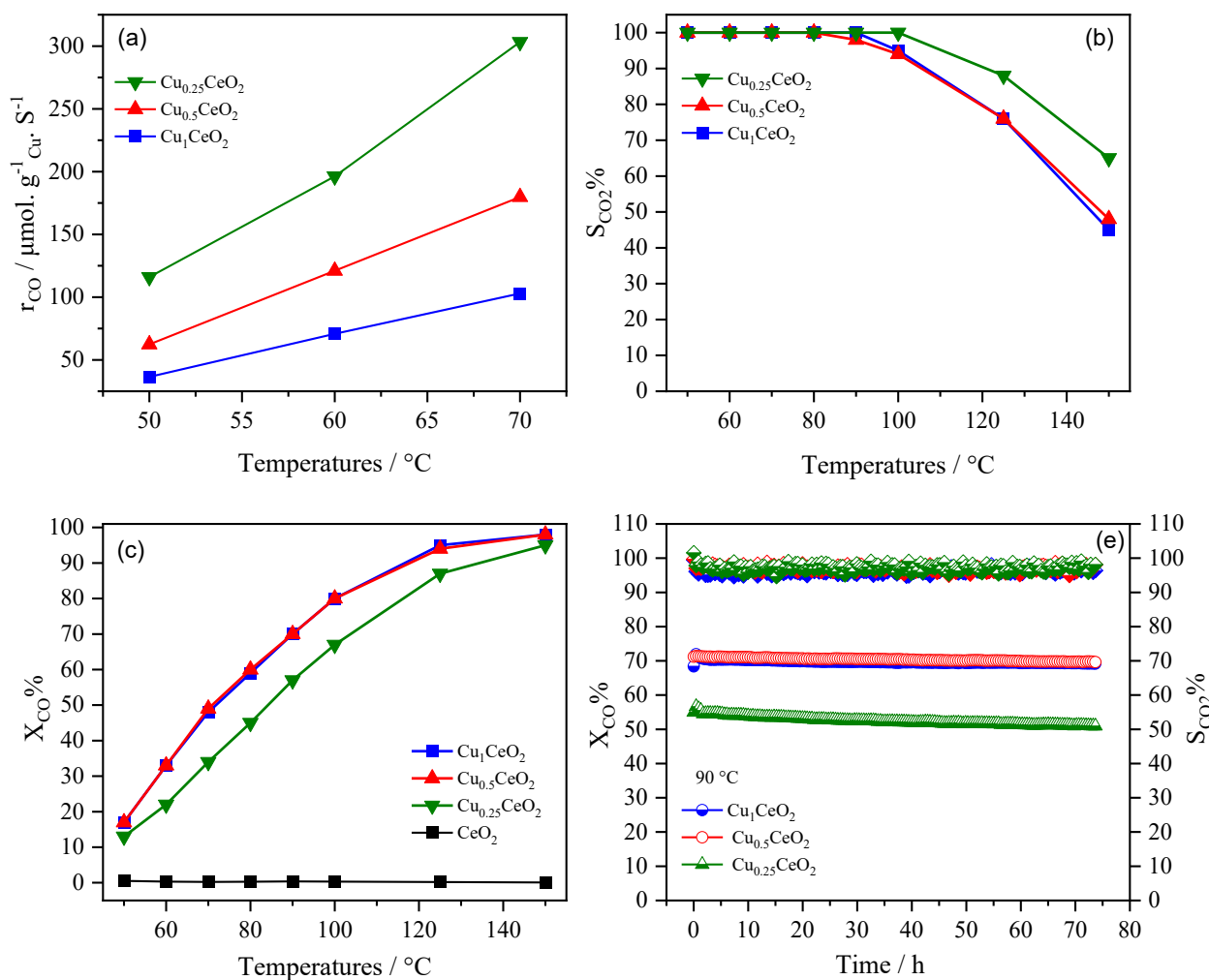


Figure 3.2.1. (a) CO oxidation rate normalized on the Cu mass, (b) CO₂-selectivity, CO₂-conversion (c) and (d). Long-term test of CO PROX over all prepared catalysts.

3.2.2 Catalyst characterization

Table 3.2.1 demonstrates the Cu content of the catalysts as determined by ICP. The content of Cu in all catalysts was close to the nominal values. The texture properties of the support and Cu catalysts are measured by N₂ adsorption/desorption, and the obtained results are summarized in Table 3.2.1. The N₂ adsorption-desorption isotherm of the support and catalysts shows type-II isotherms (Figure 3.2.2) which are characteristic for nonporous materials.¹³⁷ As expected, the surface area and pore volume corresponding to the support and Cu catalysts are more or less the same.

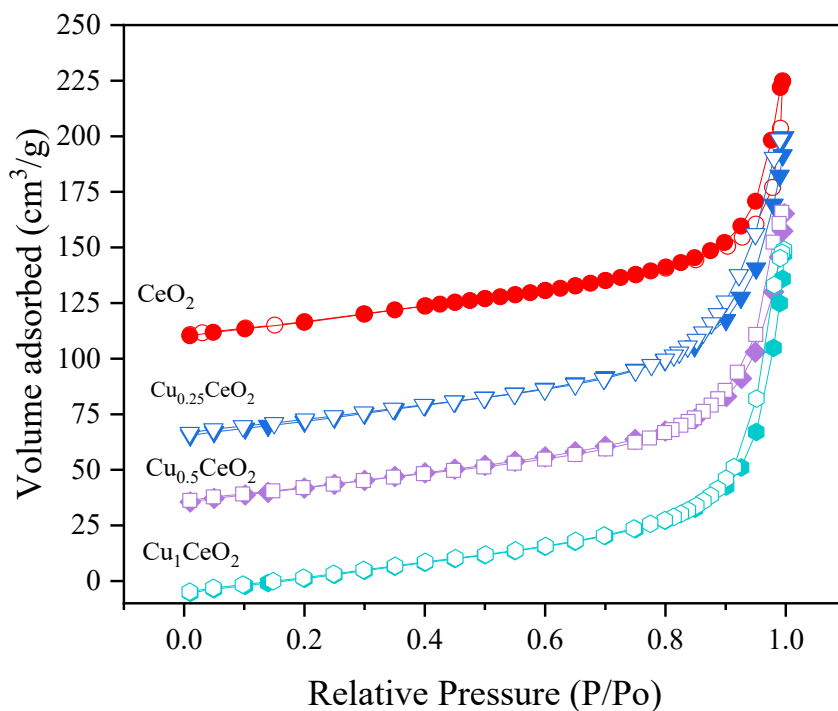


Figure 3.2.2. N₂ adsorption and desorption isotherms (filled and open symbols, respectively).

The XRD analysis of the support and Cu catalysts which is depicted in Figure 3.2.3, showed similar diffraction pattern of the fluorite structure of Ceria (ICDD PDF 01-080-5547).¹¹¹ No reflection peak attributed to CuO_x species was observed due to the low Cu loading.

Table 3.2.1. Elemental composition, surface, pore properties and crystallite size.

Catalysts	Cu wet%	S _{BET} (m ² ·g ⁻¹)	Pore volume (cm ³ ·g ⁻¹)	Average pore size (nm)	Crystallite size (nm)
CeO ₂	-	51	0.18	9.89	19
Cu _{0.25} CeO ₂	0.25	56	0.20	11.2	19
Cu _{0.5} CeO ₂	0.47	53	0.18	11.5	21
Cu ₁ CeO ₂	1	52	0.22	12.0	20

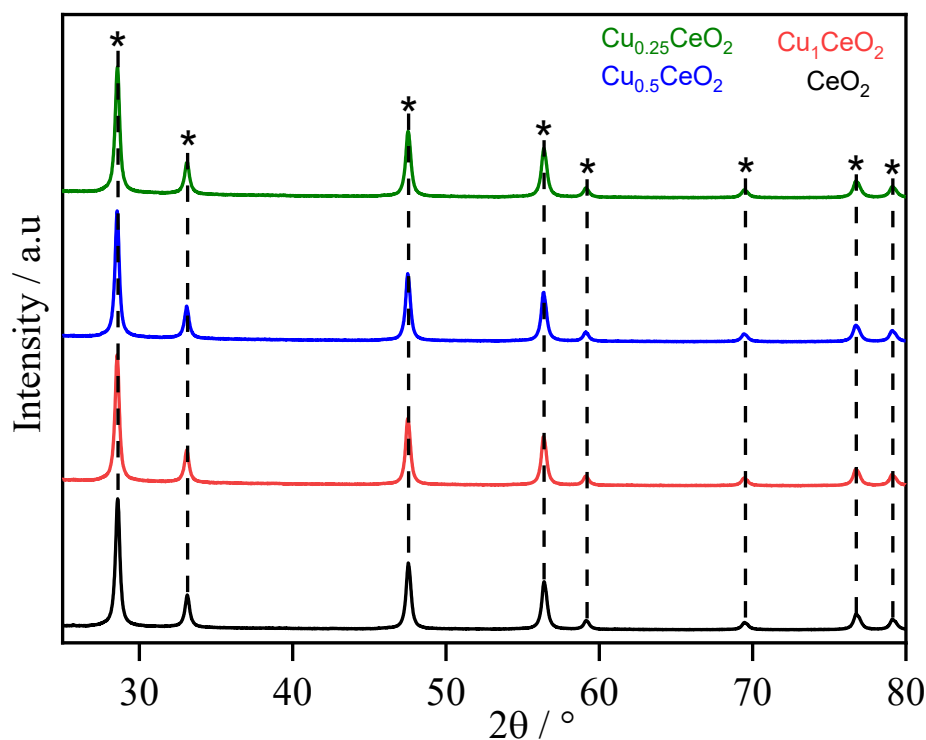


Figure 3.2.3. X-ray diffractograms of the Cu catalysts and bare CeO₂ support.

High-angle annular dark-field scanning transmission electron microscopy (HAADF-STEM) was carried out to obtain further information about the structure of catalysts. Due to the higher atomic number of Ce and thus its brighter appearance in the HAADF images, dispersed Cu cannot be seen directly in all materials (Figure 3.2.4, Figure A.5a-b, Figure A.7a-b). A differentiation between Ce and Cu is however possible with energy-dispersive X-ray spectroscopy (EDX), but in the case of Cu_{0.25}CeO₂, no Cu was detected. This is an indication of Cu being present either in highly dispersed form (and in this concentration below the detection limit of the EDX detector) or as bigger separate entities. As Cu is visible in minor amounts in the EDX spectra of Cu_{0.5}CeO₂ and Cu₁CeO₂ (See Figure A.6 and Figure A.8), an atomic dispersion of Cu on CeO₂ is implied. An agglomeration of Cu was not observed which is in accordance with recently reported results that Cu species are atomically dispersed on CeO₂ even when the Cu loading was higher than 1wt%.^{138, 139} Electron energy loss spectra (EELS) were recorded in the region of the Ce M-edge (Figure 3.2.4c-d), in order to gain insight into the Ce oxidation state in Cu_{0.25}CeO₂. The EEL spectra revealed the presence of Ce³⁺ (area 2) and Ce⁴⁺ (area 1) in the catalyst, and the Ce³⁺ seems to appear predominantly at the surface of the CeO₂ particles. The intensity of EELS signal of Ce³⁺ for the Cu-free support seems less than for the Cu-containing catalysts (Cu_{0.25}CeO₂ Figure 3.2.4d, Cu_{0.5}CeO₂ Figure A.5d, Cu₁CeO₂ Figure A.7d). These findings inferred that the presence of Cu species on the surface led to enhance the reducibility of the support (Figure A.4).

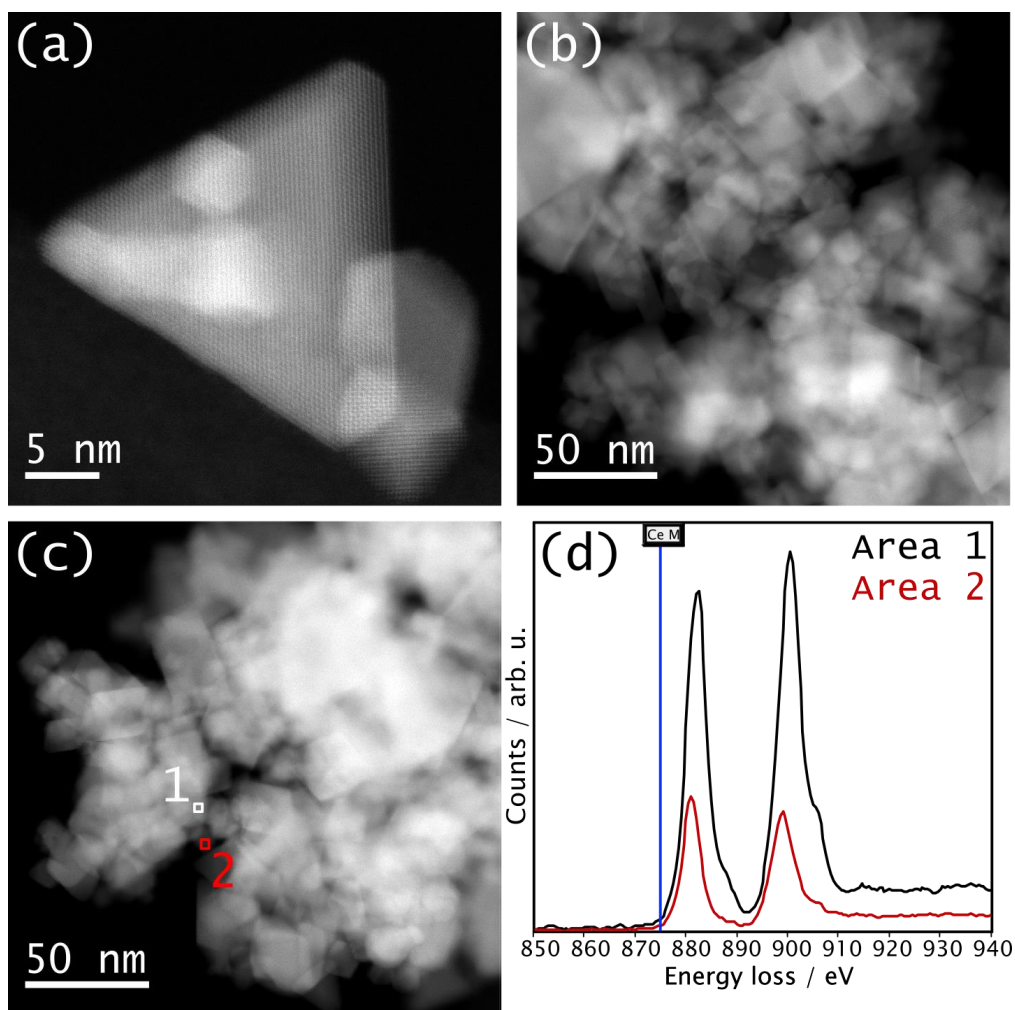


Figure 3.2.4. (a-b) Selected HAADF-STEM images of $\text{Cu}_{0.25}\text{CeO}_2$; (c) STEM-ADF image of $\text{Cu}_{0.25}\text{CeO}_2$ is shown with highlighted areas 1 and 2, of which the respective Ce M edge electron energy loss (EEL) spectra are provided in (d). Further results of STEM investigations are provided in the Appendix.

3.2.3 Hydrogen temperature-programmed reduction (H_2 -TPR)

The H_2 -TPR method has been carried out to investigate the reducibility of the Cu catalysts. The TPR profile of the bare support exhibits two reduction peaks at 428 °C and 852 °C. (Figure 3.2.5 black line). The first reduction peak at 428 °C assigned to the reduction of the surface Ce^{4+} into Ce^{3+} , while the peak at 852 °C is attributed to the reduction of bulk CeO_2 .¹⁴⁰ The TPR profile of the $\text{Cu}_{0.25}\text{CeO}_2$ (Figure 3.2.5-green line) showed two reduction peaks, a very sharp reduction peak at 148 °C (denoted α peak) which it is attributed to highly dispersed surface CuO ^{50, 106, 141} and at 181 °C (denoted β peak) corresponding to the reduction of Cu strongly interacting with CeO_2 , i.e. in the Cu-O-Ce moieties.^{57, 140} The reduction temperature peak (α) in this $\text{Cu}_{0.5}\text{CeO}_2$ is higher than the in other samples indicating the lack of formation of large particles of CuO on the surface and that the Cu species distribution is quite uniform.¹⁴⁰ Table 3.2.2 shows the quantitative analysis of the total hydrogen consumption in the temperature range 100-200°C for reduction of copper catalysts. It can be seen that the total H_2 consumption is higher than the stoichiometric amount required to obtain 100% reduction of CuO (Cu^{2+} to Cu^0) of the catalysts. It

was calculated from the integration of the overlap peaks (α) and (β). There is a large difference between the theoretical and experimental values of H₂ consumption. This suggests that reduction of cerium species on the surface must occur at low temperatures. This could also explain the disappearance of low temperature peak reduction at 428 °C in the TPR profile of the support when copper was added, because the presence of Cu improves the reducibility of the support in the catalyst forms more active surface oxygen species. The TPR profile of high copper concentration in Cu_{0.5}CeO₂ shows a broadening of the reduction peak (α) in the range of 100-160°C. This peak attributed to different copper species in this catalyst. More probably due to the formation of small CuO clusters which are strongly interacting with the CeO₂. With further increases in Cu content up to 1 wt% (Cu₁CeO₂) a broadening of the reduction peak (β) and the appearance of a new reduction peak (denoted γ) in the range (200-275 °C) are observed in H₂-TPR. This might be due to the formation of large and crystallized CuO particles since they are usually reduced at higher temperature than small CuO clusters.¹⁴⁰ This could be the reason for the low catalytic activity of Cu₁CeO₂.^{142, 143} These results indicate that the Cu species in these two catalysts are not uniform on the surface, in contrast to the lowest copper concentration of Cu_{0.25}CeO₂ which shows only sharp reduction peak centered at 148 °C (α). It could be suggested that the Cu species in this sample (Cu_{0.25}CeO₂) are homogenously distributed on the surface of the support and this observation is an agreement with the EPR spectrum at low temperature (105K) of the Cu_{0.25}CeO₂ since it shows more Cu²⁺ single sites.

Table 3.2.2. H₂-TPR results

Catalysts	Total amount of H ₂ theoretical (μ mol/g)	Total amount of H ₂ measured (μ mol/g)
Cu _{0.25} CeO ₂	39.37	262.15
Cu _{0.5} CeO ₂	74.01	303.8
Cu ₁ CeO ₂	157.48	360.7

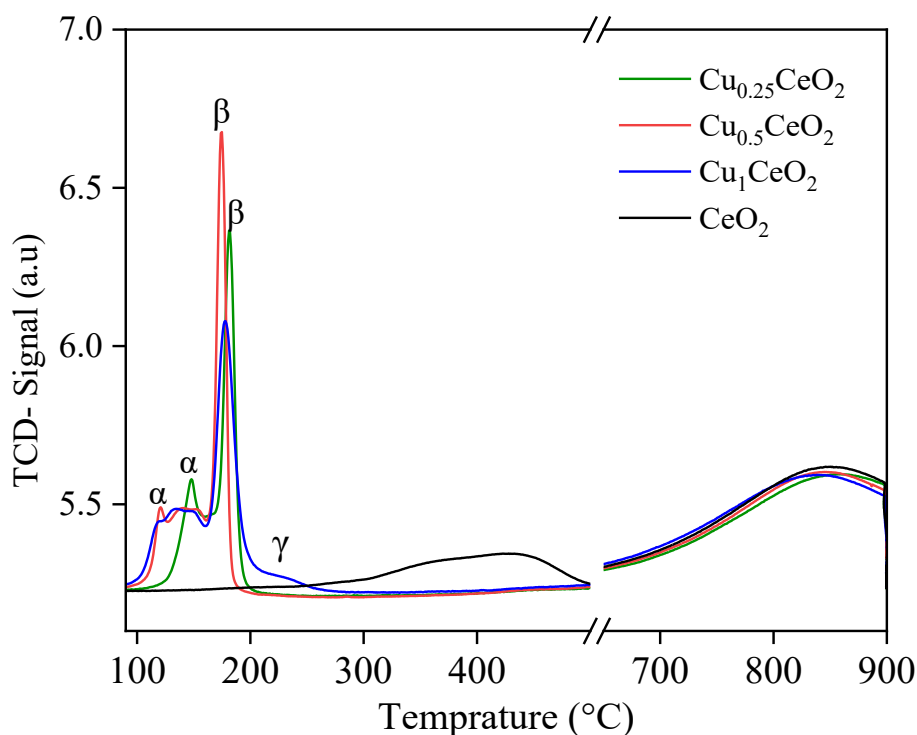


Figure 3.2.5. H₂-TPR profiles of pure support and Cu-containing catalysts from room temperature to 900 °C in 5% H₂/ Ar.

It obvious from Figure 3.2.1c that the Cu_{0.5}CeO₂ and Cu₁CeO₂ catalysts exhibit similar catalytic activity. To be sure that the catalytic activity is reproducible, new batches of Cu_{0.5}CeO₂ and Cu₁CeO₂ have been prepared and re-examined for PROX reaction. Surprisingly, the new prepared catalysts show similar catalytic activity (Figure A. 9) to that obtained from old batch (Figure 3.2.1), indicating the reproducibility of the adapted preparative procedure (ball milling). Since Cu_{0.5}CeO₂ and Cu₁CeO₂ show similar catalytic performance, in this section, we will investigate only Cu_{0.25}CeO₂ and Cu₁CeO₂ by operando methods.

3.2.4 Operando DRIFT

The operando DRIFT measurements were carried out under PROX reaction conditions to identify the adsorbed surface species. The DRIFT spectra were recorded for the pure support and Cu catalysts at temperature range 50 to 100 °C after reduction pretreatment in 10% H₂/ He at 250 °C. Figure 3.2.6 shows DRIFT spectra of support and two catalysts (Cu_{0.25}CeO₂ (a), and (b) Cu₁CeO₂) under PROX conditions. At all temperatures, the DRIFT spectra of Cu_{0.25}CeO₂ exhibits three IR bands at 2348, 2169 and 2106 cm⁻¹. The band at wave number 2106 cm⁻¹ is ascribed to the CO adsorbed on Cu⁺^{15, 144} and the intensity of this band gradually decreased as temperatures increased. The decrease in the Cu⁺-CO intensity with temperatures is due to the decrease in the number of adsorbed CO molecules, indicating that the CO conversion rises as temperatures of reaction increase. For Cu₁CeO₂, the intensity of Cu⁺-CO is still higher than the Cu⁺-CO intensity of Cu_{0.25}CeO₂ even at 100 °C. This indicates that the number

of adsorbed CO molecules in this sample is much higher than on $\text{Cu}_{0.25}\text{CeO}_2$. A peak observed in all samples at 2348 cm^{-1} for gas phase CO_2 indicates the beginning of the CO oxidation reaction at $50\text{ }^\circ\text{C}$, and the intensity of this peak was significantly increased as temperatures increases. For Cu_1CeO_2 catalyst, the intensity of IR peak at 2348 cm^{-1} higher than on $\text{Cu}_{0.25}\text{CeO}_2$ catalyst due to the high CO conversion to CO_2 . A small shoulder at 2051 cm^{-1} only at $50\text{ }^\circ\text{C}$ observed only in the spectra of Cu_1CeO_2 is attributed to CO adsorbed Cu^0 .^{73, 135} In addition, a band appears at 2169 cm^{-1} between 50 and $80\text{ }^\circ\text{C}$ (Figure 3.2.6a,b), its assignment is not clear based on literature data. It has been reported that the band at 2169 cm^{-1} was attributed to $\text{Cu}^+(\text{CO})_3$ or $\text{Cu}^{2+}\text{-CO}$ ^{145, 146} while in other literature this band was attributed to the CO gas contribution.¹²⁸ To clarify the assignment of the band (2169 cm^{-1}) in Figure 3.2.6a, we performed a control experiment (inset in Figure 3.2.6a) after feeding the reactants of the CO PROX reaction at RT into the DRIFT cell in absence and presence of catalyst ($\text{Cu}_{0.25}\text{CeO}_2$). It is obvious that, in absence of catalyst (black line), the spectrum shows a doublet band centered around 2107 cm^{-1} and 2169 cm^{-1} assigned to gaseous CO, whereas in presence of catalyst, the spectrum shows a similar band at 2169 cm^{-1} , while the band at 2116 cm^{-1} overlaps with $\text{Cu}^+\text{-CO}$ (red line). Finally, this experiment revealed that the band at 2169 cm^{-1} obtained in this IR (Figure 3.2.6a, b) spectra is attributed the CO contribution.

The DRIFT spectra (Figure 3.2.6c) of the pure support show a broad doublet band between 2090 and 2179 cm^{-1} typically assigned for gaseous CO whereas the IR band of CO_2 was not present since no catalytic activity was observed when the supported was tested in flu-plug reactor in the range of $50\text{-}150\text{ }^\circ\text{C}$. These results indicated that the CO adsorption on the Cu^+ species is an essential step in the cycle of catalytic activity in CO-PROX reaction. The results of mass spectroscopy recorded in parallel with reaction conditions for support and Cu-containing catalyst are displayed in (Figure A.10)

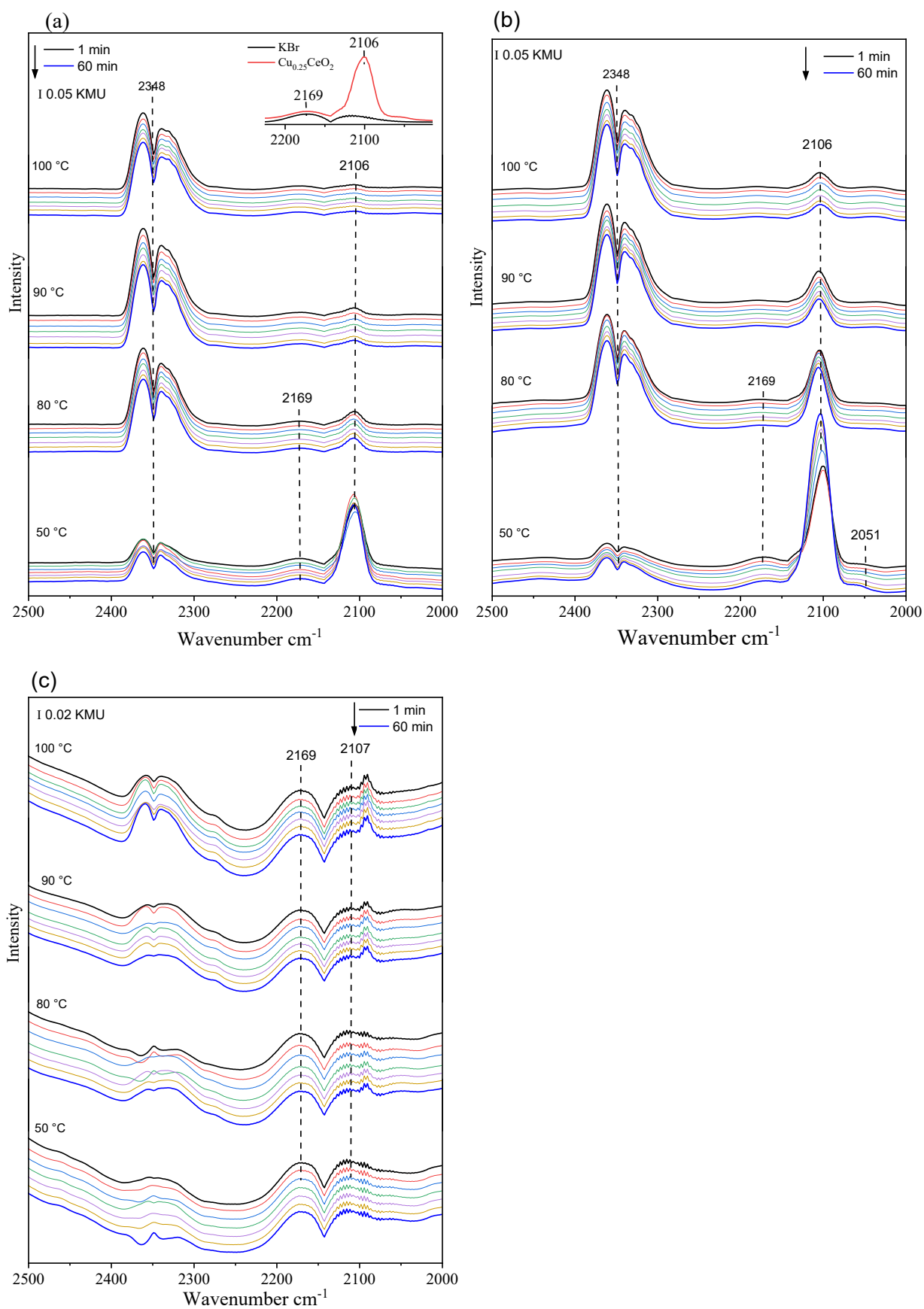


Figure 3.2.6. Operando DRIFT spectra of (a) $\text{Cu}_{0.25}\text{CeO}_2$, (b) Cu_1CeO_2 and (c) CeO_2 at 50, 80, 90 and 100 °C under CO-PROX gases 1% CO, 1% O₂, 80% H₂ and the rest is He.

3.2.5 Ex Situ and Operando EPR Studies

Since no direct evidence was observed from operando DRIFTS about the role of Cu^{2+} species, in situ/operando EPR investigations were conducted to follow the behaviour of Cu^{2+} species during the CO-PROX reaction. The bare support in this work exhibited, similar to previous studies on the CeO_2 and $\text{CeO}_2\text{-TiO}_2$ supports,^{147, 148} two weak signals: one at $g = 2.005$ assigned to oxygen vacancies and the other axial signal at $g_{\perp} = 1.963$ and $g_{\parallel} = 1.938$ (Figure A.11c), which has been ascribed to Ce^{3+} ions associated with a defect centre ($\text{Ce}^{3+}\text{-}\square$).¹⁵ Since the support itself is inactive for CO-PROX, we only show the operando EPR results at $90\text{ }^{\circ}\text{C}$ for $\text{Cu}_{0.25}\text{CeO}_2$ and Cu_1CeO_2 . The EPR spectra of the pre-oxidized Cu-containing catalysts (treated at $250\text{ }^{\circ}\text{C}$ in 5% O_2/He) in Figure 3.2.7 show an axial signal A at $g_{\parallel}(\text{A}) = 2.271$, $g_{\perp}(\text{A}) = 2.052$ with $A_{\parallel}(\text{A}) = 156.5\text{ G}$ and $A_{\perp}(\text{A}) = 19.4\text{ G}$ for both catalysts $\text{Cu}_{0.25}\text{CeO}_2$ and Cu_1CeO_2 , and an additional axial signal B $g_{\parallel}(\text{B}) = 2.290$, $g_{\perp}(\text{B}) = 2.059$ with $A_{\parallel}(\text{B}) = 119.5\text{ G}$ and $A_{\perp}(\text{B}) = 13.8\text{ G}$ for Cu_1CeO_2 assigned to Cu^{2+} ions species in tetragonally distorted octahedral coordination since $g_{\parallel} > g_{\perp} > g_e$.^{149, 150} The well-resolved hyperfine structure of the perpendicular component arises from a magnetic interaction between the spin of a single electron (d^9 , $S=1/2$) with the nuclear spin of Cu ($I= 3/2$), suggesting the presence of isolated Cu sites in both catalysts. The higher g_{\parallel} and lower A_{\parallel} values of signal B compared to those of signal A suggest a change in the Cu^{2+} coordination of signal B to square planar sites located at ceria subsurface positions. These sites normally showed lower reactivity towards CO oxidation compared to isolated Cu^{2+} species which are atomically dispersed on the surface of CeO_2 .¹⁵¹ The EPR signal intensity of isolated Cu^{2+} in Cu_1CeO_2 is lower than that in $\text{Cu}_{0.25}\text{CeO}_2$ (Figure 3.2.7). This may be due to the presence of EPR silent CuO particles at higher Cu loading (1wt%). This is suggested, too, from H_2 -TPR which showed a broad reduction peak at a range $200\text{-}275\text{ }^{\circ}\text{C}$. Moreover, during the pre-treatment of the oxidized catalysts in 10% H_2/Ar flow at $250\text{ }^{\circ}\text{C}$ for 1h, the EPR signal of the monomeric Cu^{2+} species decreased gradually with time in $\text{Cu}_{0.25}\text{CeO}_2$ but very fast in **Cu_1CeO_2** (Figure A.11a-b) due to reduction of Cu^{2+} to EPR-inactive Cu^+ ions. This indicates that the reduction of Cu^{2+} species in Cu_1CeO_2 is easier than in $\text{Cu}_{0.25}\text{CeO}_2$ due to the presence of CuO particles. This also agrees with H_2 -TPR results which showed a reduction peak (α) at lower temperature for Cu_1CeO_2 .

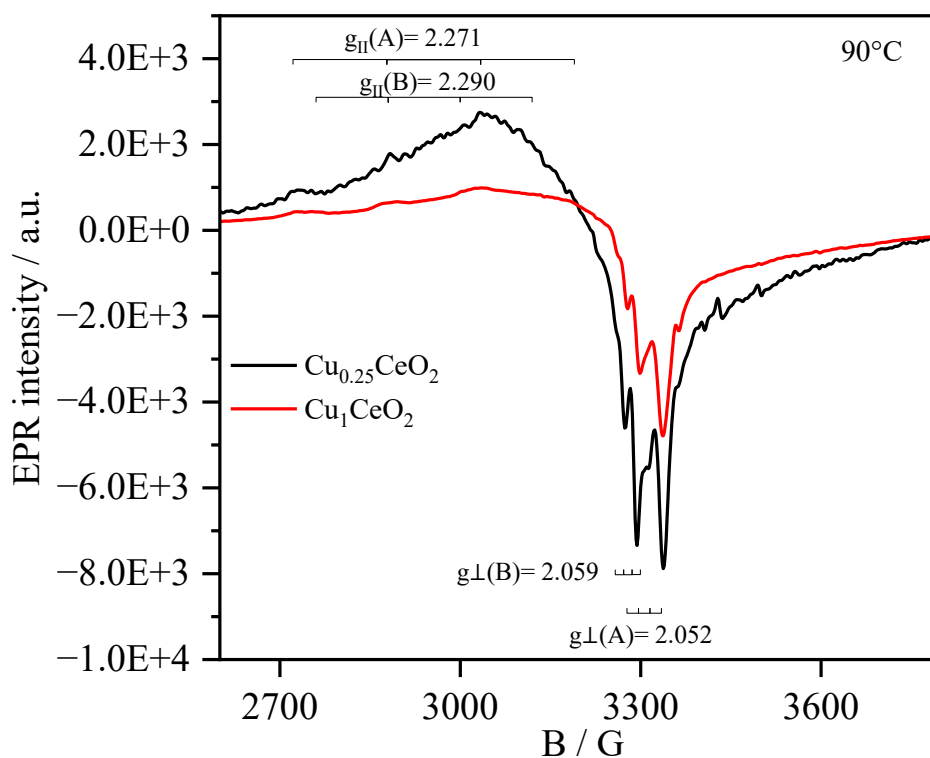


Figure 3.2.7. Ex situ EPR spectra of the pre-oxidized support and Cu catalysts at 90 °C.

When the reduced catalysts were exposed to a CO-PROX feed, the intensity of the EPR signals of Cu^{2+} ions remarkably increased again due to the reoxidation of the EPR-silent Cu^+ species to Cu^{2+} with different coordination environments (Figure 3.2.8). This effect was very quick for the most active catalyst ($\text{Cu}_{0.25}\text{CeO}_2$) which reached a steady state already after 4 minutes in which the intensities of the Cu^{2+} and O-vacancy signals do not change anymore at prolonged reaction times. This points to a rapid dynamic reduction/reoxidation cycle of Cu species by CO and O_2 , respectively, that renders the EPR intensity constant in time average.^{152, 153} (Figure 3.2.8, red line). In contrast, for the less active catalyst (Cu_1CeO_2), there was observed rapid growth of the Cu^{2+} signal intensity in the first 4 minutes which then decreased slightly before reaching a steady state after about 30 minutes. This suggests that initial Cu^+ sites in the pre-reduced catalyst are quickly re-oxidized in the first 4 min under PROX feed to Cu^{2+} species (Figure 3.2.8, Cu_1CeO_2 , red line). In subsequent redox cycles, these Cu^{2+} sites are reduced by CO and re-oxidized by O_2 again, whereby reduction seems faster than reoxidation as indicated by the decreasing EPR intensity between 4 and 60 min. This may be a reason for the lower CO oxidation rate on Cu_1CeO_2 , also observed in the catalytic tests (Figure 3.2.1. a). The CO_2 formation during operando EPR was also detected by online MS (Figure A.12).

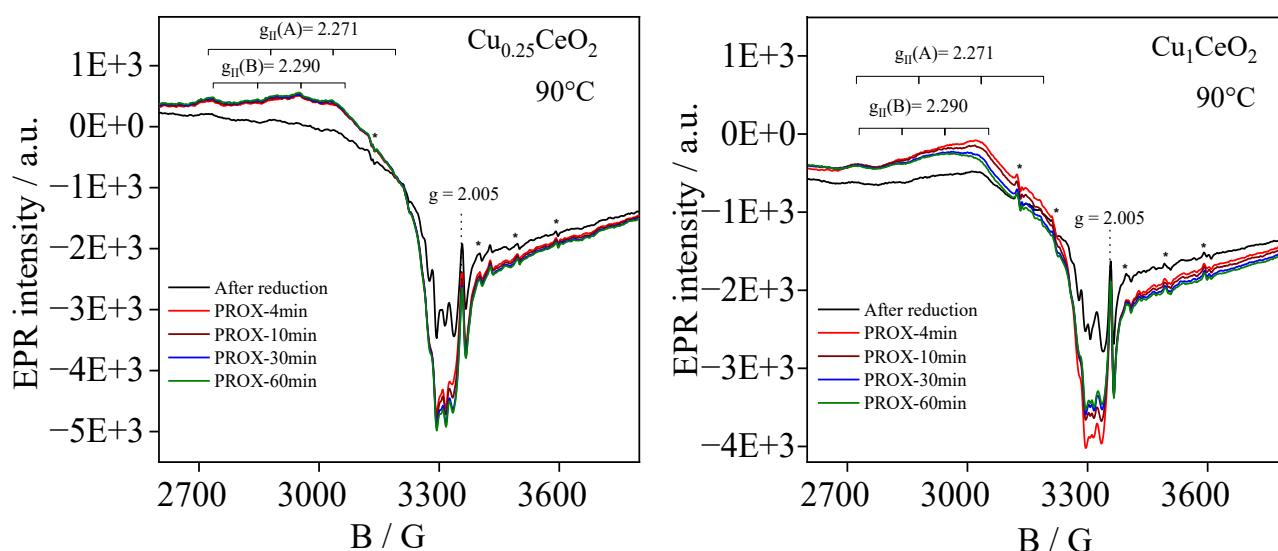


Figure 3.2.8. Operando EPR spectra at 90 °C of the catalysts (a) $\text{Cu}_{0.25}\text{CeO}_2$ and (b) Cu_1CeO_2 after pretreatment with 10% H_2/Ar flow and flushing with Ar, subsequent to a flow of (1% $\text{CO} + 1\% \text{O}_2 + 80\% \text{H}_2$)/ He for 60 min. (* EPR lines with a hyperfine structure sextet attributed to the presence of a trace amount of Mn^{2+} species).

A control EPR experiment was conducted for $\text{Cu}_{0.25}\text{CeO}_2$ catalyst to check whether the molecular of O_2 feed and/ or the lattice oxygen are involved in CO oxidation, Figure 3.2.9a showed no changes in the EPR signals after switching from H_2 to O_2 at 90 °C (Figure 3.2.9a, red and green lines), whereas a significant decreased was observed in the intensity at $g = 2.005$, which indicated that the oxidation of Cu^+ to Cu^{+2} occurs slowly by O_2 . This implies that the oxygen vacancies activate O_2 from the gas phase during the catalytic reaction. However, the EPR signal of Cu^{2+} species drastically decreased when $\text{Cu}_{0.25}\text{CeO}_2$ was exposed to a flow of CO (compare Figure 3.2.9a, red and blue lines). Previous studies reported that CO reduced a fully oxidized CuCeO_2 catalyst (around 70% of Cu^{2+}) at 27 °C, and the Cu^+ did not re-oxidize in the O_2 feed even at 100 °C,^{154, 155} indicating a stabilized Cu^+ oxidation state on the catalyst. These results prove that surface lattice oxygen, which may originate mainly from $\text{Cu}^{2+}\text{-O-Ce}^{4+}$ moieties, plays a decisive role in the preferential oxidation of CO molecules. The oxidation of CO molecules by surface lattice oxygen leads to the formation of oxygen vacancies and subsequent reduction of the EPR active Cu^{2+} species to EPR inactive Cu^+ . To elaborate the relationship between the amount of Cu^{2+} single sites and the catalytic activity, the variation of the double integral area of the EPR signals of Cu^{2+} under PROX conditions is shown in Figure 3.2.9b. Apparently, $\text{Cu}_{0.25}\text{CeO}_2$ showed 1.72 times a higher amount of the Cu^{2+} single species than Cu_1CeO_2 . This could be a major reason related to the higher activity obtained by $\text{Cu}_{0.25}\text{CeO}_2$ and this is in good agreement with recent work reported by our group, where we found that the rate of CO oxidation was increased by increasing the presence of single-site Cu ions on the surface.⁵⁵ Therefore, increasing Cu contents to 1 wt% led to form much less active Cu species cluster (Cu_2O) and that the lower activity observed by Cu_1CeO_2 catalyst attributed to

a large part of the Cu site might be hidden in those clusters and excluded from contact to reactants. Figure A.11d shows the relative amount of reduced copper species in the $\text{Cu}_{0.25}\text{CeO}_2$ catalyst (calculated from the subtraction of double integrals of EPR signals during 60 min oxidizing pretreatment by O_2 and reduction by CO) is much more than Cu_1CeO_2 . This indicates that the amount of Cu^{2+} in $\text{Cu}_{0.25}\text{CeO}_2$ which reduced to Cu^+ by CO is much more than Cu_1CeO_2 , suggesting that the Cu single sites on the surface which participated in the PROX reaction in $\text{Cu}_{0.25}\text{CeO}_2$ are higher than the other samples. Finally, it is more probably that $\text{Cu}_{0.25}\text{CeO}_2$ is a highly reducible catalyst, these results could explain the superior catalytic performance was obtained by $\text{Cu}_{0.25}\text{CeO}_2$.

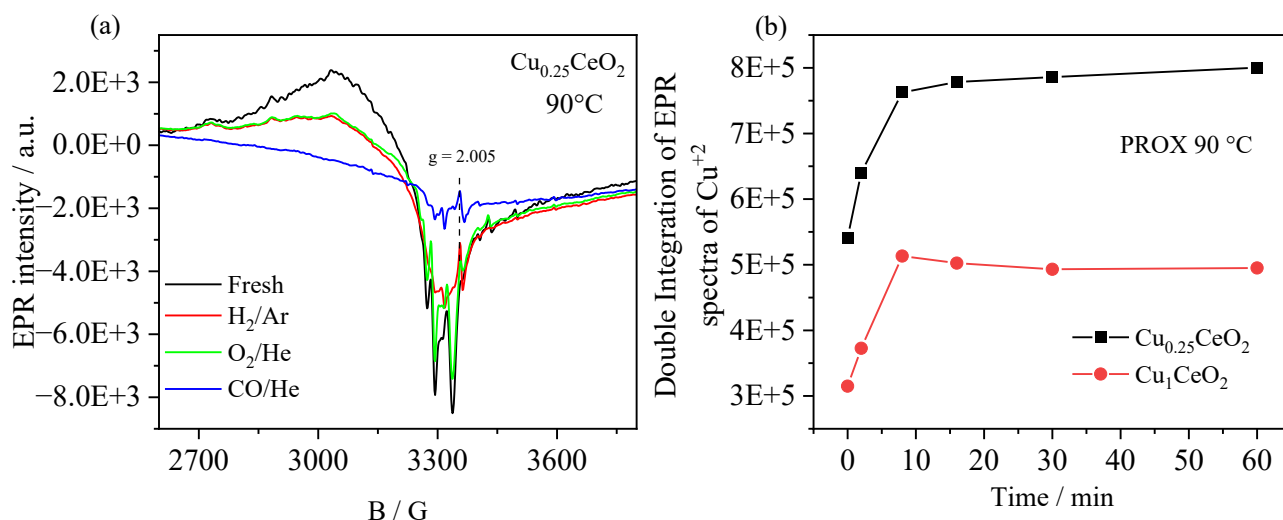


Figure 3.2.9. (a) $\text{Cu}_{0.25}\text{CeO}_2$ (recorded at 90 °C) after reductive pretreatment (red line) then exposure to 5% O_2/He (green line) and exposure to 5% CO/He (blue line). (b) Double integral area of the EPR signals of Cu^{2+} under PROX reaction.

3.2.6 Operando NAP-XPS

Operando NAP-XPS is carried out to acquire more information about the oxidation state of Ce species, since by EPR, it could not be shown any direct participation of Ce during the reductive pretreatment and PROX conditions, even at low temperature (-170 °C). Figure 3.2.10 demonstrates the binding energies corresponding to the Ce3d region of the pure support and $\text{Cu}_{0.25}\text{CeO}_2$ catalyst. The XPS spectra contain four spin-orbit doublets. The spectra were deconvoluted by four characteristic spin-orbit doublets, which can be attributed to the $3d_{5/2}$ and $3d_{3/2}$ spin-orbit components marked v and u, respectively. In general, the three spin-orbit doublets with peaks at 882.1/900.5 eV (v/u), 888.2/907.4 eV (v''/u'') and 897.8/916.1 eV (v'''/u''') are ascribed to Ce^{4+} and the other two doublets at 881.1/900.1 eV (v⁰/u⁰) and 884.5/903.0 eV (v'/u') are attributed to Ce^{3+} .¹¹⁵ The same calculation method (Eq 3.1.1) was used to estimate the Ce^{3+} as in the previous section.

The NAP-XPS spectra were recorded under different reaction conditions over CeO_2 support in Figure 3.2.10a. However, the results of this support are typically similar to those obtained by NAP-XPS for CeTiO_2 support in the previous section 3.1.3. Therefore, we will be not discussed these results in detail.

In contrast to the support, the Cu-containing catalyst ($\text{Cu}_{0.25}\text{CeO}_2$) showed a different behaviour. It can be seen from the Figure 3.2.10b that the percentage of Ce^{3+} on the surface significantly increased to about 26.3% when the $\text{Cu}_{0.25}\text{CeO}_2$ catalyst was pretreated with 10% H_2/He at 250 °C. This suggests that the reducibility of CeO_2 in the Cu-containing catalyst significantly improved when the Cu was added. However, the percentage of Ce^{3+} clearly decreased to 5.2% when the 5% O_2/He was introduced to the surface of the catalyst at 90 °C. This suggests that the O_2 feed refilled the oxygen vacancies thus formed by the reductive pretreatment under H_2 , which led to oxidize around 70% of reduced cerium species on the surface. This observation clearly explains the drastic decrease in the EPR signals at $g = 2.005$ after switching to oxygen (Figure 3.2.9a, compare red and green lines). Noteworthy, it is seen that the percentage of Ce^{3+} is significantly increased again from 5.2 % to 19.1 after switch the gas flow to 5% CO/He . This indicates that the removal of lattice oxygen is possible by CO , which led to the formation of oxygen vacancies and thus formation of more Ce^{3+} species. Finally, upon switching to the complete PROX mixture gases, the Ce^{3+} percentage on the surface dropped to 10.9%. This percentage value is higher than that observed under O_2/He , but lower than that under H_2/He , and at this step the catalyst starts to produce CO_2 as observed by mass spectrometer data. This indicates that the catalyst reached steady state reaction conditions. Due to the low content, Cu has not been directly observed in the Cu 2p spectra, this is a further indication that the Cu species is in the atomically dispersed form (Figure A. 13). The Cu_1CeO_2 catalyst also showed a similar NAP-XPS results (Figure A. 14) but due to the high copper content in this sample, the amount of Ce^{3+} present on the surface is much higher than the Ce^{3+} proportions on the lowest Cu content catalyst $\text{Cu}_{0.25}\text{CeO}_2$. This explains why this sample showed high activity in term of CO oxidation.

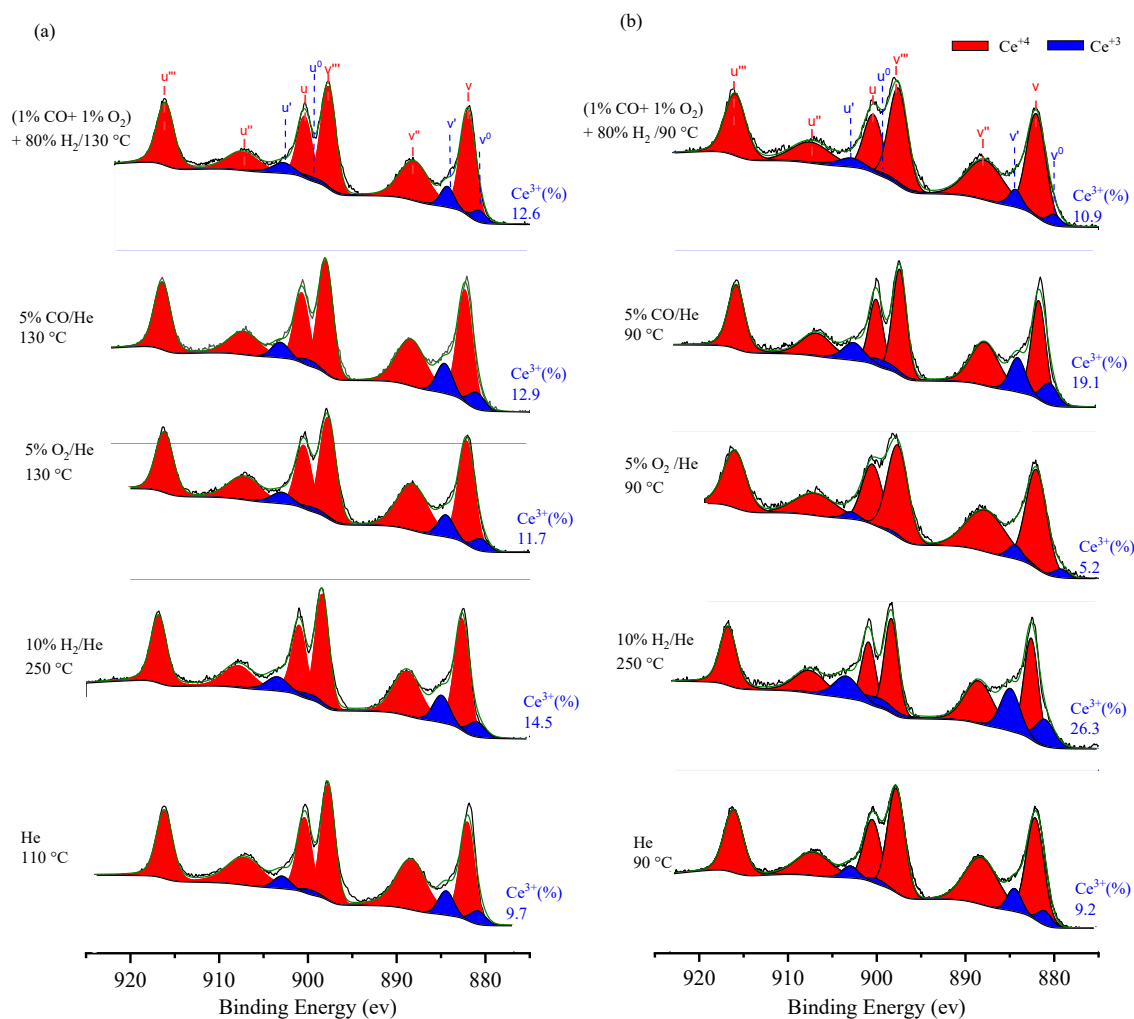
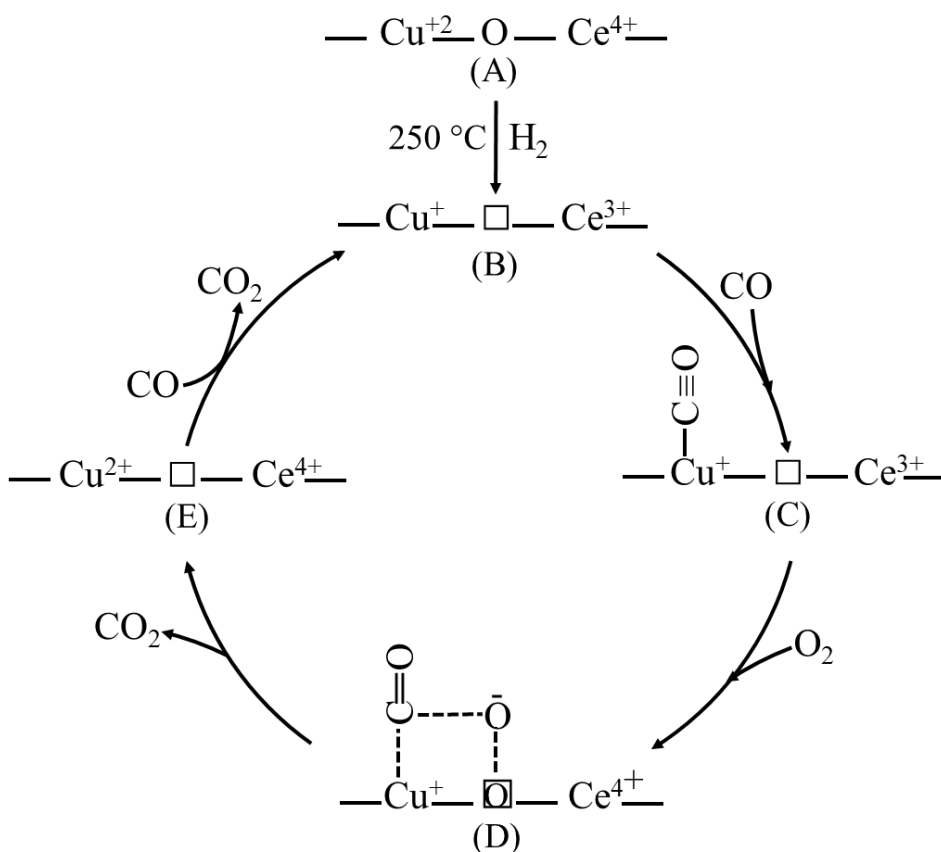


Figure 3.2.10. operando NAP-XPS of free Cu-support (a) and (b) Cu-containing catalyst ($\text{Cu}_{0.25}\text{CeO}_2$) in Ce region under different conditions.

3.2.7 PROX Reaction mechanism over the CuCeO_2 catalyst.

It has been widely reported that the mechanism of CO oxidation over a CuCeO_2 catalyst followed a Mars-van Krevelen mechanism, which involves chemical adsorption of CO on surface Cu^+ species to form $\text{Cu}^+\text{-CO}$ species, and further reaction with lattice oxygen species in Cu-O-Ce moieties. Subsequently, oxygen vacancies are refilled by the oxygen gas phase to complete the CO oxidation catalytic cycle reaction. According to the results from DRIFTS and EPR as well as NAP-XPS described in this section, we can propose the mechanism of PROX reaction over the CuCeO_2 catalyst. It can be seen that the easily reducible Cu single sites substituted in CeO_2 , i.e. $-\text{Cu-O-Ce}-$ is the active site for CO oxidation in the presence of hydrogen. After reductive treatment in hydrogen (Scheme 3.2.1B) the surface is reduced and thus some oxygen vacancies are generated as evidenced by the EPR. The formation of oxygen vacancies is accompanied by formation of Ce^{3+} and Cu^+ as shown by NAP-XPS and DRIFTS respectively. The reaction mechanism can be described in following steps given in Scheme 3.2.1. First, the CO is adsorbed on the Cu^+ species to form $\text{Cu}^+\text{-CO}$ (Scheme 3.2.1C) as indicated by the

IR band centered at 2106 cm^{-1} which it is clearly observed by operando DRIFTS. In the presence of molecular O_2 , the EPR spectra show that the Cu^{2+} signal slightly increased at the same time as the intensity of EPR signal at $g = 2.005$ decreased, while the amount of Ce^{3+} significantly decreased as proven by NAP-XPS. These results suggest that O_2 is activated by oxygen vacancies because the molecular O_2 selectively oxidizes the Ce^{3+} to Ce^{4+} , keeping Cu^+ more or less the same. Then surface-active oxygen species are able to oxidize carbon monoxide (Scheme 3.2.1D). After feeding only CO, The EPR signal of Cu^{2+} shows a remarkably decrease whereas the amount of Ce^{3+} significantly increased (as shown by NAP-XPS). This means that the surface oxygen reacts with CO leading to formation of CO_2 (Scheme 3.2.1E). Finally, all the operando techniques during the PROX conditions described above exhibit the existence of all three species Cu^+ , Cu^{2+} and Ce^{3+} . That means these species are responsible for the CO oxidation reaction over the CuCeO_2 in the presence of hydrogen. Therefore, we can propose that the active sites for PROX reaction are $\text{Cu}^{2+}\text{-O-Ce}^{4+} \rightleftharpoons \text{Cu}^+\text{-}\square\text{-Ce}^{3+}$ moieties which are connected by bridging oxygen on the surface of CeO_2 . These results are an agreement with the spectroscopic investigation in recently published work in the CO oxidation condition over CuCeTiO_2 catalyst.⁵⁵



Scheme 3.2.1. The proposed reaction mechanisms of the PROX reaction over CuCeO_2 Catalyst.

3.2.8 Conclusions

CO oxidation in the presence of 80% H₂ was performed in the range of 50-150 °C over CuCeO₂ catalysts with Cu loadings of 0.25, 0.5 and 1 wt. %. In the temperature window of 50-100 °C, a superior CO-oxidation rate and 100% CO₂-selectivity were observed by the lowest Cu contents (Cu_{0.25}CeO₂) catalyst. These catalysts were prepared by a simple ball-milling technique and offer an improved catalytic behaviour in the PROX reaction conditions than the most active catalyst reported in literature.

The Cu atomic efficiency greatly improved by decreasing the Cu content from 1 to 0.25 wt% and using a surface preparation method that led to a significant increase in the activity of Cu catalyst.

Organic solvents, toxic chemicals, and templates which were used in the sole-gel method and other complex methods are not required in this preparation method, making it a potentially practical approach for manufacturing copper-ceria catalysts in industrial applications. This simple strategy can also be extended to other inexpensive single atom catalysts such as Cu, Ni and Co etc., which may open the door for preparing highly efficient catalysts not only for the PROX reaction but also for other reactions such as methanol synthesis, water gas shift reaction, and CO-oxidation.

Based on the extensive spectroscopies investigation by in-situ/operando EPR, DRIFTS and NAP-XPS, we can suggest that the rapid shuttling of electrons between neighbouring Cu and Ce species and the vicinity cerium proportions on the support under PROX conditions form a dynamic redox pair $\text{Cu}^{2+}-\text{O}-\text{Ce}^{4+} \rightleftharpoons \text{Cu}^{+}-\square-\text{Ce}^{3+}$ which is the active site for CuCeO₂ catalysts, whereas the pure support shows no redox behaviour under PROX reaction conditions. This could be the mean reason why it is inactive.

For the CuCeO₂ catalysts investigated in this work, the Cu_{0.25}CeO₂ possesses the highest contents of Cu²⁺ single sites, and a strong interaction between Cu and ceria (as evidenced by EPR and H₂-TPR characterizations), indicating that the Cu species in this sample are highly dispersed on the surface. Therefore, this enhances the CO adsorption on Cu⁺ and activation of oxygen molecules, thus showing the highest activity for CO oxidation.

The high CO₂-selectivity values of Cu_{0.25}CeO₂ sample even at high temperatures (125-150 °C) are attributed to low tendency of Cu single sites for hydrogen activation at such high temperatures. This could be clearly confirmed by H₂-TPR profile for this sample (Figure 3.2.5, green line).

3.3 The impact of the support on the PROX activity of $\text{Cu}_{0.25}\text{CeO}_2\text{-3nm}$ and $\text{Cu}_{0.25}\text{CeO}_2\text{-25nm}$ catalysts

Previous section 3.2 has given considerable insight into the influence of Cu loadings on the catalytic activity of CuCeO_2 system under CO-PROX conditions. However, there is still an open question: How does the crystallite size, reducibility, and redox properties of CeO_2 affect the activity? Therefore, in this section, two Cu catalysts with optimal Cu loading (0.25 wt%) were prepared by ball-milling using two CeO_2 with different crystallite size.

3.3.1 Catalytic performance of $\text{Cu}_{0.25}\text{CeO}_2\text{-3nm}$ and $\text{Cu}_{0.25}\text{CeO}_2\text{-25nm}$ catalysts

The catalytic activities of the catalysts were examined after reductive pretreatment in 10 % of H_2 at 250 °C for 1 h. In Figure 3.3.1, the CO conversion and CO_2 -selectivity over the pure supports and Cu catalysts are plotted in the temperature range of 50-150 °C. The CeO_2 supports showed negligible activity, in agreement with the previous reports.^{39, 67, 156} This implies that the active site for CO oxidation should involve the participation of Cu species. In contrast to the bare supports, all $\text{Cu}_{0.25}\text{CeO}_2\text{-25nm}$ and $\text{Cu}_{0.25}\text{CeO}_2\text{-3nm}$ catalysts show catalytic activity for CO oxidation to CO_2 which increases with increasing reaction temperature (Figure 3.3.1). However, the $\text{Cu}_{0.25}\text{CeO}_2\text{-(25nm)}$ catalyst exhibits a higher CO conversion in comparison with the other catalyst and reached 100 % conversion at 150 °C (Blue line in Figure 3.3.1a). While $\text{Cu}_{0.25}\text{CeO}_2\text{-(3nm)}$ catalyst displayed a slight increase in the CO conversion with increasing reaction temperature and reached only 20% at 150 °C. The major difference in the catalytic performance for both samples is the CO_2 -selectivity values. $\text{Cu}_{0.25}\text{CeO}_2\text{-(3nm)}$ catalyst has 90% CO_2 -selectivity in the range of high temperature 150 °C, while the CO_2 -selectivity of $\text{Cu}_{0.25}\text{CeO}_2\text{-(25nm)}$ remarkably decreased to 64% when the temperature of the reaction reached 150 °C. The catalytic stability is plotted as a function of time on stream in Figure 3.3.1c, d. Moreover, catalytic stability is a critical parameter for heterogeneous catalysts, particularly for industrial production. The stability of $\text{Cu}_{0.25}\text{CeO}_2\text{-(25nm)}$ was performed in the range of low temperature (PEMFC) fuel cell working temperature window (90 °C). As displayed in Figure 3.3.1c, no deactivation was observed for $\text{Cu}_{0.25}\text{CeO}_2\text{-(25nm)}$ catalyst after 75 h of the CO-PROX reaction, the CO conversion remaining around 50 % and the CO_2 selectivity always fluctuating between 92 to 97 %. The $\text{Cu}_{0.25}\text{CeO}_2\text{-3nm}$ catalyst showed negligible activity at reaction temperatures lower than 100 °C ($X_{\text{CO}} < 2\%$). Therefore, the catalytic stability was performed at high temperatures (150 °C, Figure 3.3.1d). Achieving high selectivity (90% CO_2 -selectivity) at high temperatures is a key factor for improving the overall efficiency and performance of high-temperature proton exchange membrane fuel cell applications. One possibility to explain the better CO_2 -selectivity of $\text{Cu}_{0.25}\text{CeO}_2\text{-(3nm)}$ at high temperatures might be

attributed to the high existence amount of Cu single species on the surface. Indeed, as will be illustrated below, in situ EPR results detected higher Cu single sites on $\text{Cu}_{0.25}\text{CeO}_2$ -(3nm) catalyst. The desirable stability can be ascribed to the strong metal support interaction. The results showed that catalysts prepared in this work have a promising application prospect in the long-time reaction process.

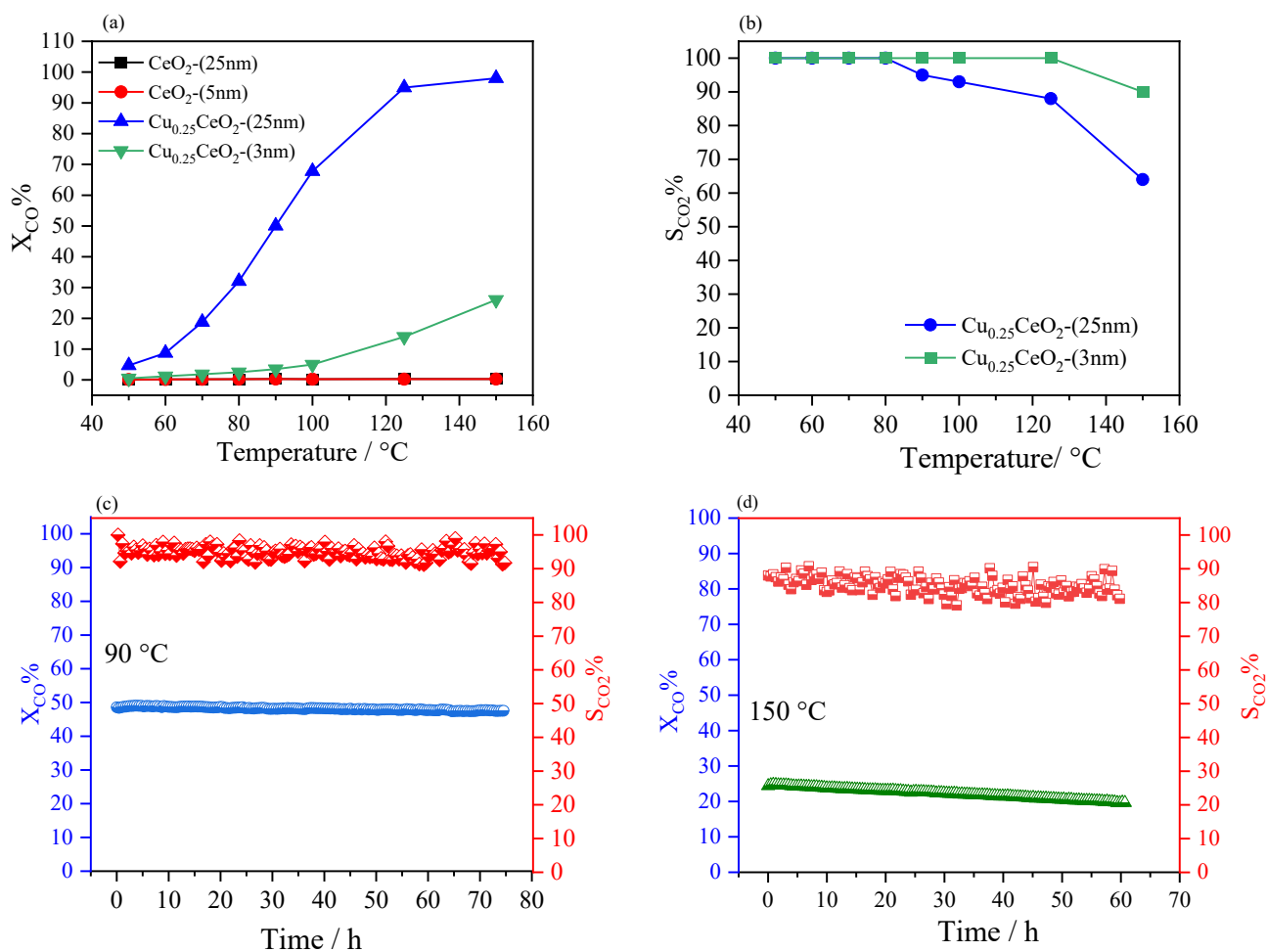


Figure 3.3.1. (a) CO conversion, (b) selectivity towards CO_2 as a function of the temperature over the catalysts $\text{Cu}_{0.25}\text{CeO}_2$ -(25nm), $\text{Cu}_{0.25}\text{CeO}_2$ -(3nm) and supports, and (d) catalytic stability over the catalyst $\text{Cu}_{0.25}\text{CeO}_2$ -(3nm).

N_2 adsorption/desorption isotherms of the supports and Cu catalysts are displayed in Figure 3.3.2a, b. All samples show type II isotherms. This indicates that these catalysts are nonporous materials.¹³⁷ The surface area, average pore size, pore volume, and Cu content of the catalysts are listed in Table 3.3.1.

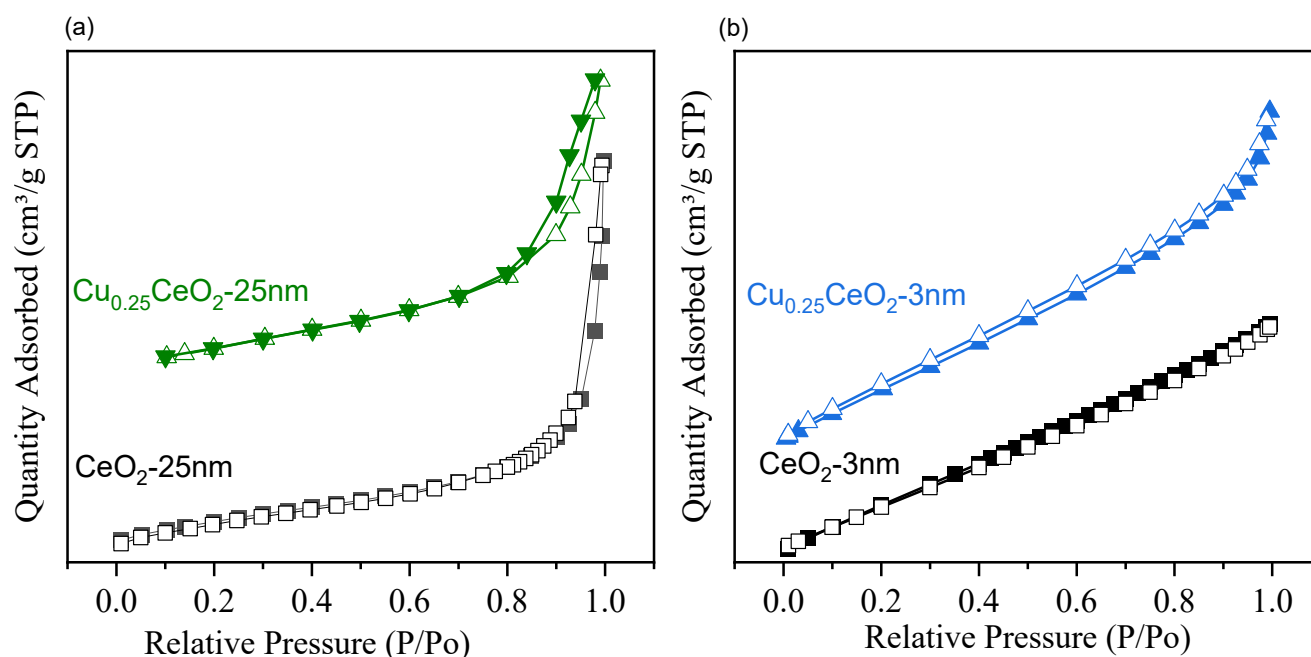


Figure 3.3.2. N₂ adsorption and desorption isotherms (filled and open symbols, respectively): (a) CeO₂-25nm, Cu_{0.25}CeO₂-25nm and (b) CeO₂-3nm, Cu_{0.25}CeO₂-3nm.

The XRD patterns of the supports and prepared Cu catalysts with the same Cu content in Figure 3.3.3 shows the existence of cubic fluorite CeO₂ structure (JCPDS card no: 01-080-5547).¹¹¹ The broadening of the diffraction patterns of CeO₂-3nm indicates that this support has a very small crystallite size. In contrast, the XRD peaks of the Cu_{0.25}CeO₂-3nm catalyst become sharper, indicating that some bigger crystallite formation due to the high temperature was used under calcination conditions. For CeO₂-25nm, no changes were observed in crystallite size when Cu was loaded due to the lower content. No diffraction peaks correspond to the presence of Cu species.

Table 3.3.1. Elemental composition, surface area, pore properties and crystallite size.

Catalysts	Cu wt%	S _{BET} (m ² ·g ⁻¹)	Pore volume (cm ³ ·g ⁻¹)	Average pore size (nm)	Crystallite size (nm)
CeO ₂ -3nm	-	25	0.02	3.49	3
CeO ₂ -25nm	-	45	0.13	10.5	26
Cu _{0.25} CeO ₂ -3nm	0.22	26	0.03	4.23	8
Cu _{0.25} CeO ₂ -25nm	0.26	43	0.12	9.13	27

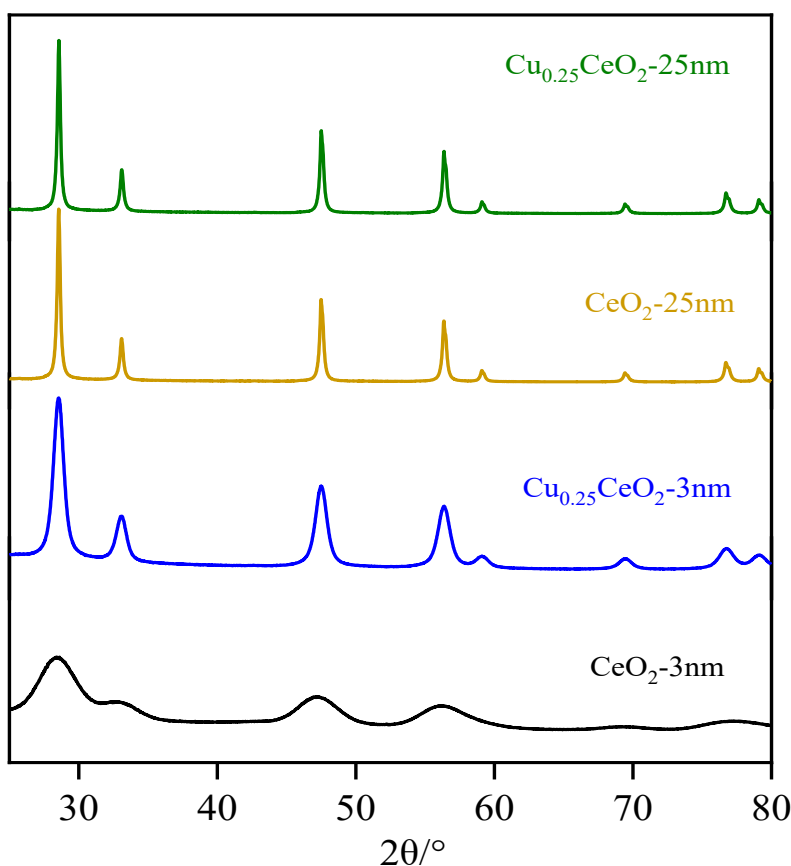


Figure 3.3.3. X-ray diffractograms of the supports and Cu catalysts.

The H₂-TPR of bare support (CeO₂-25 nm) shows a broad reduction peak expanded over a temperature range of 300-525 °C with well-defined two peaks at 314 and 475 °C. The first reduction peak at 314 °C is attributed to the reduction of Ce⁴⁺ on the surface of the support, while the second reduction at 475 °C is ascribed to the reduction of Ce⁴⁺ on the sub-surface. Due to oxygen mobility, this reduction peak appears at higher temperatures.¹⁴⁰ The TPR profile of supported Cu catalysts (Cu_{0.25}CeO₂-25nm) showed a distinct reduction behaviour with two small shoulders at 117 and 129 °C which can be assigned to the reduction of Cu²⁺ species on the surface of the support (Figure 3.3.4).¹⁴² In addition, a sharp reduction peak at a higher temperature of 158 °C was also observed in this H₂-TPR profile, which ascribed to the reduction of highly interacted Cu species.⁵⁸ The disappearance (Figure 3.3.4, compare black and blue lines) of the reduction peaks of surface Ce⁴⁺ of the bare support could be attributed to the facile reduction of these species after Cu loading due to H₂ activation over Cu and subsequent spillover over the support. Based on these results, one may attribute the sharp peaks at 158 °C to the reduction of both Cu²⁺ and surface Ce⁴⁺ in Cu-O-Ce moieties.¹⁰⁶ The TPR profile of the CeO₂-3nm (Figure 3.3.4 red line) shows a broad reduction peak at higher reduction temperatures of 400-575 °C in comparison with CeO₂-25nm, which is also ascribed to the reduction of surface Ce⁴⁺.^{55, 106} For Cu_{0.25}CeO₂-3nm, there is a very small shoulder at 166 °C also attributed to the reduction of Cu²⁺ and a very broad reduction peak

centered at 360 °C, which is ascribed to the reduction of Cu^{2+} as well as Ce^{4+} on the surface.¹⁵⁷ These results reveal that $\text{Cu}_{0.25}\text{CeO}_2\text{-25nm}$ is much more reducible in comparison with other catalyst and this could explain the high catalytic activity obtained at low temperatures (50-150 °C) over $\text{Cu}_{0.25}\text{CeO}_2\text{-25nm}$. Conversely, the smallest shoulder peak at 166 °C suggests that the amount of easily reducible Cu species (reduced at ≤ 250 °C) that are responsible for the PROX activity are very less on $\text{Cu}_{0.25}\text{CeO}_2\text{-3nm}$ in comparison with $\text{Cu}_{0.25}\text{CeO}_2\text{-25nm}$ catalyst.

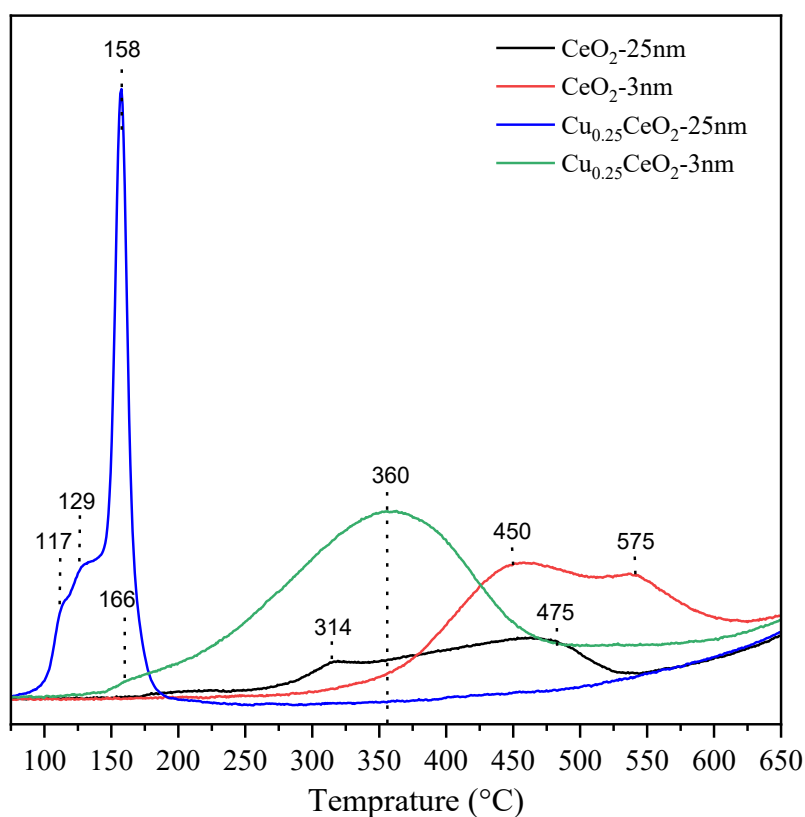


Figure 3.3.4. H₂-TPR profiles of pure supports and Cu-containing catalysts from room temperature to 900 °C in 5% H₂/ Ar.

3.3.2 In situ DRIFTS investigations

In situ DRIFTS of $\text{Cu}_{0.25}\text{CeO}_2\text{-25nm}$ and $\text{Cu}_{0.25}\text{CeO}_2\text{-3nm}$ catalysts (Figure 3.3.5) displays a spectral region of the formation of CO₂ and carbonyl species over both catalysts. After reductive pretreatment in hydrogen 10% at 250 °C for 1h, the temperature decreased to 90 °C, and then the sample was exposed to PROX mixture (1% CO, 1% O₂, 80% H₂)/ He. Two weak peaks appearing at 2107 and 2171 cm⁻¹ could be attributed to gaseous CO over $\text{Cu}_{0.25}\text{CeO}_2\text{-3nm}$ (Figure 3.3.5b).¹²⁸ For $\text{Cu}_{0.25}\text{CeO}_2\text{-25nm}$ catalyst, the IR spectra show a sharp peak at 2100 cm⁻¹ ascribed to the C=O stretch of CO species indicating the adsorption of CO on Cu⁺ sites,¹⁵⁸ while no peak of CO adsorption on Cu⁺ was detected over $\text{Cu}_{0.25}\text{CeO}_2\text{-3nm}$ catalyst. The reason for this behaviour is not clear in all details, but it could be attributed to the deep reduction of Cu species to inactive Cu⁰ during CO oxidation. The oxidation of the reduced Cu species to Cu²⁺ was excluded since no increase of the Cu²⁺ signal was observed from EPR

investigations (Figure 3.3. 7b). Another reason one could be considered is reaching the fast oxidation of Cu^+ into Cu^{2+} during the reaction (by O_2), which cannot be seen by DRIFTS. Therefore, a control experiment under flowing only CO/He was performed in an attempt to detect Cu^+ and the obtained DRIFT spectra are shown in Figure 3.3.5c. The spectra clearly reveal the absence of Cu^+ -CO band, which, therefore, excludes the assumption of the rapid oxidation of Cu^+ during the reaction. According to these results, one can attribute the absence of Cu^+ -CO in the DRIFT spectra in Figure 3.3.5c to the reduction of Cu^{2+} into Cu metal.

Both catalysts show two peaks centered at 2349 cm^{-1} corresponding to the gaseous CO_2 . With an increase in the reaction temperature, the peak of Cu^+ -carbonyl species decreased and slightly shifted to the lower wavenumber (Figure 3.3.5a). This was accompanied by increasing the CO_2 peak intensity due to the increase of the CO conversion to CO_2 over $\text{Cu}_{0.25}\text{CeO}_2\text{-25nm}$. The redshift for the band of Cu^+ -carbonyl indicates a strong CO adsorption and a strong π -back-bond, and thus there is a strongly interacting between the Cu species and support for $\text{Cu}_{0.25}\text{CeO}_2\text{-}(25\text{nm})$ catalyst.¹⁴⁴ The high intensity of Cu^+ -carbonyl is shown in Figure 3.3.5a, indicating that a higher amount of Cu^+ -carbonyl species is formed over the $\text{Cu}_{0.25}\text{CeO}_2\text{-}(25\text{nm})$ which is attributed to the superior catalytic activity of this catalyst.

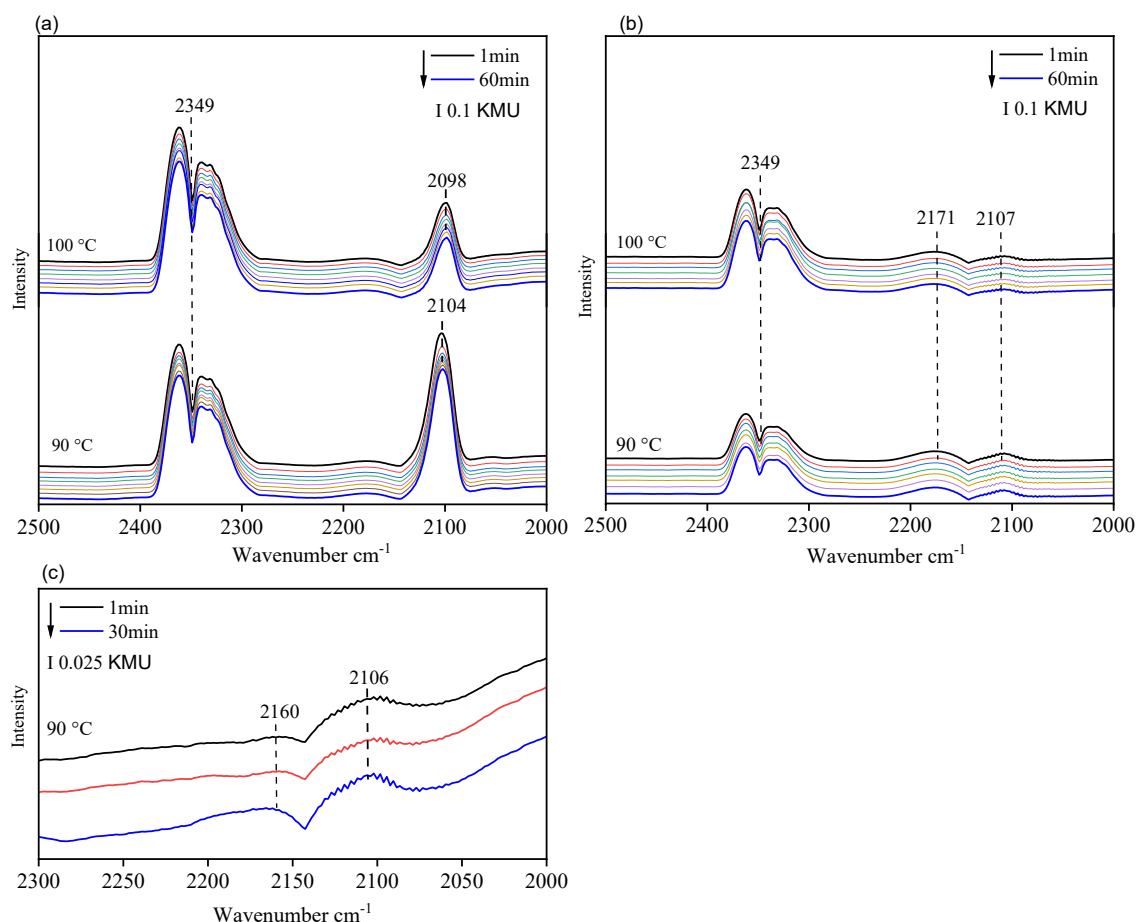


Figure 3.3.5. In situ DRIFT spectra of (a) $\text{Cu}_{0.25}\text{CeO}_2\text{-25nm}$, (b) $\text{Cu}_{0.25}\text{CeO}_2\text{-3nm}$ at 90 and 100 °C under CO-PROX conditions, (c) DRIFTS spectra of the $\text{Cu}_{0.25}\text{CeO}_2\text{-3nm}$ catalyst exposed to a flow of 15 ml/min of 1% CO/He at 90 °C for 30m min (after reductive pretreatment under 10% H_2/He for 1h).

3.3.3 Ex Situ and in situ EPR studies

EPR spectra of Cu-free supports and Cu catalysts are shown in Figure 3.3.6. The EPR spectrum of CeO₂-3nm support (Figure 3.3.6a) shows a sharp signal arising from paramagnetic oxygen defects such as O[•] and /or O₂^{•-} in the range of $g = 2.009$ and minor Ce³⁺ species ($g_{\perp} = 1.963$).^{120, 159, 160}

The EPR spectra of Cu_{0.25}CeO₂-25nm and Cu_{0.25}CeO₂-3nm catalysts recorded at -170 °C are presented in Figure 3.3.6b. The EPR spectra of both samples show the presence of isolated Cu²⁺ while the EPR intensity of Cu²⁺ species in the Cu_{0.25}CeO₂-3nm sample is around 12.6 times higher than the EPR intensity of Cu_{0.25}CeO₂-25nm catalyst. This suggests that the presence of Cu species Cu_{0.25}CeO₂-25nm is highly dispersed in comparison with the Cu_{0.25}CeO₂-25nm sample.

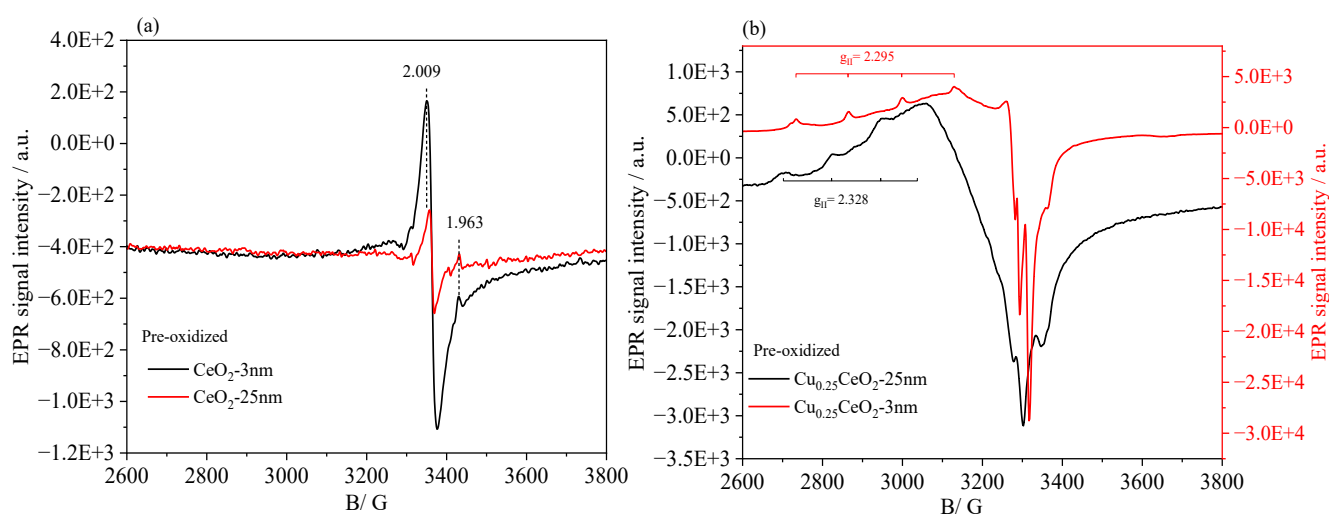


Figure 3.3.6. EPR spectra of the pre-oxidized Cu-containing catalysts recorded at -173 °C (a) and supports (b).

After 1h reductive pretreatment in 10 %H₂ at 250 °C, the EPR signals of Cu²⁺ in both catalysts remarkably decreased due to the reduction of Cu²⁺ ions to EPR silent, more probably Cu⁺ species or to inactive Cu⁰ (compare black and red lines, Figure 3.3. 7). However, the DRIFTS results of Cu_{0.25}CeO₂-3nm Figure 3.3.5b did not detect any Cu⁺-CO species, this could be due to the direct formation of Cu⁰. The EPR spectrum of reduced Cu_{0.25}CeO₂-3nm catalyst shows two different values of g (remarked as $g_{\parallel} (A_1) = 2.295$ and $g_{\parallel} (A_2) = 2.236$). This shift might be attributed to the change in the geometry of Cu²⁺ species. When the reduced Cu_{0.25}CeO₂-3nm sample was exposed to a mixture of ROX (1% CO, 1% O₂ and 80% H₂) in He, the EPR spectrum shows that the sample remained in the reduced form and did not change even after 1 h at 90 °C. This suggests that the reoxidation of the Cu⁰ species process in this sample is very difficult. Figure 3.3.6a shows that CeO₂-3nm has much higher amounts of oxygen vacancy than CeO₂-25nm. These oxygen vacancies could be responsible for stabilizing Cu⁰, which leads to preventing the reoxidation of these species to Cu²⁺. This conclusion is consistent with XPS results in Figure 3.3.8, which shows a decrease in the signal intensity of Ce³⁺ (oxygen vacancy) after adding

copper, providing direct evidence of interaction between oxygen vacancy and copper species. The EPR spectra of $\text{Cu}_{0.25}\text{CeO}_2\text{-3nm}$ under reduction and PROX conditions became very complicated. In this case, we will not be discussed this in detail. For the $\text{Cu}_{0.25}\text{CeO}_2\text{-25nm}$ catalyst, after exposing the reduced catalyst to PROX feed the EPR signal of Cu^{2+} remarkably increased again due to the reoxidation of Cu^+ silent EPR species to Cu^{2+} . These results indicate that the redox activity of $\text{Cu}_{0.25}\text{CeO}_2\text{-25nm}$ is very easy in comparison with $\text{Cu}_{0.25}\text{CeO}_2\text{-3nm}$ catalyst. The highest activity was observed by the $\text{Cu}_{0.25}\text{CeO}_2\text{-25nm}$ catalyst, which is attributed to the higher redox activity of this sample.

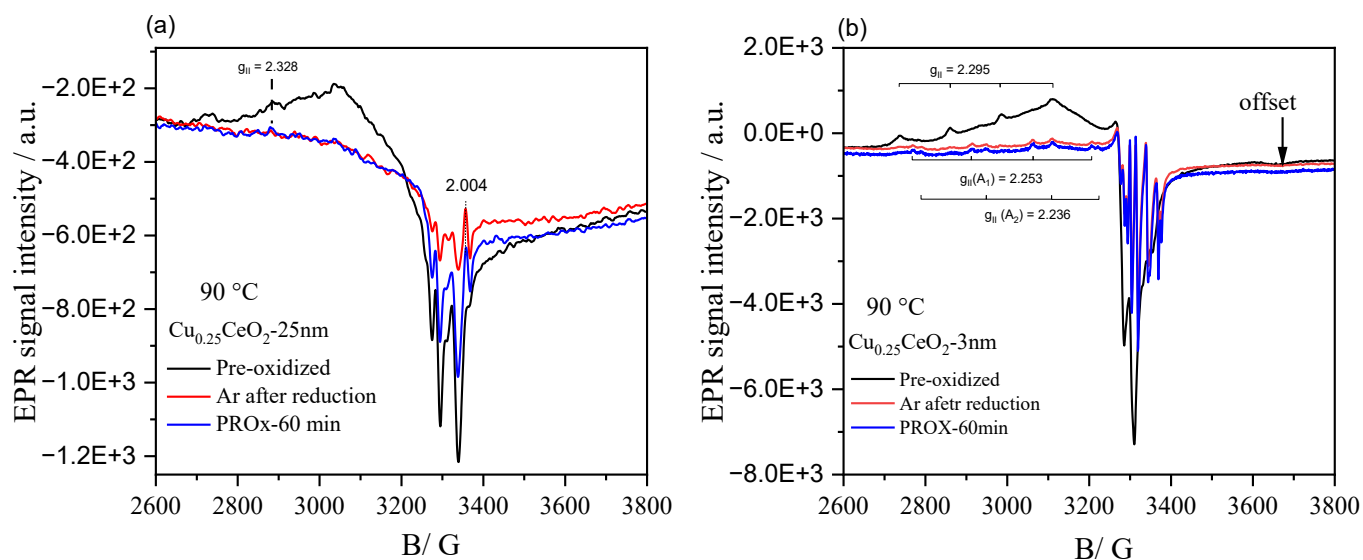


Figure 3.3. 7. Operando EPR spectra at 90 °C of the catalysts (a) $\text{Cu}_{0.25}\text{CeO}_2\text{-25nm}$ and (b) $\text{Cu}_{0.25}\text{CeO}_2\text{-3nm}$ in the pre-oxidized form (black line), after pretreatment with 10% H_2/Ar flow and flushing with Ar (red line), subsequent to a flow of (1% CO + 1% O_2)/He + 80% H_2 /He for 60 min (blue line).

3.3.4 Ex Situ XPS investigations

The XPS results of $\text{CeO}_2\text{-3nm}$ (Figure 3.3.8a) show that the amount of Ce^{3+} species on the surface is higher than on the surface of $\text{Cu}_{0.25}\text{CeO}_2\text{-3nm}$ catalyst. This is consistent with the sharp EPR signal at $g = 2.009$ (Figure 3.3.6a, black line). According to the Mars and Van Krevelen mechanism, a high amount of Ce^{3+} suggests more oxygen vacancy formation (Table 3.3.2).¹⁶¹

In general, small CeO_2 particle size can be enhanced the existence of a high Ce^{3+} concentration and thus improve the stability of Cu single-site species. The large difference in the Ce^{3+} content between pure support $\text{CeO}_2\text{-3nm}$ and $\text{Cu}_{0.25}\text{CeO}_2\text{-3nm}$ catalyst after adding Cu might be attributed to the direct interaction between Cu species and oxygen vacancy.

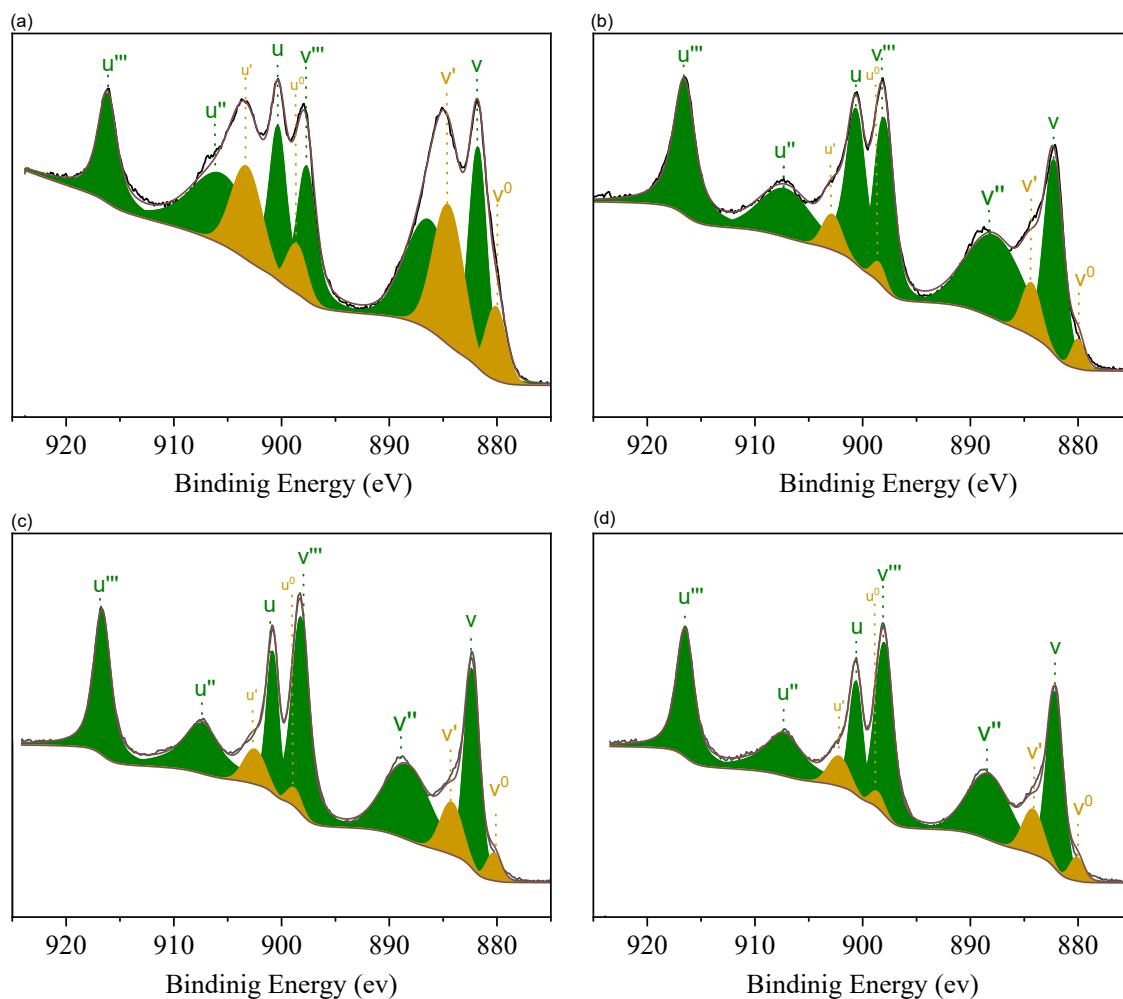


Figure 3.3.8. XPS spectra of Ce 3d for CeO₂-3nm (a), Cu_{0.25}CeO₂-3nm(b), CeO₂-25nm(c), and Cu_{0.25}CeO₂-25nm(d).

Table 3.3.2. XPS deconvolution results of CeO₂-3nm, Cu_{0.25}CeO₂-3nm, CeO₂-25nm and Cu_{0.25}CeO₂-25nm

Sample		CeO ₂ -3nm		Cu _{0.25} CeO ₂ -3nm		CeO ₂ -25nm		Cu _{0.25} CeO ₂ -25nm	
Species	Label	B. E	Ratio of Ce ³⁺ %	B. E	Ratio of Ce ³⁺ %	B. E	Ratio of Ce ³⁺ %	B. E	Ratio of Ce ³⁺ %
Ce ³⁺	v ⁰	880.1	28.5	880.0	9	880.3	12	880.1	11
	u ⁰	898.7		898.6		898.9		898.8	
	v'	884.5		884.3		884.2		884.2	
	u'	903.3		902.9		902.6		902.3	
Ce ⁴⁺	v	881.8	882.2	882.3	882.1				
	u	900.4	900.5	900.8	900.6				
	v''	886.3	887.7	888.3	888.3				
	u''	905.9	907.4	907.3	907.4				
	v'''	897.7	898.0	898.2	898.0				
	u'''	916.2	916.5	916.6	916.5				

B.E. refers to the binding energy.

3.3.5 Conclusions

This section pointed out the significant influence of the crystallite size of CeO₂ supports. Therefore, two catalysts with 0.25 wt% of Cu supported on two different CeO₂ and tested under CO-PROX reaction conditions. XRD and XPS results showed that CeO₂-3nm has a smaller crystallite size and rich oxygen vacancy (evidenced by EPR). Thus, the Cu_{0.25}CeO₂-3nm catalyst was shown to have the best CO₂-selectivity at high temperatures of 125-150 °C compared to the Cu_{0.25}CeO₂-25nm catalyst. Its highest CO₂-selectivity was attributed to the existence high amount of Cu single species in this catalyst as evidenced by EPR. On the other hand, the activation of H₂ over Cu_{0.25}CeO₂-3nm required high temperature as revealed by H₂-TPR, suggesting that Cu²⁺ single species are a lower tendency for activating hydrogen. The high activity of Cu_{0.25}CeO₂-25nm is attributed to high reducibility and high redox properties as provided by H₂-TPR and EPR.

4 General conclusions and Future works

Preferential oxidation of CO is the most efficient and cost-effective technique to produce CO-free hydrogen for fuel cell application. Finding an inexpensive, highly active, highly selective, and stable catalyst is still a major challenge for the CO-PROX reaction. Cu/CeO₂ systems have been known as promising catalysts due to their high catalytic performance and low cost.

Throughout this PhD thesis, specific conclusions are put forward in each of the different sections. As an outline compendium, these main study findings and most significant results can be summarized in general conclusions:

1. This work aims to develop highly active Cu single atoms catalysts for preferential CO oxidation reaction. Therefore, we prepared CuCe/TiO₂ (Ce/TiO₂=0.18) catalyst with a tiny amount of Cu (0.05 wt.%). This catalyst exhibited high activity and CO₂-selectivity compared with the best-known CeO₂-based PROX catalysts. For the stability of this catalyst, there was no deactivation observed after 17 h at 120 °C. The NAP-XPS results of the support did not show any significant redox activity under PROX conditions despite the coexistence of Ti⁴⁺ with Ce⁴⁺ and Ce³⁺ on the surface of the support. This might be the main reason why the bare support displayed negligible activity. In contrast to the support, the Cu catalyst demonstrated a significant and reversible Ce⁴⁺/Ce³⁺ redox shuttle under PROX conditions, whereas the oxidation state of Ti was unchanged. Copper was only detected by EPR as Cu²⁺ which confirmed its predominant single-site nature. Cu species in the bulk of the support are inactive (as evidenced by EPR). From operando EPR, NAP-XPS, and DRIFTS investigations, we could demonstrate that active sites for CO oxidation in the presence of hydrogen are single Cu ions incorporated in the surface of highly dispersed ceria where they shuttle between $-\text{Cu}^{2+}-\text{O}-\text{Ce}^{4+}-$ and $-\text{Cu}^{+}-\square-\text{Ce}^{3+}$ by supplying active oxygen for oxidation of CO to CO₂, which is then refilled by molecular oxygen according to Mars-van Krevelen and/or Langmuir-Hinshelwood mechanisms (i.e., oxidation of CO via oxygen lattice). Cu⁺ species were demonstrated by operando DRIFTS to be preferred sites for the adsorption and the activation of CO molecules.

2. Previously the in-situ and operando spectroscopic investigations showed that Cu single sites on the ceria surface are the active sites. Therefore, to maximize the number of Cu atomic active sites on the surface of Ce, different Cu contents (0.25, 0.5 and 1wt%) were supported on commercially available CeO₂ by mechanochemical reaction (ball-milling). The activity test results showed that the Cu-mass normalized CO oxidation rate significantly increased as Cu content decreased from 1 to 0.25wt%. The Cu-mass normalized CO oxidation rate of the lowest Cu loading (Cu_{0.25}CeO₂) catalyst is five times higher than reported in literature. According to all the results previously shown, it can be suggested that the superior CO-PROX catalytic activity of the Cu_{0.25}CeO₂ catalyst is related to the high dispersion of the Cu²⁺ single sites on the surface associated with the high amount of oxygen vacancies after reduction pretreatment (as evidenced by EPR and NAP-XPS). The higher CO₂-selectivity obtained by Cu_{0.25}CeO₂ catalyst at high temperatures range of 125-150 °C is attributed to the low tendency of Cu single sites to activate hydrogen (provided by H₂-TPR). Interestingly, these catalysts were prepared by a straightforward method (ball-milling). This preparation method does not require organic solvents, templates, acid or base media and much power, making this preparation strategy highly desirable in the industry. Appealingly, there are no changes in CO conversion and CO₂ selectivity resulting from the experiment of 74 h time-on-stream even at 90 °C over all these three catalysts, making them reasonable for practical fuel cell application. Increasing Cu content to 1wt% led to a decrease in the Cu-mass CO oxidation rate of Cu₁CeO₂. This is because higher Cu loadings favour the formation of less active Cu clusters (as evidenced by EPR) because a large part of the Cu sites may be hidden in those clusters and excluded from contact with reactants. Increasing Cu content from 0.5 to 1 wt%, the activity in term of CO conversion of Cu_{0.5}CeO₂ and Cu₁CeO₂ was unchanged. This indicates that the number of active sites in these two catalysts is comparable. By combining various spectroscopic methods, we can show that the direct interactions of Cu single sites with cerium, and oxygen vacancy species are greatly correlated to CO oxidation activity and CO₂-selectivity.
3. The redox properties, oxygen vacancies and reducibility of the supports play an essential role in the catalytic performance of supported copper catalysts. Two Cu (0.25 wt%-Cu) catalysts supported on two different commercial CeO₂ having different crystallite sizes were also prepared by ball-milling. The activity order for these Cu catalysts is Cu_{0.25}CeO₂-25nm < Cu_{0.25}CeO₂-3nm. The high activity of

Cu_{0.25}CeO₂-25nm catalyst is attributed to the redox properties and reducibility of this sample (as evidenced by EPR and H₂-TPR, respectively). Therefore, we can conclude that the redox properties and reducibility of the support are seen as the key factor determining the CO PROX activity. EPR and XPS results showed that the lower crystallite size CeO₂-3nm support is rich in oxygen vacancies compared to bigger crystallite support (CeO₂-25nm). The higher oxygen vacancies in this support led to stabilize the reoxidation of Cu species to Cu²⁺. And therefore, the process of reduction/oxidation in a Cu_{0.25}CeO₂-3nm catalyst is very difficult.

Future works:

1. Despite significant progress has been made on Cu/CeO₂ catalysts, further improvements in the CO PROX over these catalysts are still required to enable the commercialization of these catalysts. The challenge is to design new Cu/CeO₂ catalyst generations that have the ability to achieve full CO conversion at low temperatures without any hydrogen oxidation reaction. Catalysts with a high reducibility, redox-active, oxygen vacancy and high Cu dispersed are required to achieve high catalytic performance. Therefore, further studies have to focus on the synthesis of Cu-single atoms catalysts (SACs) using highly reducible CeO₂. In addition, the oxygen storage and oxygen mobility of CeO₂ are seen to play a very important role in enhancing the reaction rate. It has been shown that the addition of lower valent cations such as Fe²⁺ or Mn²⁺ during the preparation of Cu/CeO₂ catalysts led to creating of materials with higher oxygen mobility and OSC. Therefore, the existence of such cations with redox properties might be an attractive way to enhance the redox cycle of the catalyst.
2. The stability is a significant challenge for CO PROX reaction at low temperatures. The gas mixture obtained from hydrocarbon steam reforming followed by water gas shift reaction usually has 15-25% CO₂ and 10-20% H₂O. Therefore, a long-term stability test under flow of PROX gas mixtures contain both 15-25% CO₂ and 10-20% H₂O are necessary. However, further studies should be done to transfer the developed catalysts on a laboratory scale to practical industry. Thus, further work aims to design an experimental set-up activity test more directly related to catalysts working under industrial conditions.

5 References

- (1) Xiaoding, X.; Moulijn, J. A. *Energy & Fuels.*, **1996**, *10*, 305-325.
- (2) Wójtowicz, M. A.; Pels, J. R.; Moulijn, J. A. *Fuel Process. Technol.*, **1993**, *34*, 1-71.
- (3) Abed, H.; Mosrati, J.; Abdel-Mageed, A. M.; Cisneros, S.; Huyen Vuong, T.; Rockstroh, N.; Bartling, S.; Wohlrab, S.; Brückner, A.; Rabeah, J. *ChemCatChem.* **2022**, 1-8.
- (4) Barbir, F.; Academic press, 2012.
- (5) Gold, L. New catalyst of platinum nanoparticles could lead to stall-free stable fuel cells. 2010.
- (6) Wu, J.; Yuan, X. Z.; Martin, J. J.; Wang, H.; Zhang, J.; Shen, J.; Wu, S.; Merida, W. *J. Power Sources.*, **2008**, *184*, 104-119.
- (7) Santacesaria, E.; Carrá, S. *Appl. Catal.*, **1983**, *5*, 345-358.
- (8) Si, R.; Flytzani-Stephanopoulos, M. *Angew. Chem.*, **2008**, *120*, 2926-2929.
- (9) Trimm, D. L. *Appl. Catal., A.*, **2005**, *296*, 1-11.
- (10) Son, I. H.; Shamsuzzoha, M.; Lane, A. M. *J. Catal.*, **2002**, *210*, 460-465.
- (11) Jiménez, S.; Soler, J.; Valenzuela, R. X.; Daza, L. *J. Power Sources.*, **2005**, *151*, 69-73.
- (12) Schönbrod, B.; Mariño, F.; Baronetti, G.; Laborde, M. *Int. J. Hydrogen Energy.*, **2009**, *34*, 4021-4028.
- (13) Tosti, S. *Int. J. Hydrogen Energy.*, **2010**, *35*, 12650-12659.
- (14) Liu, Q. H.; Liao, L. W.; Zhou, X. H.; Yin, Q. Q. *Adv. Mater. Res.*, **2011**, *236-238*, 829-834.
- (15) Adak, S.; Rabeah, J.; Ranjan, R.; Khan, T. S.; Poddar, M. K.; Gupta, R. K.; Sasaki, T.; Kumar, S.; Bordoloi, A.; Gopinath, C. S.; et al. *Appl. Catal. A* **2021**, 624.
- (16) Arango-Díaz, A.; Cecilia, J. A.; Moretti, E.; Talon, A.; Núñez, P.; Marrero-Jerez, J.; Jiménez-Jiménez, J.; Jiménez-López, A.; Rodríguez-Castellón, E. *Int. J. Hydrogen Energy.*, **2014**, *39*, 4102-4108.
- (17) Arango-Díaz, A.; Moretti, E.; Talon, A.; Storaro, L.; Lenarda, M.; Núñez, P.; Marrero-Jerez, J.; Jiménez-Jiménez, J.; Jiménez-López, A.; Rodríguez-Castellón, E. *Appl. Catal., A.*, **2014**, *477*, 54-63.
- (18) Barbato, P. S.; Colussi, S.; Di Benedetto, A.; Landi, G.; Lisi, L.; Llorca, J.; Trovarelli, A. *Appl. Catal., A.*, **2015**, *506*, 268-277.
- (19) Adhikari, S.; Fernando, S. *Ind. Eng. Chem. Res.*, **2006**, *45*, 875-881.
- (20) Adams, T. M.; Mickalonis, J. *Mater. Lett.*, **2007**, *61*, 817-820.
- (21) Park, E. D.; Lee, D.; Lee, H. C. *Catal. Today.*, **2009**, *139*, 280-290.
- (22) Gases, A. R. o. P. O. o. C. M. i. H. R.
- (23) Choudhary, T. V.; Goodman, D. W. *Catal. Today.*, **2002**, *77*, 65-78.
- (24) Faur Ghenciu, A. *Curr. Opin. Solid State Mater. Sci.*, **2002**, *6*, 389-399.
- (25) Avgouropoulos, G.; Ioannides, T.; Papadopoulou, C.; Batista, J.; Hocevar, S.; Matralis, H. K. *Catalysis Today.*, **2002**, *75*, 157-167.
- (26) Korotkikh, O.; Farrauto, R. *Catal. Today.*, **2000**, *62*, 249-254.
- (27) Kahlich, M. J.; Gasteiger, H. A.; Behm, R. J. *J. Catal.*, **1997**, *171*, 93-105.
- (28) Manasilp, A.; Gulari, E. *Appl. Catal., B.*, **2002**, *37*, 17-25.
- (29) Qiao, B.; Liu, J.; Wang, Y.-G.; Lin, Q.; Liu, X.; Wang, A.; Li, J.; Zhang, T.; Liu, J. *ACS Catalysis.*, **2015**, *5*, 6249-6254.
- (30) Zhang, Y.; Hao, Y.; Meng, L. *Pol. J. Environ. Stud.*, **2022**, *31*, 4965-4973.
- (31) Papavasiliou, J. *Catalysis Today.*, **2020**, *357*, 684-693.
- (32) Carretin, S.; Hao, Y.; Aguilar-Guerrero, V.; Gates, B. C.; Trasobares, S.; Calvino, J. J.; Corma, A. *Chemistry.*, **2007**, *13*, 7771-7779.
- (33) Wörner, A. *Appl. Catal., A.*, **2003**, *245*, 1-14.
- (34) Mariño, F.; Descorme, C.; Duprez, D. *Appl. Catal., B.*, **2004**, *54*, 59-66.
- (35) Liu, Y.; Liu, B.; Liu, Y.; Wang, Q.; Hu, W.; Jing, P.; Liu, L.; Yu, S.; Zhang, J. *Appl. Catal., B.*, **2013**, *142-143*, 615-625.
- (36) Zhu, F.; Zhang, Y.; Gu, X.; Chen, C.; Jin, W.; Ke, X. *Int. J. Hydrogen Energy.*, **2016**, *41*, 13513-13520.
- (37) Cecilia, J. A.; Arango-Díaz, A.; Rico-Pérez, V.; Bueno-López, A.; Rodríguez-Castellón, E. *Catal. Today.*, **2015**, *253*, 115-125.
- (38) Barbato, P. S.; Di Benedetto, A.; Landi, G.; Lisi, L. *Chem. Eng. J.*, **2015**, *279*, 983-993.
- (39) Caputo, T.; Lisi, L.; Pirone, R.; Russo, G. *Appl. Catal., A.*, **2008**, *348*, 42-53.
- (40) Liu, Z.; Zhou, R.; Zheng, X. *J. Nat. Gas Chem.*, **2007**, *16*, 167-172.
- (41) Daniel Gamarra, C. B., Marcos Fernández-García, and Arturo Martínez-Arias. *J. AM. CHEM. SOC.*, **2007**, *129*, 12064-12065.
- (42) Park, J. E.; Park, E. D. *Catal. Lett.*, **2014**, *144*, 607-614.
- (43) Gawade, P.; Bayram, B.; Alexander, A.-M. C.; Ozkan, U. S. *Appl. Catal., B.*, **2012**, *128*, 21-30.
- (44) Mhlaba, R.; Mosuang, T.; Magadzu, T. *Chemistry.*, **2019**, *1*, 164-179.
- (45) Teng, Y.; Sakurai, H.; Ueda, A.; Kobayashi, T. *Int. J. Hydrogen Energy.*, **1999**, *24*, 355-358.
- (46) Omata, K.; Takada, T.; Kasahara, S.; Yamada, M. *Appl. Catal., A.*, **1996**, *146*, 255-267.

- (47) Elias, J. S.; Artrith, N.; Bugnet, M.; Giordano, L.; Botton, G. A.; Kolpak, A. M.; Shao-Horn, Y. *ACS Catalysis* **2016**, *6*, 1675-1679.
- (48) Du, Q.; Cheng, X.; Tahir, M. H.; Su, D.; Wang, Z.; Chen, S. *Int. J. Hydrogen Energy*, **2020**, *45*, 16469-16481.
- (49) Konsolakis, M. *Appl. Catal., B*, **2016**, *198*, 49-66.
- (50) Si, R.; Raitano, J.; Yi, N.; Zhang, L.; Chan, S.-W.; Flytzani-Stephanopoulos, M. *Catal. Today*, **2012**, *180*, 68-80.
- (51) Abed, H.; Mosrati, J.; Abdel-Mageed, A. M.; Cisneros, S.; Vuong, T. H.; Rockstroh, N.; Bartling, S.; Wohlrab, S.; Brückner, A.; Rabeah, J. *ChemCatChem* **2022**.
- (52) Wu, Z.; Zhu, H.; Qin, Z.; Wang, H.; Huang, L.; Wang, J. *Appl. Catal., B*, **2010**, *98*, 204-212.
- (53) Alencar, C. S. L.; Paiva, A. R. N.; Silva, J. C. M. d.; Vaz, J. M.; Spinacé, E. V. *Mater. Res.*, **2020**, *23*.
- (54) Davó-Quiñonero, A.; Bailón-García, E.; López-Rodríguez, S.; Juan-Juan, J.; Lozano-Castelló, D.; García-Melchor, M.; Herrera, F. C.; Pellegrin, E.; Escudero, C.; Bueno-López, A. *ACS Catalysis*, **2020**, *10*, 6532-6545.
- (55) Mosrati, J.; Abdel-Mageed, A. M.; Vuong, T. H.; Grauke, R.; Bartling, S.; Rockstroh, N.; Atia, H.; Armbruster, U.; Wohlrab, S.; Rabeah, J.; et al. *ACS Catal* **2021**, *11*, 10933-10949.
- (56) Fang, Y.; Chi, X.; Li, L.; Yang, J.; Liu, S.; Lu, X.; Xiao, W.; Wang, L.; Luo, Z.; Yang, W.; et al. *ACS Appl. Mater. Interfaces*, **2020**, *12*, 7091-7101.
- (57) Lu, J.; Wang, J.; Zou, Q.; He, D.; Zhang, L.; Xu, Z.; He, S.; Luo, Y. *ACS Catal* **2019**, *9*, 2177-2195.
- (58) Vuong, T. H.; Radnik, J.; Rabeah, J.; Bentrup, U.; Schneider, M.; Atia, H.; Armbruster, U.; Grünert, W.; Brückner, A. *ACS Catalysis*, **2017**, *7*, 1693-1705.
- (59) Chang, K.; Wang, T.; Chen, J. G. *Appl. Catal., B*, **2017**, *206*, 704-711.
- (60) Chen, C.-S.; Chen, T.-C.; Wu, H.-C.; Wu, J.-H.; Lee, J.-F. *Catal. Sci. Technol.*, **2020**, *10*, 4271-4281.
- (61) Chen, Y.-Z.; Liaw, B.-J.; Huang, C.-W. *Appl. Catal., A*, **2006**, *302*, 168-176.
- (62) Chen, Y.-Z.; Liaw, B.-J.; Chen, H.-C. *Int. J. Hydrogen Energy*, **2006**, *31*, 427-435.
- (63) Chen, Y.-Z.; Liaw, B.-J.; Chang, W.-C.; Huang, C.-T. *Int. J. Hydrogen Energy*, **2007**, *32*, 4550-4558.
- (64) Ratnasamy, P.; Srinivas, D.; Satyanarayana, C.; Manikandan, P.; Kumaran, R. S.; Sachin, M.; Shetti, V. N. *J. Catal.*, **2004**, *221*, 455-465.
- (65) Maela, M.; Roberta, D. M.; Flora, B.; Salvatore, C.; Jan, K. *Appl. Catal., B*, **2005**, *61*, 192-205.
- (66) Caputo, T.; Pirone, R.; Russo, G. *Kinet. Catal.*, **2006**, *47*, 756-764.
- (67) Firsova, A.; Il'ichev, A.; Khomenko, T.; Gorobinskii, L.; Maksimov, Y. V.; Suzdalev, I.; Korchak, V. *Kinet. Catal.*, **2007**, *48*.
- (68) Avgouropoulos, G.; Ioannides, T.; Matralis, H. *Appl. Catal., B*, **2005**, *56*, 87-93.
- (69) Severino, F.; Brito, J. L.; Laine, J.; Fierro, J. L. G.; Agudo, A. L. *J. Catal.* **1998**, *177*, 82-95.
- (70) VANNICE, K. I. C. A. M. A. *J. Catal.* **1991**, *131*, 22-35
- (71) K. Nagase, Y. Z., Y. Kodama, and J. Kakuta. *J. Catal.* **1999**, *187*, 123-130.
- (72) G.G. Jernigan, G. A. S. *J. Catal.* **1994**, *147*, 567-577.
- (73) Yao, S.; Mudiyansele, K.; Xu, W.; Johnston-Peck, A. C.; Hanson, J. C.; Wu, T.; Stacchiola, D.; Rodriguez, J. A.; Zhao, H.; Beyer, K. A.; et al. *ACS Catalysis* **2014**, *4*, 1650-1661.
- (74) Yao, S.; Mudiyansele, K.; Xu, W.; Johnston-Peck, A. C.; Hanson, J. C.; Wu, T.; Stacchiola, D.; Rodriguez, J. A.; Zhao, H.; Beyer, K. A.; et al. *ACS Catalysis*, **2014**, *4*, 1650-1661.
- (75) Fang, Y.; Chi, X.; Li, L.; Yang, J.; Liu, S.; Lu, X.; Xiao, W.; Wang, L.; Luo, Z.; Yang, W.; et al. *ACS Appl. Mater. Interfaces*. **2020**, *12*, 7091-7101, 10.1021/acsami.9b18264.
- (76) Eren, B.; Heine, C.; Bluhm, H.; Somorjai, G. A.; Salmeron, M. *J. Am. Chem. Soc.* **2015**, *137*, 11186-11190.
- (77) Zhang, R.; Miller, J. T.; Baertsch, C. D. *J. Catal* **2012**, *294*, 69-78.
- (78) Jia, A.-P.; Hu, G.-S.; Meng, L.; Xie, Y.-L.; Lu, J.-Q.; Luo, M.-F. *J. Catal.*, **2012**, *289*, 199-209.
- (79) Elias, J. S.; Artrith, N.; Bugnet, M.; Giordano, L.; Botton, G. A.; Kolpak, A. M.; Shao-Horn, Y. *ACS Catal.* **2016**, *6*, 1675-1679.
- (80) Gamarra, D.; Munuera, G.; Hungria, A. B.; Fernández-García, M.; Conesa, J. C.; Midgley, P. A.; Wang, X. Q.; Hanson, J. C.; Rodríguez, J. A.; Martínez-Arias, A. *J. Phys. Chem. C*, **2007**, *111*, 11026-11038.
- (81) Elias, J. S.; Risch, M.; Giordano, L.; Mansour, A. N.; Shao-Horn, Y. *J. Am. Chem. Soc.*, **2014**, *136*, 17193-17200.
- (82) Wang, F.; Büchel, R.; Savitsky, A.; Zalibera, M.; Widmann, D.; Pratsinis, S. E.; Lubitz, W.; Schüth, F. *ACS Catal.* **2016**, *6*, 3520-3530.
- (83) Kydd, R.; Teoh, W. Y.; Wong, K.; Wang, Y.; Scott, J.; Zeng, Q.-H.; Yu, A.-B.; Zou, J.; Amal, R. *Adv. Funct. Mater.* **2009**, *19*, 369-377.
- (84) Abdel-Mageed, A. M.; Rungtaweeworanit, B.; Parlinska-Wojtan, M.; Pei, X.; Yaghi, O. M.; Behm, R. J. *J. Am. Chem. Soc.*, **2019**, *141*, 5201-5210.
- (85) Konsolakis, M.; Lykaki, M. *Catalysts*, **2020**, *10*, 160.
- (86) Wang, J.; Pu, H.; Wan, G.; Chen, K.; Lu, J.; Lei, Y.; Zhong, L.; He, S.; Han, C.; Luo, Y. *Int. J. Hydrogen Energy*, **2017**, *42*, 21955-21968.
- (87) Wang, F.; Büchel, R.; Savitsky, A.; Zalibera, M.; Widmann, D.; Pratsinis, S. E.; Lubitz, W.; Schüth, F. *ACS Catalysis*, **2016**, *6*, 3520-3530.
- (88) Mosrati, J.; Abdel-Mageed, A. M.; Vuong, T. H.; Grauke, R.; Bartling, S.; Rockstroh, N.; Atia, H.; Armbruster, U.; Wohlrab, S.; Rabeah, J.; et al. *ACS Catal.* **2021**, *11*, 10933-10949.
- (89) Ji, S.; Chen, Y.; Wang, X.; Zhang, Z.; Wang, D.; Li, Y. *Chem. Rev.*, **2020**, *120*, 11900-11955.

- (90) Liu, W.; Flytzanistephanopoulos, M. *J. Catal.* **1995**, *153*, 317-332.
- (91) Lopez, I.; Valdes-Solis, T.; Marban, G. *Int. J. Hydrog. Energy*. **2008**, *33*, 197-205.
- (92) Hou, X.; Jones, B. T. Inductively coupled plasma/optical emission spectrometry. John Wiley & Sons Chichester, UK: 2000; Vol. 2000, pp 9468-9485.
- (93) Birkholz, M.; John Wiley & Sons, 2006.
- (94) Ross, J. R.; Elsevier, 2011.
- (95) Liu, P.-z.; Hao, B.; Zhang, H.-x.; Xu, B.-s.; Guo, J.-j. *New Carbon Materials.*, **2021**, *36*, 497-511.
- (96) Palmer, L.; Jackson, J. W.; PIERCE, W. O. B. *Nature.*, **1928**, *121*, 501-501.
- (97) Israel E. Wachs, M. A. B.;
- (98) instrument., E. What is Raman Spectroscopy? 2020; Vol. 2023.
- (99) Ryczkowski, J. *Catal. Today.*, **2001**, *68*, 263-381.
- (100) Ruz, S. G. Activity, in situ IR and EXAFS spectroscopy studies, and monte carlo simulation of the preferential oxidation of carbon monoxide on Nb-promoted Pt/Al₂O₃ catalysts and Pt-free oxides catalysts University of Notre Dame, 2007.
- (101) Aboukaïs, A.; Bennani, A.; Lamonier-Dulongpont, C.; Abi-Aad, E.; Wrobel, G. *Colloids Surf., A.*, **1996**, *115*, 171-177.
- (102) Fujiwara, S.; Katsumata, S.; Seki, T. *J. Phys. Chem.*, **1967**, *71*, 115-120.
- (103) Stevie, F. A.; Donley, C. L. *J. Vac. Sci. Technol., A.*, **2020**, *38*.
- (104) Marbán, G.; Fuertes, A. B. *Appl. Catal. B.* **2005**, *57*, 43-53.
- (105) Zou, Q.; Zhao, Y.; Jin, X.; Fang, J.; Li, D.; Li, K.; Lu, J.; Luo, Y. *Appl. Surf. Sci.*, **2019**, *494*, 1166-1176.
- (106) Wang, W.-W.; Du, P.-P.; Zou, S.-H.; He, H.-Y.; Wang, R.-X.; Jin, Z.; Shi, S.; Huang, Y.-Y.; Si, R.; Song, Q.-S.; et al. *ACS Catal* **2015**, *5*, 2088-2099.
- (107) Ratnasamy, P.; Srinivas, D.; Satyanarayana, C. V. V.; Manikandan, P.; Kumaran, R. S. S.; Sachin, M.; Shetti, V. N. *J. Catal.* **2004**, *221*, 455-465.
- (108) Bae, C. M.; Ko, J. B.; Kim, D. H. *Catal. Commun.* **2005**, *6*, 507-511.
- (109) Polster, C. S.; Nair, H.; Baertsch, C. D. *J. Catal.* **2009**, *266*, 308-319.
- (110) Thommes, M.; Kaneko, K.; Neimark, A. V.; Olivier, J. P.; Rodriguez-Reinoso, F.; Rouquerol, J.; Sing, K. S. W. *Pure Appl. Chem.*, **2015**, *87*, 1051-1069.
- (111) Reddy, B. M.; Reddy, G. K.; Ganesh, I.; Ferreira, J. M. F. *J. Mater. Sci.* **2009**, *44*, 2743-2751.
- (112) Reddy, B. M.; Khan, A.; Yamada, Y.; Kobayashi, T.; Lorient, S.; Volta, J. C. *J. Phys. Chem. B.*, **2003**, *107*, 5162-5167.
- (113) Zhang, Y.; Bals, S.; Van Tendeloo, G. *Part. Part. Syst. Char.* **2019**, *36*, 1800287-1800319.
- (114) Bezkrvnyi, O. S.; Blaumeiser, D.; Vorokhta, M.; Kraszkiewicz, P.; Pawlyta, M.; Bauer, T.; Libuda, J.; Kepinski, L. *J. Phys. Chem. C.*, **2020**, *124*, 5647-5656, 10.1021/acs.jpcc.9b10142.
- (115) Bêche, E.; Charvin, P.; Perarnau, D.; Abanades, S.; Flamant, G. *Surf. Inter. Anal* **2008**, *40*, 264-267.
- (116) Watanabe, S.; Ma, X. L.; Song, C. S. *J. Phys. Chem. C.* **2009**, *113*, 14249-14257.
- (117) Li, S.; Zhu, H.; Qin, Z.; Wang, G.; Zhang, Y.; Wu, Z.; Li, Z.; Chen, G.; Dong, W.; Wu, Z.; et al. *Appl. Catal. B.* **2014**, *144*, 498-506.
- (118) Fang, J.; Bi, X.; Si, D.; Jiang, Z.; Huang, W. *Appl. Surf. Sci.*, **2007**, *253*, 8952-8961.
- (119) Liu, Y.; Wen, C.; Guo, Y.; Liu, X.; Ren, J.; Lu, G.; Wang, Y. *ChemCatChem* **2010**, *2*, 336-341.
- (120) Murugan, B.; Ramaswamy, A. V. *J. Am. Chem. Soc.*, **2007**, *129*, 3062-3063.
- (121) Abi-Aad, E.; Bennani, A.; Bonnelle, J.-P.; Aboukaïs, A. *J. Chem. Soc., Faraday Trans.*, **1995**, *91*, 99-104.
- (122) Martinez-Arias, A.; Cataluna, R.; Conesa, J. C.; Soria, J. *J. Phys. Chem. B.*, **1998**, *102*, 809-817, 10.1021/JP972097Q.
- (123) Kais, A. A.; Bennani, A.; Aissi, C. F.; Wrobel, G.; Guelton, M. *J. Chem. Soc. Faraday trans.* **1992**, *88*, 1321-1325.
- (124) Chen, J.; Zhan, Y.; Zhu, J.; Chen, C.; Lin, X.; Zheng, Q. *Appl. Catal. A.* **2010**, *377*, 121-127.
- (125) Conesa, J.; Soria, J. *J. Phys. Chem.*, **1978**, *82*, 1847-1850.
- (126) Conesa, J. C.; Soria, J. *J. Phys. Chem.* **1978**, *82*, 1847-1850.
- (127) Lide, D. R.; Frederikse, H. P. R.; Boca Raton (Fla.) : CRC press, 1997.
- (128) Senanayake, S. D.; Pappoe, N. A.; Nguyen-Phan, T.-D.; Luo, S.; Li, Y.; Xu, W.; Liu, Z.; Mudiyansele, K.; Johnston-Peck, A. C.; Frenkel, A. I.; et al. *Surf. Sci* **2016**, *652*, 206-212.
- (129) Cheng, N.; Zhang, L.; Doyle-Davis, K.; Sun, X. *Electrochem. Energy Rev.*, **2019**, *2*, 539-573.
- (130) Fang, Y.; Chi, X.; Li, L.; Yang, J.; Liu, S.; Lu, X.; Xiao, W.; Wang, L.; Luo, Z.; Yang, W.; et al. *ACS Appl. Mater. Interfaces.* **2020**, *12*, 7091-7101.
- (131) Li, C.; Yang, Y.; Ren, W.; Wang, J.; Zhu, T.; Xu, W. *Catalysis Letters.*, **2020**, *150*, 2045-2055.
- (132) Zhu, J.; Su, Y.; Chai, J.; Muravev, V.; Kosinov, N.; Hensen, E. J. M. *ACS Catal.* **2020**, *10*, 11532-11544.
- (133) Chen, C.-S.; Chen, T.-C.; Wu, H.-C.; Wu, J.-H.; Lee, J.-F. *Catal. Sci. Technol.* **2020**, *10*, 4271-4281, 10.1039/d0cy00792g.
- (134) Shan, W.; Liu, F.; He, H.; Shi, X.; Zhang, C. *Catal. Today.*, **2012**, *184*, 160-165.
- (135) Wang, W.-W.; Yu, W.-Z.; Du, P.-P.; Xu, H.; Jin, Z.; Si, R.; Ma, C.; Shi, S.; Jia, C.-J.; Yan, C.-H. *ACS Catalysis* **2017**, *7*, 1313-1329.
- (136) Lykaki, M.; Pachatouridou, E.; Carabineiro, S. A. C.; Iliopoulou, E.; Andriopoulou, C.; Kallithrakas-Kontos, N.; Boghosian, S.; Konsolakis, M. *Appl. Catal., B* **2018**, *230*, 18-28.

- (137) Li, Y.; Cai, Y.; Xing, X.; Chen, N.; Deng, D.; Wang, Y. *Anal. Methods.*, **2015**, *7*, 3238-3245.
- (138) Ning, J.; Zhou, Y.; Chen, A.; Li, Y.; Miao, S.; Shen, W. *Catal. Today.*, **2020**, *357*, 460-467.
- (139) García-Vargas, C. E.; Collinge, G.; Yun, D.; Lee, M.-S.; Muravev, V.; Su, Y.-Q.; Pereira-Hernández, X. I.; Jiang, D.; Glezakou, V.-A.; Hensen, E. J. M.; et al. *ACS Catalysis* **2022**, *12*, 13649-13662.
- (140) Luo, M.; Ma, J.; Lu, J.; Song, Y.; Wang, Y. **2007**, *246*, 52-59.
- (141) Lj. Kundakovic, M. F.-S. *Appl. Catal., A.*, **1998**, *171*, 13-29.
- (142) Tang, X.; Zhang, B.; Li, Y.; Xu, Y.; Xin, Q.; Shen, W. *Appl. Catal., A* **2005**, *288*, 116-125.
- (143) Zimmer, P.; Tschöpe, A.; Birringer, R. *J. Catal* **2002**, *205*, 339-345.
- (144) Shang, H.; Zhang, X.; Xu, J.; Han, Y. *Front. Chem. Sci. Eng.*, **2017**, *11*, 603-612.
- (145) Hadjiivanov, K.; Knözinger, H. *Phys. Chem. Chem. Phys* **2001**, *3*, 1132-1137.
- (146) Hadjiivanov, K.; Knözinger, H. *J. Catal* **2000**, *191*, 480-485.
- (147) Martínez-Arias, A.; Cataluña, R.; Conesa, J. C.; Soria, J. *J. Phys. Chem. B* **1998**, *102*, 809-817.
- (148) Rakhmatullin, R. M.; Semashko, V. V.; Korableva, S. L.; Kiiamov, A. G.; Rodionov, A. A.; Tschaggelar, R.; van Bokhoven, J. A.; Paun, C. *Mater. Chem. Phys.* **2018**, *219*, 251-257.
- (149) Rabeah, J.; Stosser, R.; Jiao, H.; Troyanov, S. I.; Radnik, J.; Dwelk, H.; Meisel, M.; Bruckner, A. *Chemistry* **2012**, *18*, 6433-6436.
- (150) Hathaway, B. J.; Billing, D. E. *Coord. Chem. Rev.* **1970**, *5*, 143-207.
- (151) A. Martínez-Arias, M. F. a.-G. 1., J. Soria, and J. C. Conesa. *J. Catal* **1999**, *182*, 367-377.
- (152) Abed, H.; Mosrati, J.; Abdel-Mageed, A. M.; Cisneros, S.; Huyen Vuong, T.; Rockstroh, N.; Bartling, S.; Wohlrab, S.; Brückner, A.; Rabeah, J. *ChemCatChem* **2022**, 1-8.
- (153) Mosrati, J.; Abdel-Mageed, A. M.; Vuong, T. H.; Grauke, R.; Bartling, S.; Rockstroh, N.; Atia, H.; Armbruster, U.; Wohlrab, S.; Rabeah, J.; et al. *ACS Catal.* **2021**, *11*, 10933-10949.
- (154) Martínez-Arias, A.; Hungria, A.; Fernández-García, M.; Conesa, J.; Munuera, G. *J. Phys. Chem. B* **2004**, *108*, 17983-17991.
- (155) Martínez-Arias, A.; Hungria, A. B.; Munuera, G.; Gamarra, D. *Appl. Catal. B* **2006**, *65*, 207-216.
- (156) Lenzion-Bielun, Z.; Bettahar, M. M.; Monteverdi, S. *Catal. Commun.*, **2010**, *11*, 1137-1142.
- (157) Abdel-Mageed, A. M.; Cisneros, S.; Mosrati, J.; Atia, H.; Vuong, T. H.; Rockstroh, N.; Wohlrab, S.; Brückner, A.; Rabeah, J. *ChemCatChem.*, **2023**, 1-10.
- (158) Zhang, X.; Li, G.; Tian, R.; Feng, W.; Wen, L. *J. Alloys Compd.*, **2020**, 826.
- (159) Martínez-Arias, A.; Cataluña, R.; Conesa, J. C.; Soria, J. *J. Phys. Chem. B.*, **1998**, *102*, 809-817.
- (160) Rakhmatullin, R. M.; Semashko, V. V.; Korableva, S. L.; Kiiamov, A. G.; Rodionov, A. A.; Tschaggelar, R.; van Bokhoven, J. A.; Paun, C. *Mater. Chem. Phys* **2018**, *219*, 251-257.
- (161) Paier, J.; Penschke, C.; Sauer, J. *Chem. Rev.*, **2013**, *113*, 3949-3985.
- (162) Jie, W.; Liu, Y.; Deng, W.; Liu, Q.; Qiu, M.; Liu, S.; Hu, J.; Gong, L. *J. Solid State Chem.*, **2022**, *311*, 123109.
- (163) Qiu, Z.; Guo, X.; Mao, J.; Zhou, R. *J. Phys. Chem. C.*, **2021**, *125*, 9178-9189.
- (164) Chen, F.-q.; Xia, Y.; Lao, J.-z.; Cheng, D.-g.; Zhan, X.-l. *Ind. Eng. Chem. Res.*, **2021**, *60*, 9068-9079.
- (165) Gong, L.; Liu, C.; Liu, Q.; Dai, R.; Nie, X.; Lu, L.; Liu, G.; Hu, X. *Catal. Surv. Asia.*, **2019**, *23*, 1-9.
- (166) Davó-Quñonero, A.; Navlani-García, M.; Lozano-Castelló, D.; Bueno-López, A.; Anderson, J. A. *ACS Catalysis* **2016**, *6*, 1723-1731.
- (167) Scirè, S.; Crisafulli, C.; Riccobene, P. M.; Patanè, G.; Pistone, A. *Appl. Catal., A.*, **2012**, *417-418*, 66-75.
- (168) Jin, H.; You, R.; Zhou, S.; Ma, K.; Meng, M.; Zheng, L.; Zhang, J.; Hu, T. *Int. J. Hydrogen Energy.*, **2015**, *40*, 3919-3931.

6 Appendix

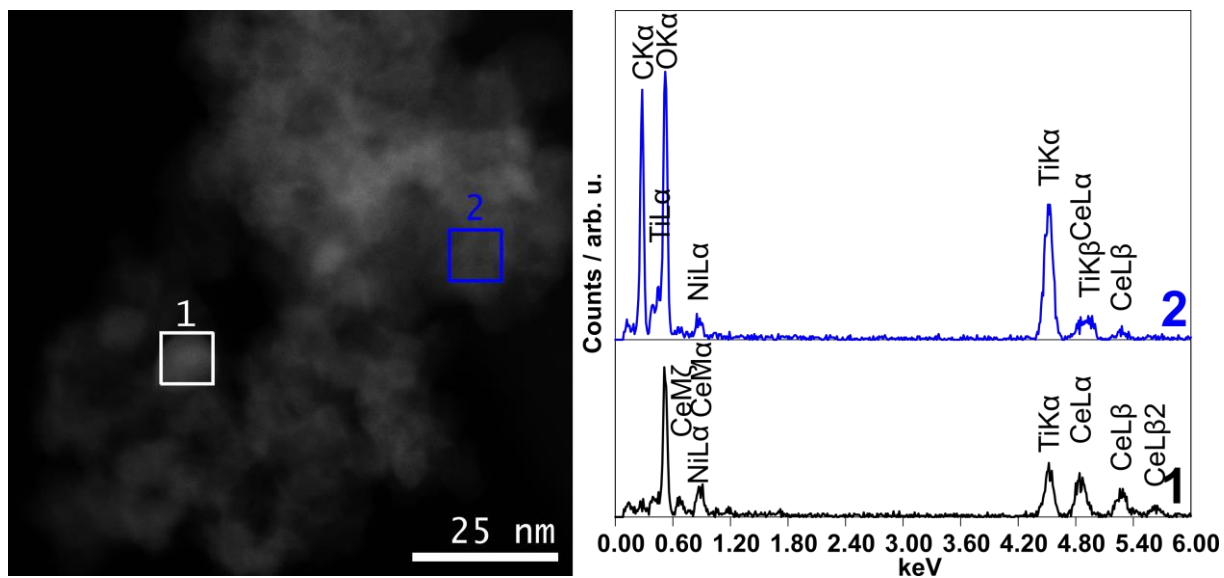


Figure A.1. Complementary to the EDS map shown in Figure 4.1. in the main manuscript, selected ED spectra of the marked areas of the Cu catalyst (STEM-HAADF image on the left) are shown on the right. The share of CeO₂ in area 1 is much higher than in area 2, where much more TiO₂ and only a small amount of CeOx is present.

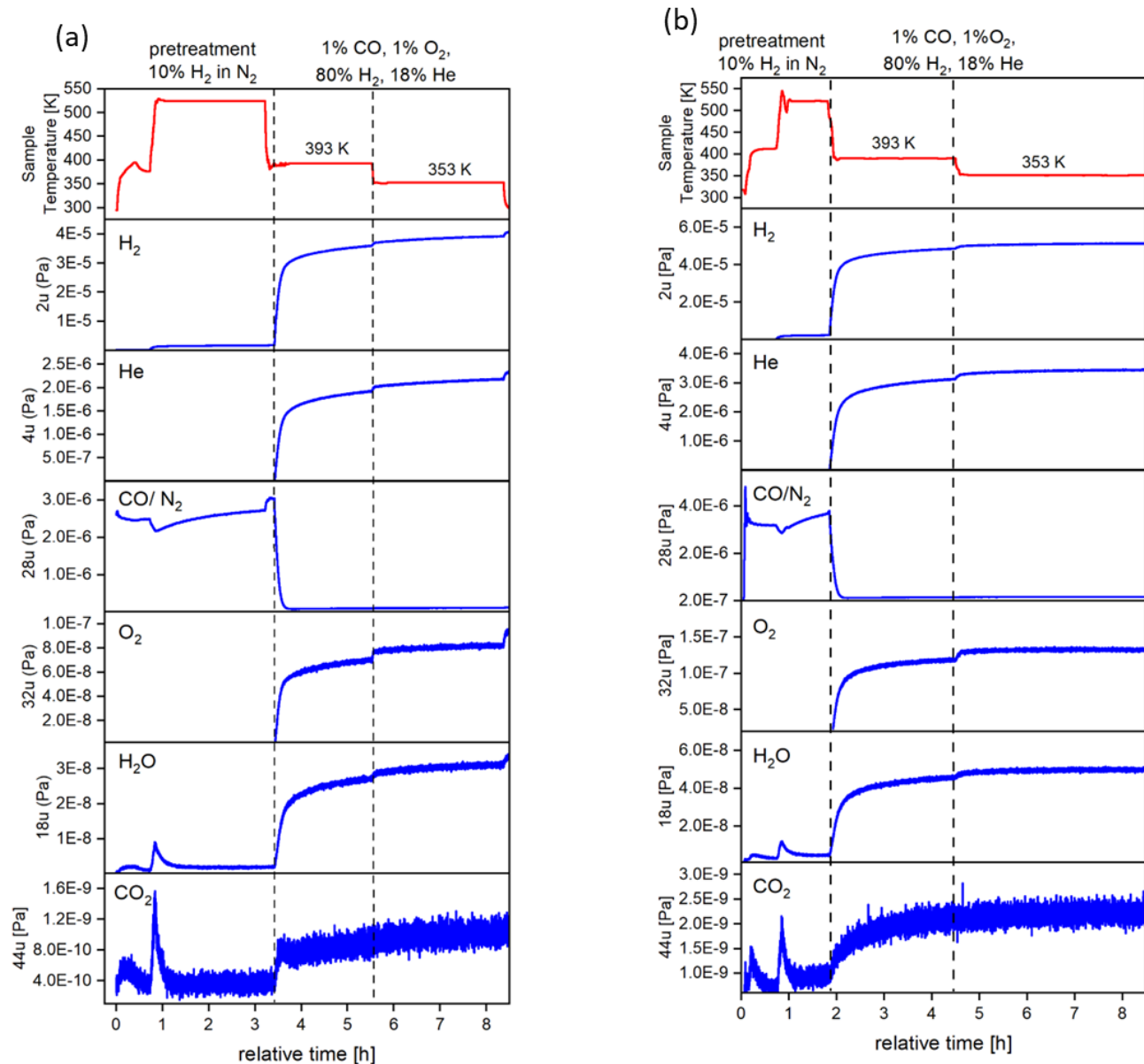


Figure A.2. Quadrupole mass spectroscopy data taken during the NAP-XPS experiment for pure support (a) and (b) copper catalyst over time at different temperatures. After a pretreatment at 250 °C in 10% H₂ the sample was cooled down to 120 °C and the reaction mixture was applied at a total pressure of 2 mbar. Thereafter the temperature was lowered to 80 °C.

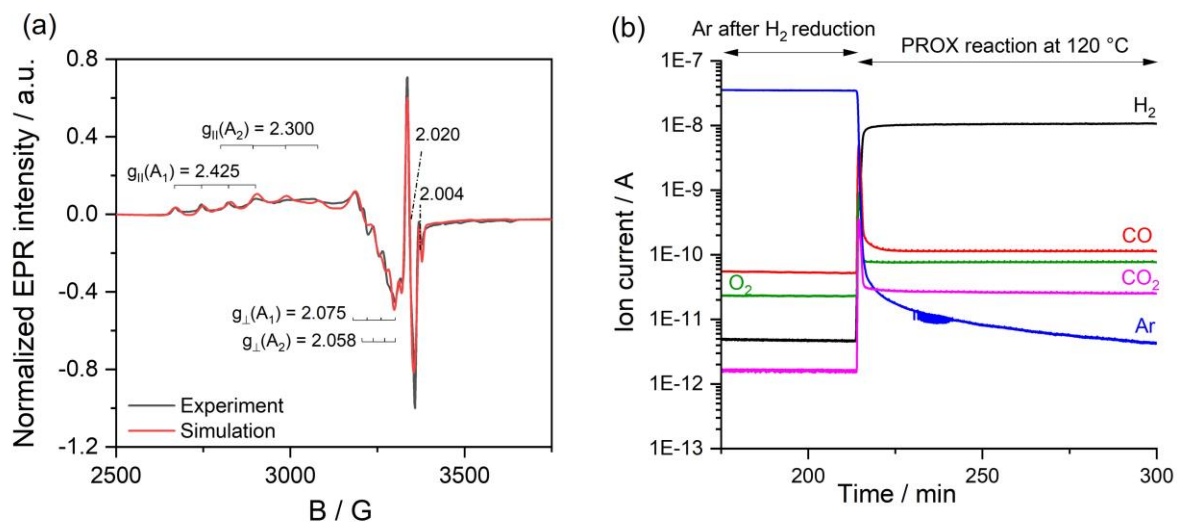


Figure A.3. (a) Normalized EPR spectra recorded at $-180\text{ }^{\circ}\text{C}$ and simulated spectra of the fresh calcined Cu-containing catalyst, (b) Quadrupole mass spectroscopy data taken during operando EPR for Cu-containing catalyst over time after a pretreatment at $250\text{ }^{\circ}\text{C}$ in 10% H₂ and cooling down to $120\text{ }^{\circ}\text{C}$ and during the PROX reaction.

Table A.1. Specific rates of CuCeO₂ catalysts compared with the most active supported Cu catalysts reported in literature.

Samples	Cu Wt%	Catalyst preparation	Reaction conditions	Temperature / °C	Rate CO * μmol g _{cu} ⁻¹ . s ⁻¹	Sco ₂ %	Ref
Cu _{0.25} CeO ₂ Cu _{0.5} CeO ₂ Cu ₁ CeO ₂	0.25 0.5 1	Ball-milling	1% CO, 2% O ₂ , 80% H ₂ / He	60	196 121 70	100 (50-100) °C	This work
CuCeTiO ₂	0.05	Sol-gel	1% CO, 1% O ₂ , 80% H ₂ /	60	21	100 (60-100) °C	³
CuCeO ₂	5	Impregnation	1.5%CO, 1.5% O ₂ , 50 % H ₂ / He	60	57.99	100 (50-100) °C	¹⁶²
CuCeO ₂	2	coprecipitation	1.5%CO, 1.5%O ₂ , 50 % H ₂ / He	60	111.5	100 (40-60) °C	¹⁶³
CuCeO ₂	10	freeze-dried	1% CO, 1% O ₂ , 50 % H ₂ / He	60	4	100 (50-80) °C	¹⁶⁴
CuCeO ₂	5	Impregnation	2% CO, 2% O ₂ 30% H ₂ / N ₂	75	39.66	100 (50-100) °C	⁵⁴
CuCeMnO ₂	8	Impregnation	1.5% CO, 1.5% O ₂ , 47% H ₂ / N ₂	60	29.28	92 (120) °C	¹⁶⁵
CuCeO ₂ CuFeCeO ₂	10	Solvent-free combustion	1% CO, 1% O ₂ , 50% H ₂ / He	60	1.98 5.95	100 (50-80) °C 100 (50-80) °C	⁵⁷
CuCeO ₂	5	Deposition- precipitation	1% CO, 1% O ₂ , 50% H ₂ / He	60	19.12	100 (60-120) °C	¹⁰⁵
CuCeO ₂	7.5	Solvent-free combustion	1% CO, 1% O ₂ , 50% H ₂ / He	60	4.49	100 (80) °C	⁸⁶
CuCe _{0.8} Zr _{0.2} O ₂	5	Impregnation	2% CO, 2% O ₂ , 30% H ₂ / He	75	31.73	95 ≤ (125) °C	¹⁶⁶
CuCeO ₂ CuCeO ₂	5 10	Deposition- precipitation	1%CO, 1% O ₂ 50% H ₂ / N ₂	60	10.41 13.38	100 (80–110) °C	¹⁰⁶
CuCeO ₂ CuCeO ₂	5 5	Deposition– precipitation Co-precipitation	1%CO, 1% O ₂ , 98% H ₂	70	9.5 14	100 (70–100) °C 100 (70–90) °C	¹⁶⁷
CuMnCeO ₂	7.30	Co-precipitation	1% CO, 1% O ₂ , 50% H ₂ / N ₂	60	5.7	100 (60-120) °C	¹⁶⁸

*CO oxidation rates was calculated on the basis CO conversion in the range (20 %≤) using Eq. A1:

$$\text{Reaction Rate} = \frac{X_{\text{CO}} \times n_{\text{CO,in}}}{m_{\text{Cu}}} \quad \text{A1}$$

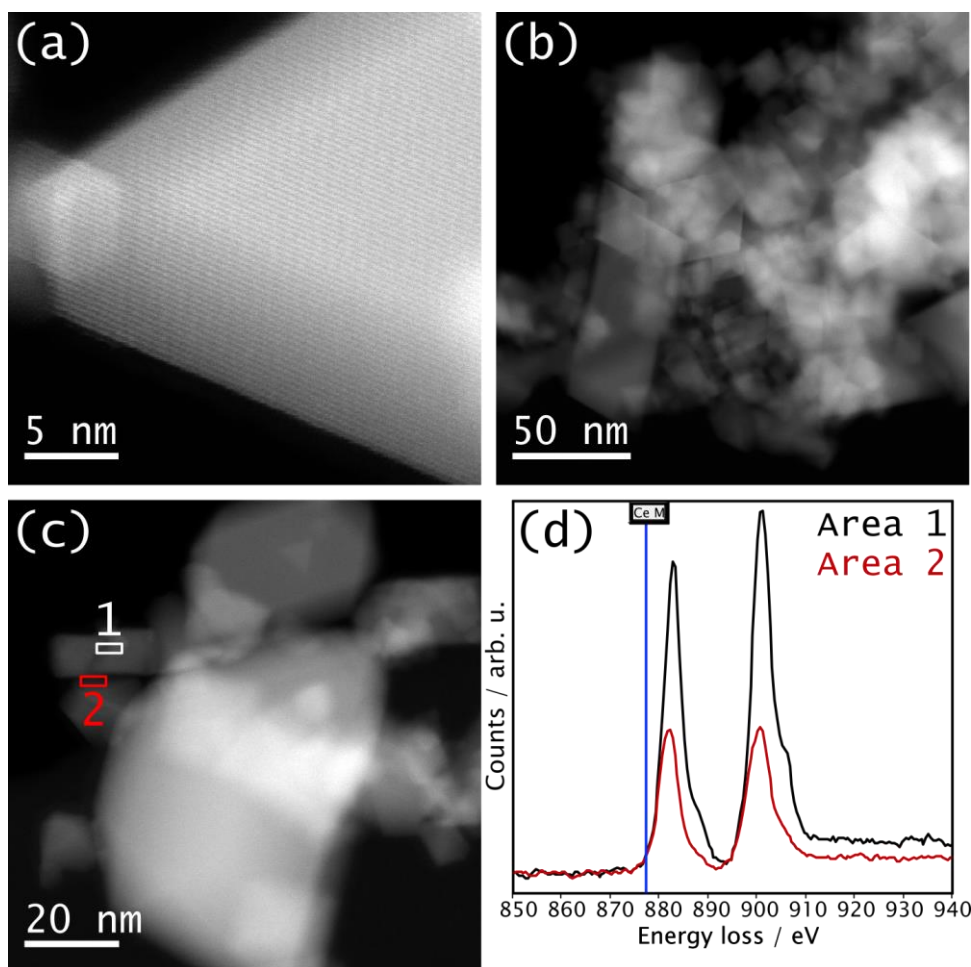


Figure A.4. (a, b) Selected HAADF-STEM images of the support (CeO_2). The electron energy loss EEL spectra (d) taken at the positions 1 and 2 marked in the STEM-ADF image in (c) show the presence of Ce in the oxidation state Ce^{4+} (spectrum 1) and Ce^{3+} (spectrum 2).

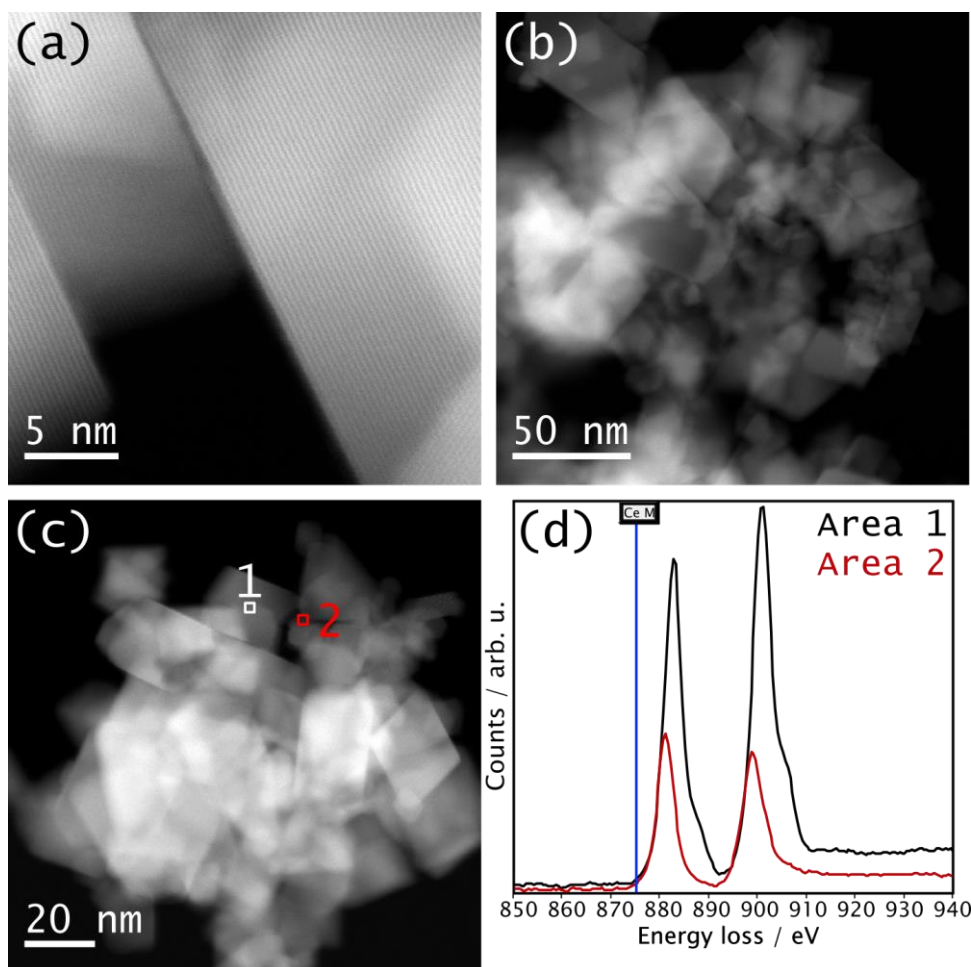


Figure A.5. (a, b) Selected HAADF-STEM images of $\text{Cu}_{0.5}\text{CeO}_2$ catalyst. The images (a-b) are very similar to those of the support. Because Ce is heavier than Cu, it is brighter in the HAADF images and thus, copper is not visible in these images. Electron energy loss (EEL) spectra (d) were taken at the positions highlighted in the STEM-ADF image (c). Like in $\text{Cu}_{0.25}\text{CeO}_2$, Ce^{4+} (spectrum 1) and Ce^{3+} (spectrum 2) are visible.

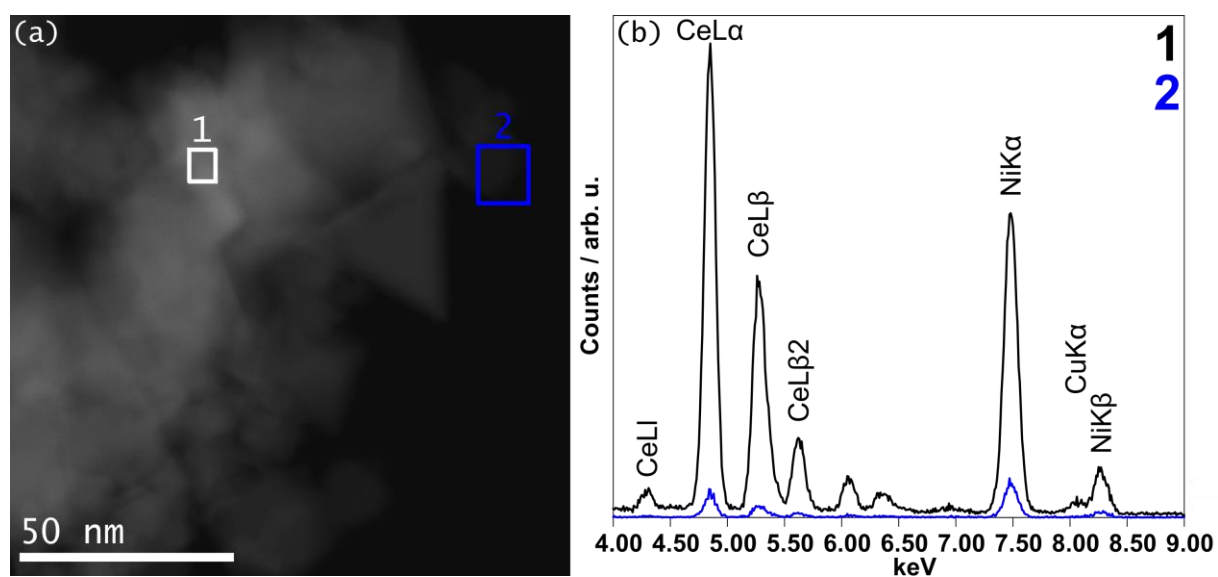


Figure A.6. Selected EDX spectra of the marked areas in the STEM-HAADF image of $\text{Cu}_{0.5}\text{CeO}_2$ (a) are shown in (b). Even though the Ce signal is very prominent in area 1, also the minor peak of Cu $\text{K}\alpha$ can be seen, which is proving the presence of Cu in this material. Spectrum 2 is taken at a position of smaller sample thickness (and thus lower amount of all constituents) so that no Cu could be observed

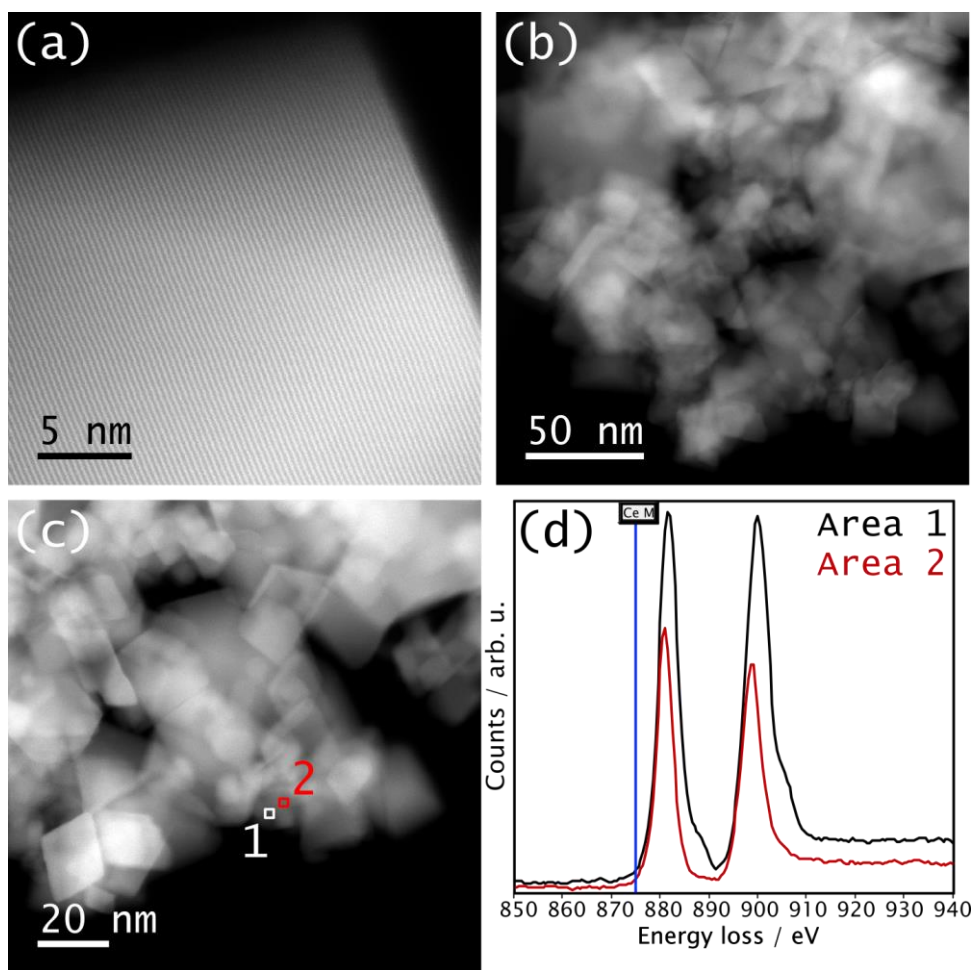


Figure A.7. (a, b) Selected HAADF-STEM images of Cu_1CeO_2 catalyst. These images also resemble those obtained for the support and $\text{Cu}_{0.5}\text{CeO}_2$. Electron energy loss (EEL) spectra (d) were taken at the positions highlighted in the STEM-ADF image (c). As observed for $\text{Cu}_{0.25}\text{CeO}_2$ and $\text{Cu}_{0.5}\text{CeO}_2$, Ce^{4+} (spectrum 1) and Ce^{3+} (spectrum 2) are visible.

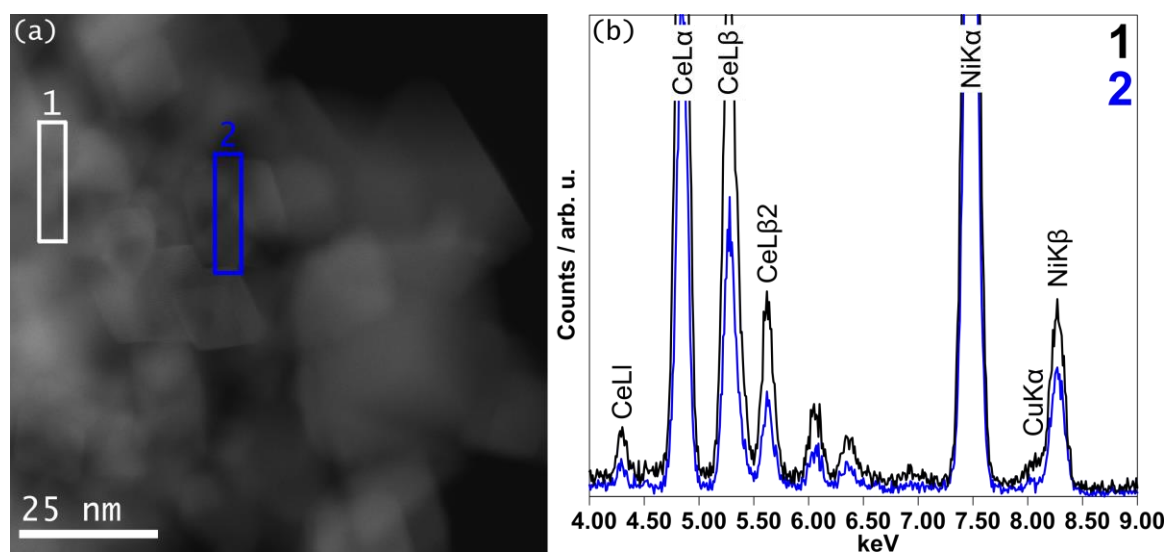


Figure A.8. Selected EDX spectra of the marked areas in the STEM-HAADF image of Cu_1CeO_2 (a) are shown in (b). Again, the minor peak of $\text{Cu K}\alpha$ can be seen in spectrum 1, which is proving the presence of Cu in this material. Spectrum 2 is taken at a position of smaller sample thickness (and thus lower amount of all constituents) so that no Cu could be observed.

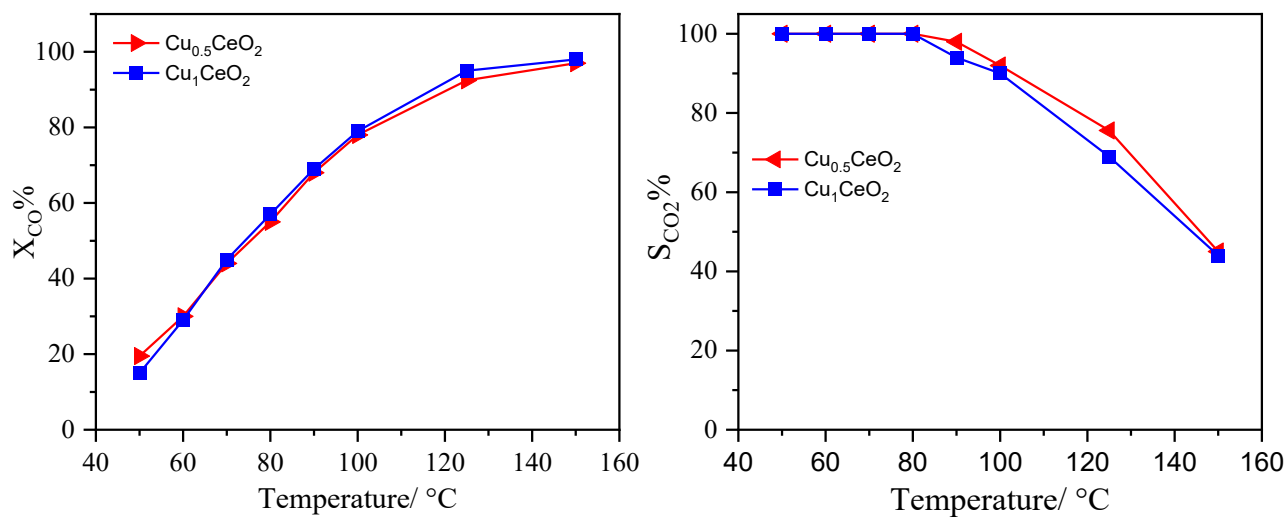


Figure A. 9. CO conversion (a) and CO₂-selectivity over new batches of Cu_{0.5}CeO₂ and Cu₁CeO₂

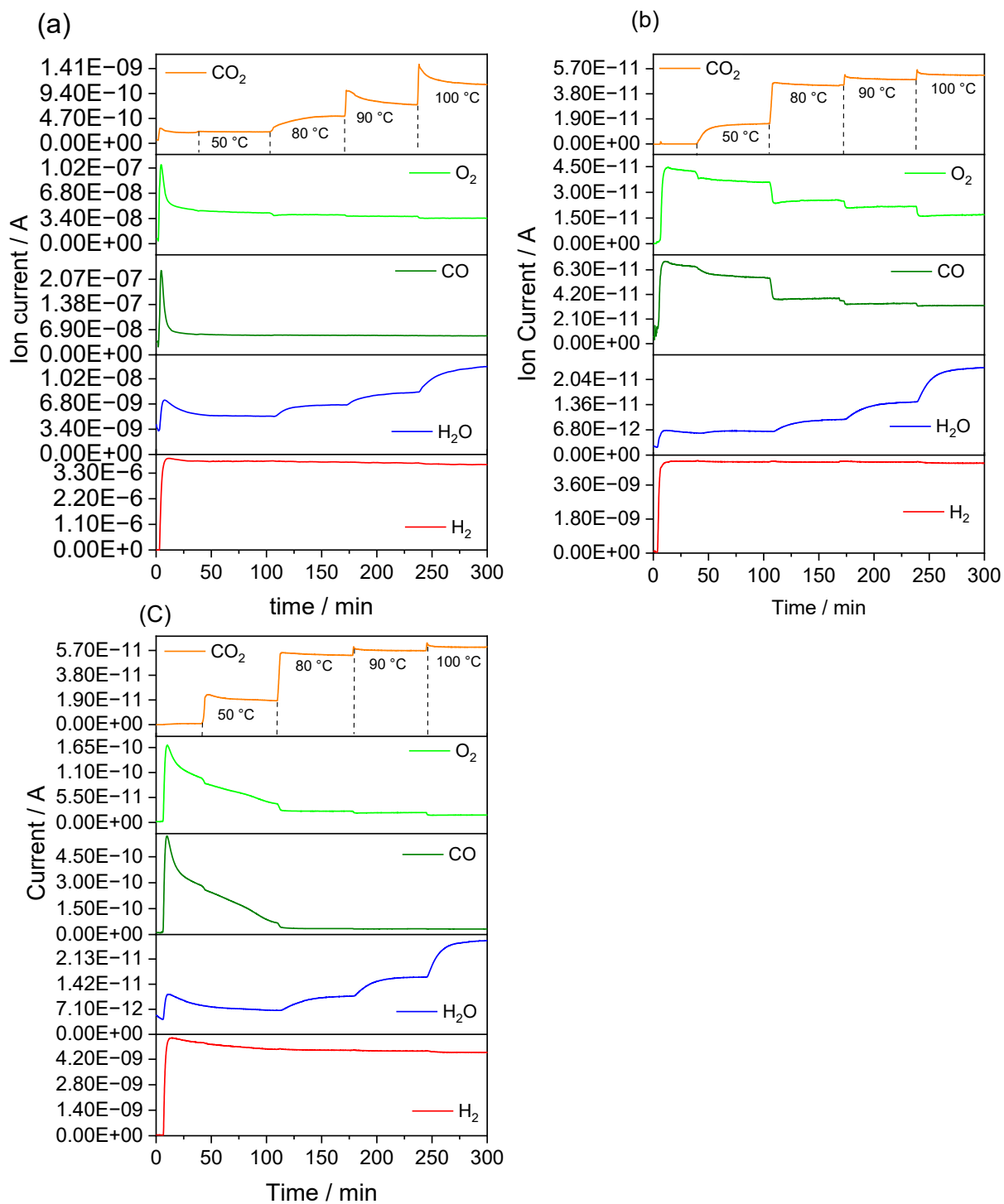


Figure A.10. CO converted to CO₂ detected by mass spectrometric analysis of the effluent gas stream over all samples (a) Support CeO₂, (b) Cu_{0.25}CeO₂, and (c) Cu₁CeO₂ in the range of temperatures (50-100 °C), carried out parallel to the operando DRIFT measurements.

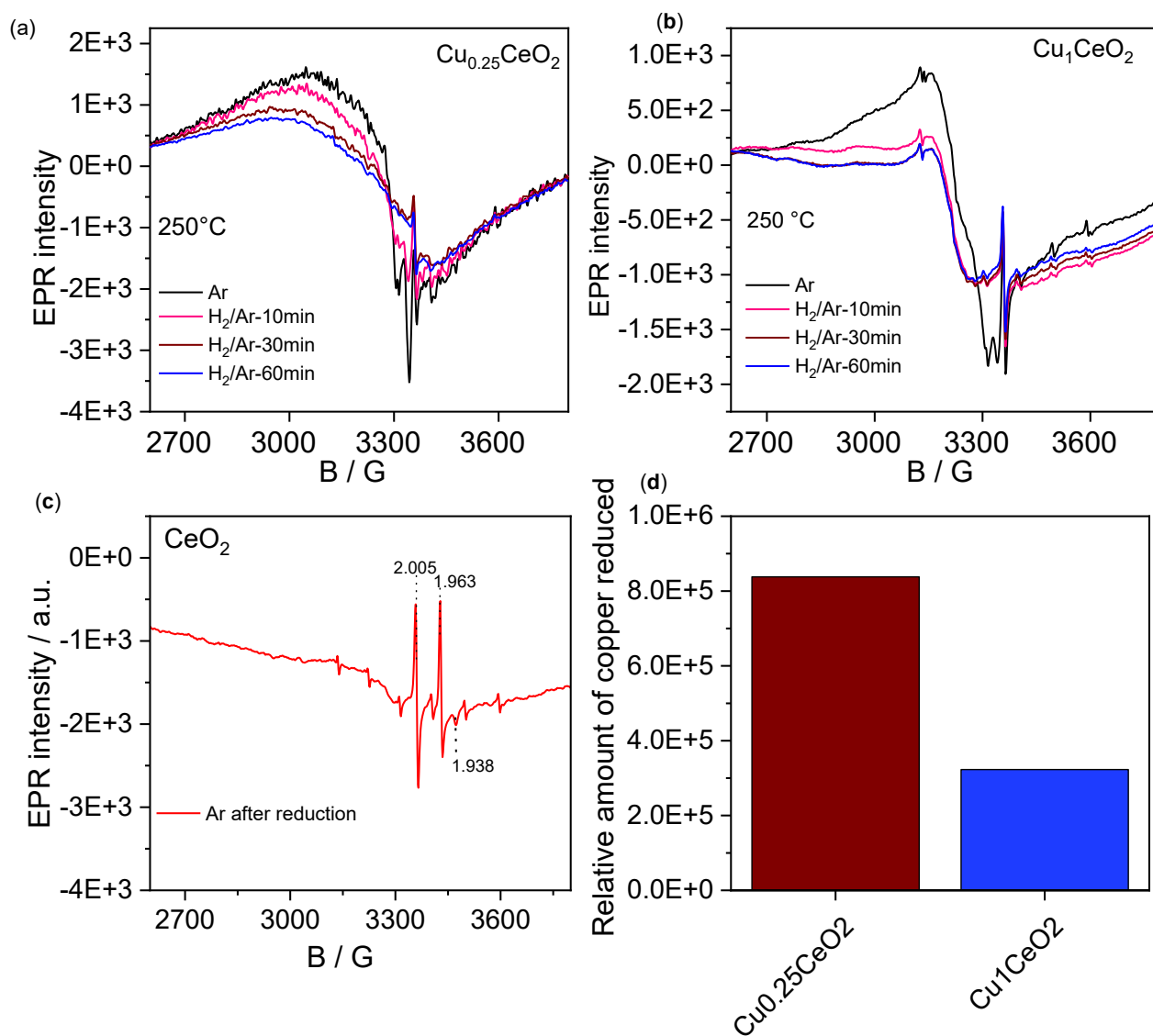


Figure A.11. Operando EPR spectra at $250\text{ }^\circ\text{C}$ of $\text{Cu}_{0.25}\text{CeO}_2$, Cu_1CeO_2 (a-c) after 1 h pretreatment with 10% H_2/Ar flow. (d) Relative amount of Cu reduced in the Cu-containing catalyst by CO/He.

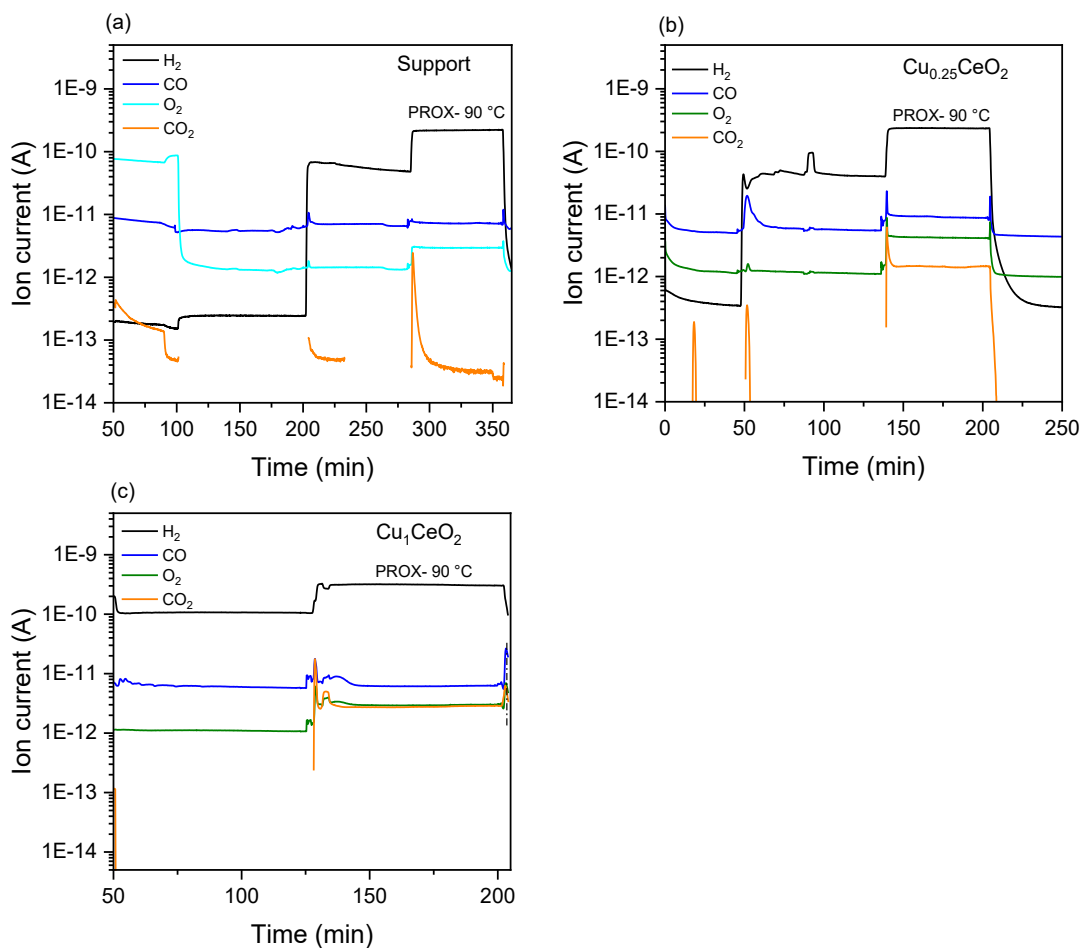


Figure A.12. CO₂ formation and CO oxidation detected by mass spectrometric analysis of the effluent gas stream over all samples (a) Support CeO₂, (b) Cu_{0.25}CeO₂, and (c) Cu₁CeO₂ at different 90 °C, carried out parallel to the operando EPR measurements.

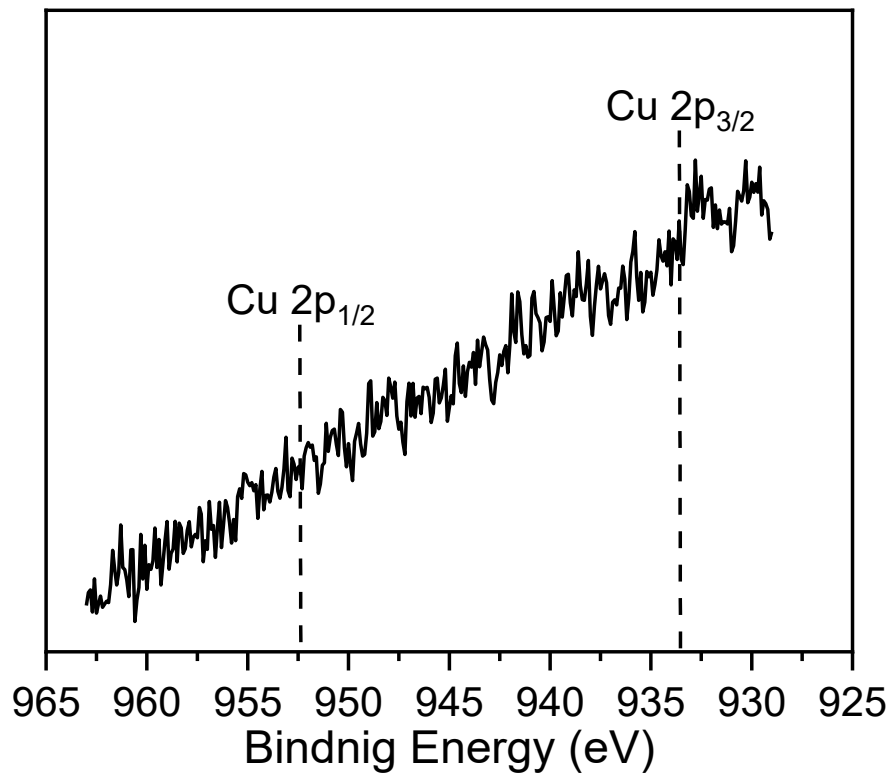


Figure A. 13. In-situ NAP-XP spectrum of the Cu₂p region of the Cu_{0.25}CeO₂ catalyst under He conditions at 90 °C temperature. Due to the presence of Ce at slightly lower binding energies and the low concentration of Cu, no signal corresponding to Cu can be found.

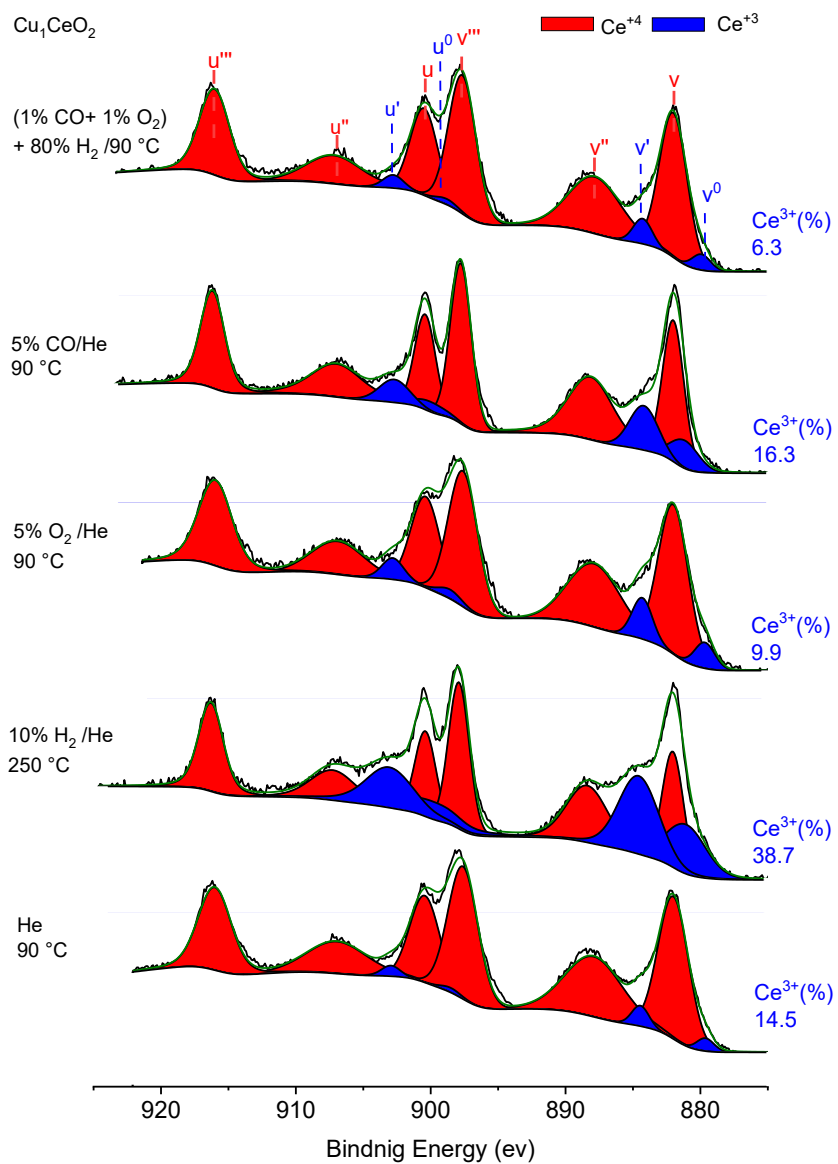


Figure A. 14. In-situ NAP-XPS spectra of the Ce3d region of the Cu_1CeO_2 catalyst measured under different conditions.

Curriculum Vitae

Full name : Hayder Jawad Abed

Date of birth: 19.08.1990

Place of birth: Al-Najaf/Iraq

Nationality: Iraq

+4915901484541

Hayder.Abed@catalysis.de

Alfatlawichem@gmail.com

Education

- 2020- today** **Ph.D. student**, at Leibniz Institute for Catalysis, Rostock University.
- 2013-2016** **Master student** in Organic Chemistry, Major: Industrial Chemistry, Mustansiriyah University
Note: GPA (83.97%, very good), Excellent, (92%) Marks of Thesis.
- 2008-2012** **Bachelor of Science** in Chemistry, Mustansiriyah University
Note: GPA (81.68%, Very good), rank 8.

Experience

- 2020- today** **Researcher at Leibniz Institute for Catalysis**
Research field is presently focused on two main subject areas: (i) synthesis and development of highly active and selective oxidation catalysis (CO-oxidation in the presence of hydrogen) and reduction catalysis (CO₂ reduction to Methane) (ii) using (in-situ and operando) spectroscopic methods to investigate the interactions of molecules on metal and metal oxide surfaces.
- 2017-2019** **Chemistry Lab Assistant and lecturer at** Faculty of Science, Wasit University.
- Lecturer of organic chemistry fundamentals.
 - Assisted students how to understand their experiments.
 - Lead lab assistant for the organic chemistry lab.
- 2016-2017** **Chemistry Lab Assistant at** Faculty of Education for pure Science, Karbala University.

Skills

- Technical**
- Two years of hands-on experience in working with Gas Chromatography.
 - Hands experience in building a new flow set-up for catalytic performance of gas phase reaction (CO₂-Methanation, CO-PROX and CO-oxidation) on solid catalyst.
 - Three years of practical experience working with in-situ DRIFT spectroscopy.
 - Practical experience of different kinds of spectroscopy (FTIR, EPR).
 - Data analysis, interpretation, and presentation (XRD, TPR, H₂-NAP-XPS, FTIR, EPR)
 - Various techniques of preparing in organic chemicals and heterogenous catalysts.

organic synthesis Procedures, basic and modern purification techniques of organic compounds such as thin layer Chromatography, Column Chromatography, Recrystallization and Vacuum Distillation.

Teaching Teacher of undergraduate courses: Fundamental of Organic Chemistry, Basic Principles of Spectroscopy: UV-visible, IR, ^1H -NMR, ^{13}C -NMR, The Systematic Identification of Organic Compounds.

Scientific publications

Part of this thesis has been published:

Journal articles fully related to this work

1. **Abed. H**, Mosrati, J. Abdel-Mageed. A. M, Cisneros. S, Vuong Thanh. H, Rockstroh. N, Bartling. S, Wohlrab. S, Brückner. A, Rabeah. J, Preferential CO Oxidation on a Highly Active Cu Single Atom Catalyst Supported by Ce–TiOx. *ChemCatChem* **2022**, 1-8.
2. **Abed. H**, Atia. H, Vuong Thanh. H, Bartling. S, Brückner. A, Rabeah. J. Preferential CO Oxidation on highly active copper supported ceria catalysts synthesized using a scalable and facile approach (submitted)

Additional articles

- 1 Cisneros. S, Santa. L, Martínez. Quintana. L, Rabee. A. I. M, Abed. H, Rockstroh. N, Bartling. S, Romero. M, Dongil. A. B, Brückner. A, Rabeah. J. The effect of O-vacancies on intermediates stability and electron delocalization over MgO modified Ru/ZrO₂: Spectroscopic insights during CO₂ methanation. *Chem. Eng. J* **2023**. 145646.
- 2 Cisneros, S.; Abdel-Mageed, A.; Mosrati, J.; Bartling, S.; Rockstroh, N.; Atia, **H. Abed**, H.; Rabeah, J.; Bruckner, A. Oxygen vacancies in Ru/TiO₂ - drivers of low-temperature CO₂ methanation assessed by multimodal operando spectroscopy. *iScience* **2022**, 25 (3).103886.

Contributions in conference

Poster presentations

Abed, H.; Mosrati, J.; Abdel-Mageed, A. M.; Cisneros, S.; Huyen Vuong, T.; Rockstroh, N.; Bartling, S.; Wohlrab, S.; Brückner, A.; Rabeah, J. Preferential CO Oxidation on a Highly Active Cu Single Atom Catalyst Supported by Ce–TiOx. 55th. Jahrestreffen Deutscher Katalytiker, Weimar (Germany), June 27-29, **2022**.